Quantifying stresses and strains from the Jura Arc, and their usefulness in choosing a deformation model for the region

David Andrew HINDLE

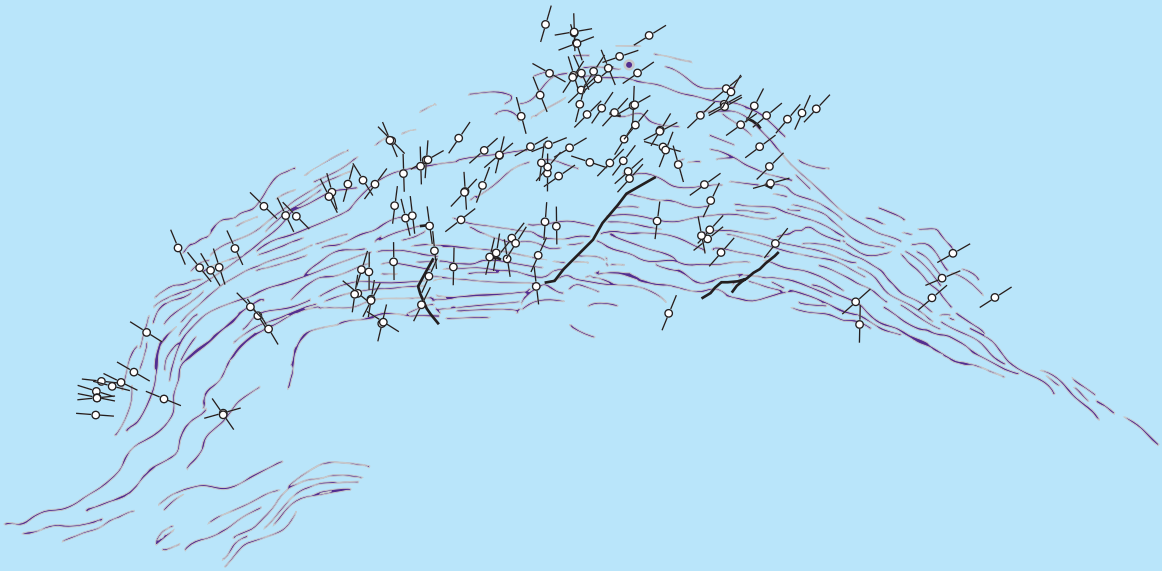

Thèse de Doctorat ès Sciences
présentées a la Faculté des Sciences
(Institut de Géologie)
de l'Université de Neuchâtel

Membres du Jury de thèse:
Prof. M. BURKHARD (Université de Neuchâtel), Directeur
Dr.. A. BECKER (University of Zurich)
Prof. O.BESSON (Université de Neuchâtel)
Prof. J.-P. GRATIER (Université de Grenoble)
Dr. J. NEWMAN (University of Utrecht)

Neuchâtel, Novembre 1997

Quantifying stresses and strains from the Jura Arc, and their usefulness in choosing a deformation model for the region

David Hindle[1]

[1]Institut de géologie, Université de Neuchâtel, Neuchâtel, Suisse

Pre-amble

This document is a newly created (July 2006), version of my PhD thesis, submitted in December 1997. The decision to resurrect such an old document was brought about by two things. Firstly, the realisation that my confidence in the permanence of digitally stored data such as word processing documents and graphics files was misplaced. With time, and changing technology, files become redundant and no longer accessible. Consequently, if I had not acted soon, it seemed there would only be a few paper records of this thesis remaining. Secondly, I had noticed a few citations of this work in the published literature, prompting me to wonder how on earth anyone knew of its existence, let alone its content. An integrated, pdf version of the entire original document will now, hopefully, be available electronically at the library of the Faculté des Sciences, Université de Neuchâtel, in permanence. The work is substantively unmodified, as I feel it should remain as the document of record of what counted as my thesis at the time. There are therefore only formatting corrections, for the most part to make the figures suitable for integration with the text and to make them fit into the LaTeX processing system.

One change to the original document is significant. Section 4 has now been replaced by the subsequent article in the Journal of Structural Geology that grew out of it. There seemed little point preserving the old matter in this case. Two figures from chapter 3 also "disappeared" over the intervening years and are no longer represented. Apart from that, everything is as it was.

Should anyone find and use this document, I hope it is useful to you. I spent an incredibly enjoyable four years in Neuchâtel preparing it. The correct citation of the work is

Hindle D., **1997** *Quantifying stresses and strains from the Jura Arc, and their usefulness in choosing a deformation model for the region*, unpublished PhD thesis, Université de Neuchâtel

David Hindle
Langwedel, Germany
July 2006.

Contents

Chapter 1

Geology of the Swiss Molasse Basin and Jura Mountains, and the history of studies of arcuate mountain belts

1.1 Introduction

1.1.1 Aim and scope of the study

The Jura and Molasse Basin form a fold and thrust belt generally considered to be the expression of the most external, late Miocene alpine deformation. The form of the belt is arcuate with a curvature of approximately 90° along strike. The internal Jura lacks cylindrical structures along most of its length, folds terminating laterally against tear faults, or dying out laterally, with displacement taken up on other adjacent structures.

Questions relating to the development of the fold and thrust belt are still debated. In the following thesis we discuss the kinematic evolution of the arcuate form of the belt. Many models have been proposed to explain the plan view geometry of curved mountain belts (Carey, 1955; Ries and Shackleton, 1976; Graham, 1978; Marshak, 1988; Ferrill and Groshong, 1993). We attempt an evaluation of these models in the light of field data from the Jura region. There is no hard and fast rule available to determine how the arcuate geometry of a fold and thrust belt has developed. Broadly speaking, we deal with three linked quantities which are key to all the questions of development of fold-thrust belts: force; displacement; and strain. Whilst they may be examined in isolation from one another, they remain intimately linked (figure 1.1).

Some thought about the implications of the various possible evolutionary models on not only the arcuate belt itself but also the adjacent hinterland and foreland begins to help us discriminate between the more and less plausible alternatives.

The question of finite strain patterns from the arc itself and its hinterland and foreland takes on great importance. The proposed geometry of movement of material within the fold belt may or may not imply deformation of the indenting region - the foreland. We have new data on finite strains from across the Molasse Basin from the use of calcite twin strain analysis. The strain axis orientation pattern can be compared (along with finite strain indicators from within the Jura) to those predicted for models.

Displacement fields from both hinterland and mountain belt can guide us in interpreting which dynamic model to choose for the particular arc we are dealing with (figure 1.2). Aiming to reconstitute the displacement field of a part of the Jura, we have constructed cross sections across the region and integrated them into a surface restoration of a part of the Jura.

In evaluating the different models of arc formation, it is difficult to proceed intuitively, so we analyse finite strain and compare it to its predicted value according to the kinematic model we choose. Thus, in parallel, we have calculated the finite strain patterns associated with different displacement fields which correspond to the some of the models imagined responsible for arc formation. We use simple models of deformation in plan and these form a fundamental tool used for choosing between deformation geometries.

Finally, models of the dynamic system of a moving thrust belt (a critical wedge) give some predictions as to the maximum values attainable for a differential stress. Burial depths of strata, if known, can also be related to the known present day stress gradients found in sedimentary basins, to give another estimate of a possible differential stress existing in a basin earlier in its history. Hence, calcite twins are used as piezometers from the Plateau Molasse, in order to test the correlation between stress magnitudes determined by different techniques, to compare these results to other studies using similar techniques, and to open the discussion on the question of stress magnitudes in the shallow parts of the earth's crust.

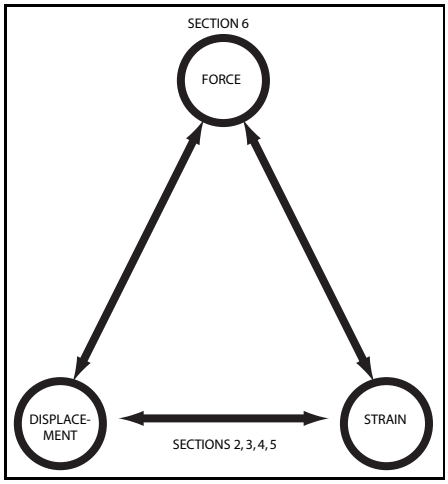

Figure 1.1: The basic relationship between force, displacement and strain, and the context of the different sections of this thesis.

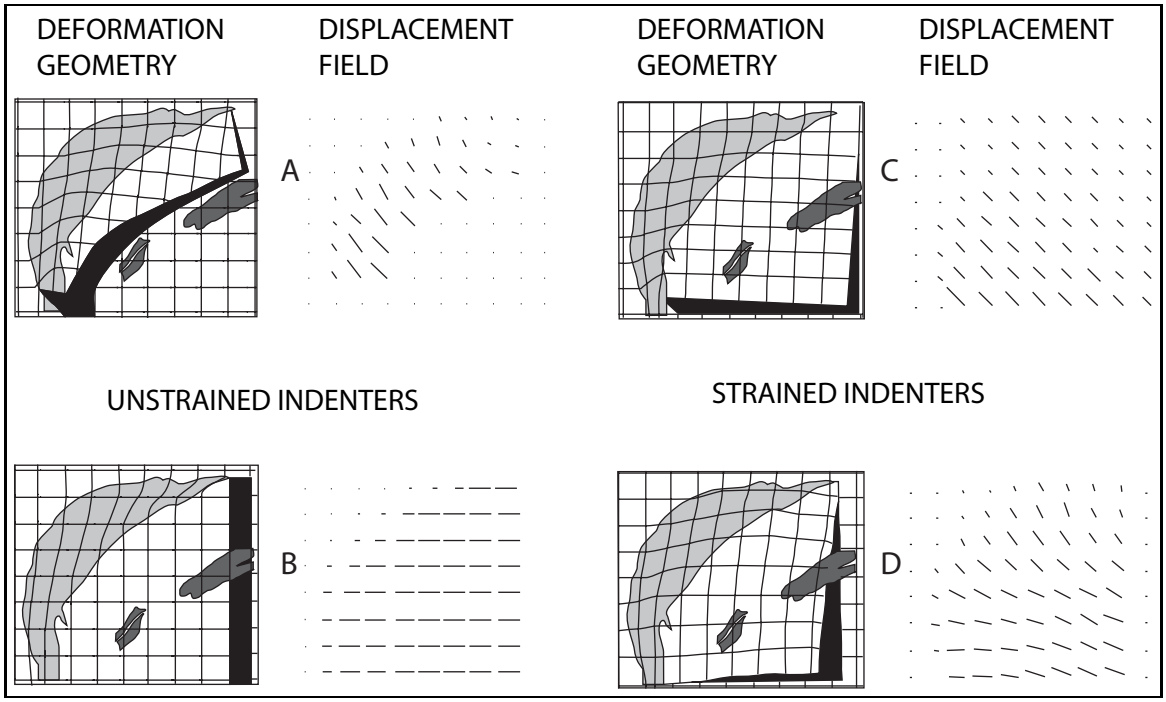

Figure 1.2: Possible Jura arc and hinterland deformation models (after Burkhard (1990)). a) Rotating indenter (Laubscher, 1965) - rigid body rotation of hinterland indents the Jura before it. b) Rigid indenter (Laubscher, 1972) - a rigid, non-rotational indenter pushes E-W into the Jura. c) Sheared indenter - displacements increase towards the southwest causing shearing across the indenter. d) Spreading indenter - indenter spreads and stretches (presumably a gravity spreading phenomena) and pushes into Jura. This model is often linked to achieving wedge critical taper.

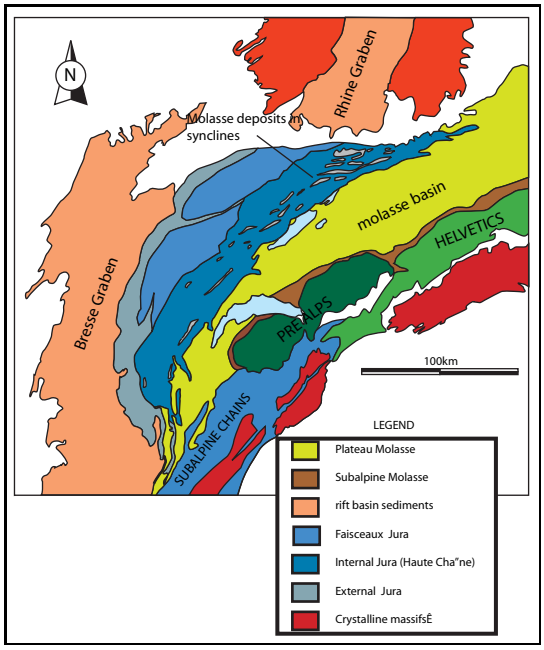

Figure 1.3: Disposition of the major structural divisions of the Jura mountains and the Molasse Basin, and their relationship to earlier western Alpine structural units.

These questions still remain open and our aim is in part to highlight the methods available to answer them. The evaluation of the methods is thus of considerable importance and forms an important part of what follows.

1.1.2 The geology of the Jura and Molasse Basin, a short review

Structure and geography

The Jura mountains form an arcuate mountain belt 400km long along its outer bend and 340km long along its inner bend. At its widest, the Jura measures 65km between Yverdon (Switzerland) and Besançon (France).

The fold belt terminates in the east when the last fold dies out in the Molasse basin. Along its western and northern border, it overthrusts the Rhine-Bresse graben. The northwestern border overthrusts tabular Jura. In the south, there is an important transfer zone which shifts folding and thrusting into the French Subalpine Chains, a contemporary fold belt (Philippe, 1995) (figure 1.3).

Two distinct regions are identified within the Jura arc, namely the external Jura and the internal Jura. The internal Jura is often referred to as the 'Haute Chaîne' and consists of folds and thrusts representing the northern limit to the Molasse basin. The region is cut by large tear faults forming lateral terminations for the thrusts. The fold thrust belt is arcuate, the fold axes trending north-south in the south of the belt, but swinging through 90° to trend east-west by its eastern termination. The external Jura is composed of flat 'Plateaux' separated by 'Faisceaux' - zones of intense deformation due to small imbricate thrusts and tear faults.

The Tertiary sediments of the Molasse Basin rest against the southwestern limit of the Jura. They remain relatively undeformed (but certainly translated a considerable distance) in the region known as the Swiss Plateau. There is only gentle folding of the sediments in the plateau Molasse.

This contrasts strongly with the folded and thrust Jura to the northwest and the Subalpine Molasse to the southeast, folded and thrust into quite spectacular structures. The Subalpine Molasse's northern limit, joining it to the Plateau is a triangle zone along a considerable distance according to seismic profiles. The southern limit represents the Oligocene alpine front. Additionally, the Jura Molasse - the Tertiary packets of sediment remaining in the Jura synclines and bearing witness to the original extent of the alpine foredeep, can also be identified. These sediments are implicated in the folding of the Jura.

The ensemble of the Swiss Molasse can be regarded as a hinterland to the Jura mountains. Strong layers of Mesozoic carbonates which are the components of the fault related folds of the Jura are both laterally continuous and relatively undeformed beneath the Plateau Molasse.

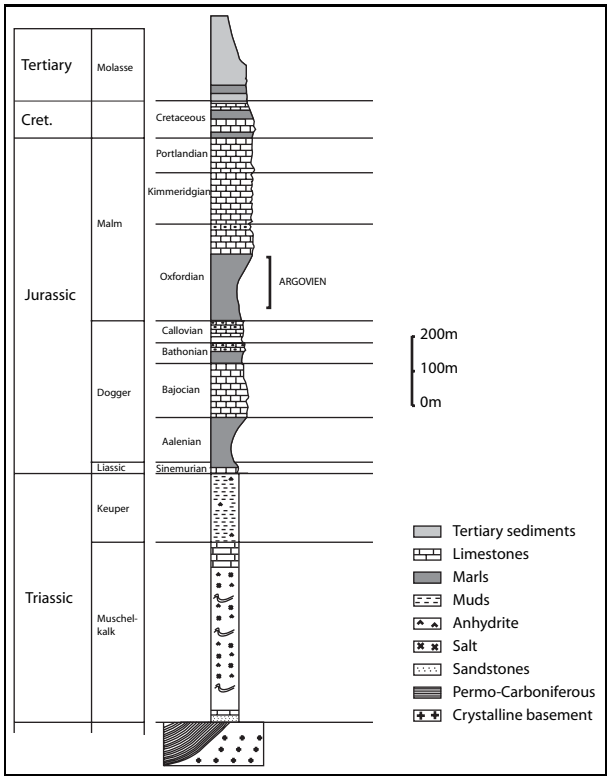

Figure 1.4: Stratigraphic column showing the major units encounterd in the Jura fold and thrust belt. Of particular interest are 1) The Triassic evaporite series which form a basal décollement for the fold belt 2) The Argovien, the top surface of which is used as a marker for retro-deformation later in the thesis.

Moving eastwards, the structural style of the Molasse Basin changes markedly. East of the eastern Jura termination, the evaporite series which forms a dcollement onlaps the basement and is not present beneath the northern sector of the basin. Without a dcollement layer, the basin's Mesozoic series has not slid above the basement.

Stratigraphy

The western Swiss Molasse Basin and the Jura Mountains are composed of Mesozoic and Cenozoic packets of sediment, several kilometres thick and with a highly variable geometry and which are now allochthonous on a basement of Permo-Carboniferous and older rocks. Significant amounts of the most recent deposits are removed by erosion. This is the case in the Jura mountains, where Tertiary sediments remain only in synclines.

We are particularly concerned with the sediments ranging from Triassic evaporites which form a basal décollement beneath both the Molasse and the Jura mountains to the latest Miocene deposits of the Molasse series itself. These are summarised in the stratigraphic column (figure 1.4). This Mesozoic and Cenozoic series developed on the stretching and subsiding margin of the Eurasian plate in a complex series of basins, before its involvement in the African-Eurasian collision. The Tertiary sediments by contrast were deposited in the collisional setting of the alpine foreland basin (the Molasse).

Triassic deposits of the Jura/Molasse region are considered to result from a general regression off continental margins forming large areas with restricted marine waters, intermittently replenished. This led to the accumulation of the thick (100's of metres) accumulations of evaporites ranging from halite to gypsum. These deposits have a complex palaeogeography (Ziegler, 1982).

Variably thick (up to 800m) sequences of Triassic evaporites are present at the base of the Mesozoic series across the parts of the Molasse Basin and the Jura examined in this thesis.

The Jurassic period (ca. 200-140Ma) is characterised by a continuous marine sedimentation of thick carbonate sequences with occasional detrital beds coming from erosion of stable massifs which remained above the level of an epicontinental sea.

The period begins with Liassic deposits which are practically never visible in the region of the Jura, but which are usually present and have a thickness of up to 100m. Then follows the thick Dogger succession from 'Opalinus Ton' to 'Dalle Nacrée', variously marls and carbonates. As of the Oxfordian (ca. 160Ma) we enter the Malm, whose base is composed of a thick sequence of marls, the so called Argovien. Following this unit are the Sequanian, Kimmeridgian, and Portlandian. The hydrodynamics of the various basins show a gradual evolution from calmer, deeper waters to shallower, eventually emersive situations under stronger influence from currents and tides.

Marine conditions prevailed once again during formation of Lower Cretaceous carbonates across the Jura with large lateral thickness variations (increasing in thickness towards the southwest).

Truly alpine influences on sedimentation are apparent in the character of the thick Tertiary deposits forming the Molasse basin infill in the alpine foreland. This fill is laterally continuous as an apron around the outer part of the bend of the alpine chain. The Tertiary series extended across the present day Jura to varying degrees, with a northwestwards advancing onlap as time went on (Homewood, 1986; Homewood et al., 1986), geodynamically controlled by an advancing alpine front causing a forebulge. Amongst this Tertiary series, the OMM (Obere Meeres Molasse) forms a marine series of coarse sandstones and conglomerates, containing shoals of carbonate debris, composed of macroscopic bioclasts. This rock is has a well developed sparitic cement. This horizon has been the focus of a calcite twinning study in the Molasse Basin itself. The Tertiary sediments of the basin range between earliest Oligocene and late Miocene age. They are split into two marine and two freshwater/fluviatile series, reflecting transgressions and regressions across the alpine foredeep.

1.1.3 Tectonic Evolution and Dynamics of the external, northwestern Alps

The Alps and the Jura

The tectonic history of the northwestern Alps is one of considerable complexity. The Alps have formed over a long collisional tectonic period (Late Cretaceous to ? present), timings of events varying even in the small domain of the western alpine arc (Platt et al., 1989b). The pre-collision history of the alpine domain is also very influential on the structural evolution of the region (Tricart, 1984; Lemoine et al., 1986).

The Jura arc, forming the culmination of the northwestern Alps, is bordered by different Tertiary Basins, these being the Rhine-Bresse graben system to the north and the west and the Molasse Basin (and behind it, the western Alps) to the southeast. There is a contrast in the structural style of the Tertiary basins. The Rhine graben corresponds to an Oligocene phase of rifting which affected the European platform, influencing some of the structures in the Jura, particularly the external regions. The Molasse basin is the foreland to the Alps, and the hinterland to the Jura. Its importance is manifest in the development of since it forms a key part of the wedge of material pushed in front of the Alps which culminates in the folds of the Jura.

Recent tectonic history, development and dynamics of the Jura

Including the Tertiary events described, up to four different tectonic events - see for instance Homberg et al. (1994); Bergerat (1987) - have affected the strata of the Jura mountains. The two latest of these have the most bearing on the problems discussed here.

Oligocene extension related to the Rhine Graben opening has been documented by many authors (Lacombe et al., 1990), and is possibly responsible for basement structures beneath the Jura. The extension gives rise to fractures oriented northeast-southwest and north-south. These may later have localised and initiated Jura strike-slip faults during Mio-Pliocene compression. Multiple fracture orientations are a feature of the Jura mountains, and whilst polyphase tectonics is a possible cause, alternative explanations exist (Reches, 1978).

A well documented northwest or northnorthwest compression and transport of the Mesozoic series above a well-defined Triassic décollement (Buxtorf, 1916; Laubscher, 1961; Tschanz and Sommaruga, 1993), the onset of this movement usually being considered as late Miocene (Burkhard, 1990) is considered to be the push which created a folded Jura. It marks the forward migration of the outer most alpine thrust, the front effectively moving from the Oligocene limit of the southern Subalpine Molasse bounding thrust. The Jura fold and thrust belt is also an example of an critical wedge. It has a shallow dipping (2-3° eastwards) basement, and a weak décollement horizon within Triassic evaporites. The translation of material above a weak décollement horizon has for many authors, affected the Molasse Basin in Switzerland as well as the material in the Jura mountains, the Molasse Basin thereby forming a hinterland to the Jura arc. The Molasse basin's Tertiary sediments reach 4km thickness in places. Their feather edge is above the Mesozoic sediments of the present day Jura mountains. It contributes

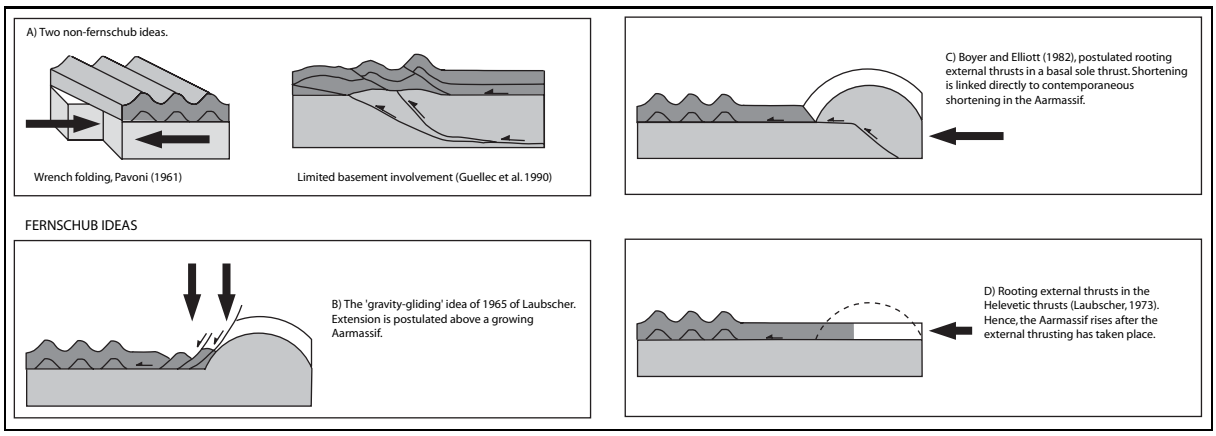

Figure 1.5: Possibilities for pushing the Jura or otherwise adapted from Burkhard (1990)

to the total thickness of the sedimentary wedge of the Jura and Molasse which is up to 7km in the south but diminishes to just a few hundreds of metres in the north.

The importance of the Molasse basin as a hinterland to the Jura arc is undeniable. It plays a key dynamic role in any Coulomb wedge model proposed for the Jura as a whole (Laubscher, 1980; Mugnier et al., 1990).

This interpretation of the Jura as a thin-skinned foreland fold and thrust belt above a regional detachment horizon has been challenged with alternative explanations both in the past (Aubert, 1945, 1959; Pavoni, 1961) and more recently (Ziegler, 1982; Gorin et al., 1993). However, seismic data interpretation (Sommaruga, 1995) seems to support the existence of a regional décollement, of considerable thickness, and of no significant basement involvement in thrusting.

Fernschub hypothesis and other questions of Jura dynamics

In the previous section, the idea of a northwestern push of the Mesozoic cover sequence originating in the Alps has been outlined. The Mesozoic cover sequence across the Molasse Basin and the Jura mountains is transferred and becomes allochthonous on its basement due to the easy gliding possible over the extensive deposits of Triassic evaporites at the base of the Mesozoic in this part of the western Alps. The presence of the décollement horizon is obviously key to the movement of the Mesozoic cover above its basement. This idea has been expressed in relation to the formation of the Jura at least since the early part of this century.

Buxtorf (1916) and later, Laubscher (1961) proposed a 'fernschub' hypothesis (meaning distant push), representing the push coming from the Alps. Shortening in the detached Mesozoic is considerable (25-30km in some areas) and must be compensated at deeper levels in the basement. There is no shortage of possibilities for models of shortening in the basement. Nevertheless, despite the now considerable evidence in favour of this interpretation of the structure and development of the Jura mountains, there have been many proponents of alternative ideas involving basement material in the Jura thrusts and requiring less or no compensation of shortening in the basement in the Alps (Aubert, 1945, 1959; Pavoni, 1961; Ziegler, 1982; Guellec et al., 1990). Figure 1.5 shows some of the different possibilities, involving basement or otherwise.

Figure 1.5a shows the contrasting ideas of Pavoni (1961) and Guellec et al. (1990). Pavoni (1961) proposed an *in situ* formation of the Jura by wrench folding above basement strike slip faults. Gehring et al. (1991) presented palaeomagnetic evidence which appeared to contradict this idea. They found no evidence for any anti-clockwise rotations from the Jura which would be required in Pavoni's model. Guellec et al. (1990) proposed a mixture of basement involvement to explain some of the uplift of the Haute Chaîne of the Jura. Beneath the Haute Chaîne, in a cross section passing through the south western part of the Jura, interpretation of the ECORS seismic data apparently shows some basement culminations which could be explained by crustal duplexes which impinge on the Mesozoic sequence of the Jura above and contribute to the relief of this area. This idea is effectively a mixture of a detached, allochthonous cover and a basement involvement in shortening. Mugnier et al. (1990) also proposed a small basement involvement in Jura dynamics, on this occasion only affecting the external Jura. Other ideas involving an autochthonous cover have been proposed by Aubert (basement contraction (Aubert, 1945, 1959)) and Ziegler (1982) (basement sole thrust under the Jura).

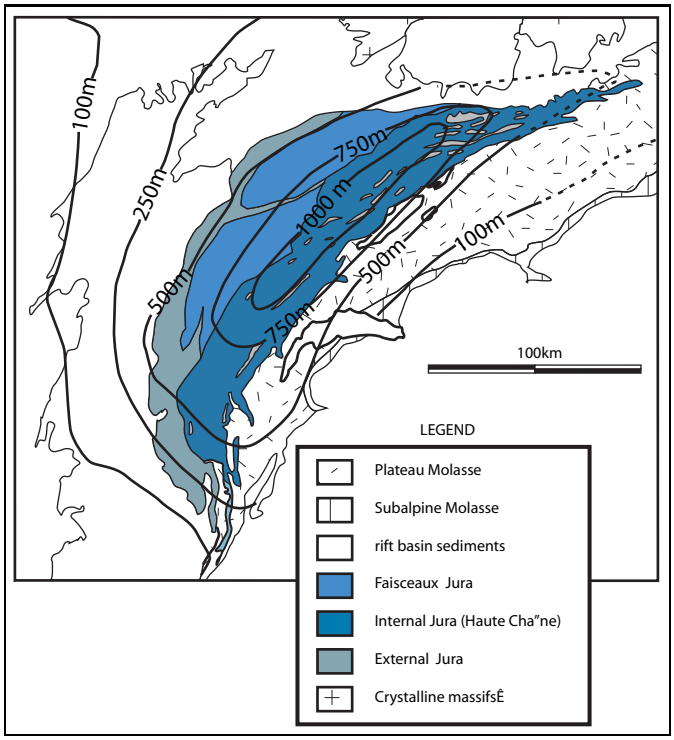

Figure 1.6: Geometry (isopachs) of the Triassic evaporites in the Jura fold and thrust belt, from Sommaruga (1996). The maximum thicknesses of evaporites correlate well with the geography of the Internal jura, whilst the 250m isopach seems to limit the terminations of the Jura. Undoubtedly, the ductile evaporite layers are a key factor in the development of this fold and thrust belt.

Fernschub-type shortening models are shown in figure 1.5b-d. Gravity gliding above a rising or pre-existing Aarmassif was proposed by Laubscher (1965). Many author's have favoured a basal sole thrust beneath the Aarmassif to root external thrusts (e.g. Boyer and Elliott (1982) - figure 1.5c). Figure 1.5d shows Laubscher's idea of rooting external thrusts in the Helvetic thrusts. Arguments about the timing of uplift in the Aarmassif tend to rule against this possibility. A more complete review of these alternatives is given by Sommaruga (1996), including additional possibilities for basement involvement in thrusts in the Jura.

Triassic Pinchout

The fernschub idea has a reliance on the mechanical properties of the evaporite layers in the Triassic beneath the Jura and elsewhere. The geography of the evaporite layers has now been mapped in detail, using seismic data (Sommaruga, 1996). Allen et al. (1986) pointed out the importance of the shape of the Triassic evaporite layers and their close correlation with the form of the Jura mountains. Once the pinch out of the evaporites is reached, detachment of the Jura from the material below is no longer possible, and the consequence is a rapid drop in the amount of displacement of points along the outer edge of the Jura (French side) to zero. To some degree, the Jura mountains change in character along this boundary, from the thrust Haute Chaîne to the external Jura which has occasional, localised and intense zones of deformation - faisceaux - within it, but which does not show extensive fault-related folding (figure 1.6).

1.2 Arcuate mountain belts - a review

Since at least the time of Carey, (Carey, 1955) the bending in plan view of many thrust belts has been recognised and treated as a major question in geodynamics. Carey himself rightly pointed out that the dimensions of most arcs were of a similar order and resembled 'strip lamina'. The question of how to bend strip lamina into the curved from of contemporary thrust belts was then asked. The original conclusion was by means of bending or impressing a straight fold belt around some basement obstacle. This apparently obvious and straightforward

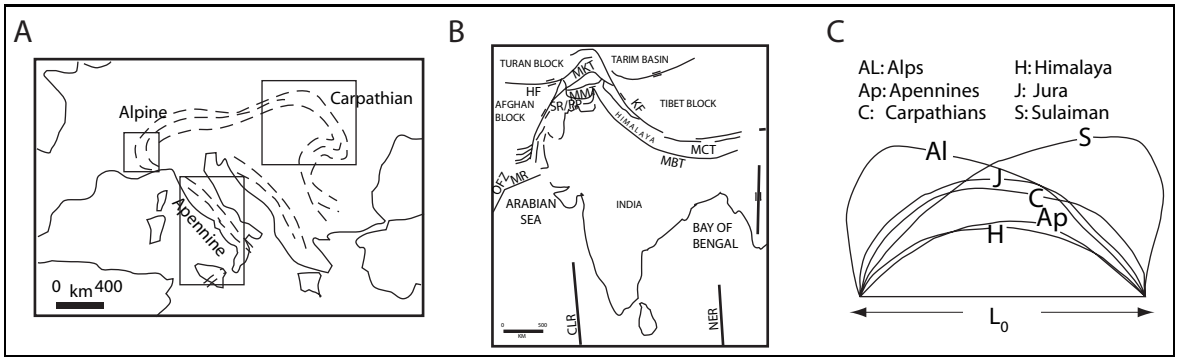

Figure 1.7: A view of some of the major arcuate mountain belts around the world. a) SUBALPINE CHAINS, Graham (1978) - wrench faulting in the basement Siddans (1979)- gravity spreading behind the arc and polyphase deformation: APPENINES - SICILIAN CANTABRIAN ARC, Eldredge et al. (1985) - compared palaeomagnetic declination differences to fold trend differences to decide on arc formation models: CARPATHIANS, considered to be a result of polyphase accretion of micro-plates during alpine orogenesis. b) HIMALAYAN MOUNTAINS, contains several arcuate belts (Makran, Sulaiman, Salt Ranges, Kashmir). Salt Ranges (SRT/SR/PB) in particular share mechanical features with the Jura. Over all the belt, a differential evolution is proposed with respect to the stage of subduction/collision reached in each zone Davis and Lillie (1993). c) ARC MARKER LINES, from Marshak (1988) - these are the plan views of the hinterland/deformed zone boundaries for various arcs around the world. Normalized to L_o

conclusion led on to attempts to unravel many curved fold belts and to try and reconstitute the palaeogeography of large regions of the earth. The solutions (for instance the alpine system solution of Carey) are tempting by their simplicity. However, since then, several other candidate mechanisms for arc curvature have been proposed (Freund, 1970; Ries and Shackleton, 1976; Graham, 1978; Siddans, 1979; Burchfiel, 1980; Eldredge et al., 1985; Merle, 1989; Marshak, 1988; Ferrill and Groshong, 1993). These alternatives are now reviewed. We also attend to the question of the Jura and review the possible explanations given for their curvature.

1.2.1 The Jura arc geometry

The Jura mountains have an arcuate form. They undergo a curvature of approximately 90° along strike. The Internal Jura lacks cylindrical structures along most of its length, folds terminating laterally against tear faults, or dying out laterally, with displacement taken up on other adjacent structures. Displacement ends at the eastern end of the Jura where the last fold dies out in the Molasse. Logically, displacement should be transferred elsewhere, but clear evidence for a transfer zone across the Molasse basin back into the Alps is lacking. In the southwest, the transfer of displacement takes place along a well described transfer zone linking the Jura to the French Subalpine Chains (Philippe, 1995)

1.2.2 Arcs or oroclines of Earth

The Jura mountains are far from unique in having an arcuate form. Arcs or oroclines are recognised along many collisional plate boundaries (Freund, 1970; Graham, 1978; Siddans, 1979; Burchfiel, 1980; Eldredge et al., 1985; Marshak, 1988; Davis and Lillie, 1993; Ferrill and Groshong, 1993). Over the years, different authors have at the same time tried to analyse the possible mechanisms of formation and to find ways of differentiating between particular mechanisms of creating such features (see for instance Carey (1955); Ries and Shackleton (1976); Eldredge et al. (1985); Marshak (1988); Ferrill and Groshong (1993). This whole thesis is no more than another attempt to do so. Figure 1.7 shows a general map of the alpine system of Europe and the different bends which have been studied separately as arcs. It also shows the Himalayan collision zone and the profile of the boundaries between deformed and undeformed zones from several arcuate mountain chains around the world.

1.2.3 Classifications of bends or oroclines or arcs

Carey (1955) defined oroclines as orogenic systems which were originally straighter than they are today. An originally straight fold belt is assumed to have undergone some later bending in plan view. Ries and Shackleton (1976) defined the terms primary and secondary arcs. Primary arcs are those curved belts whose curvature

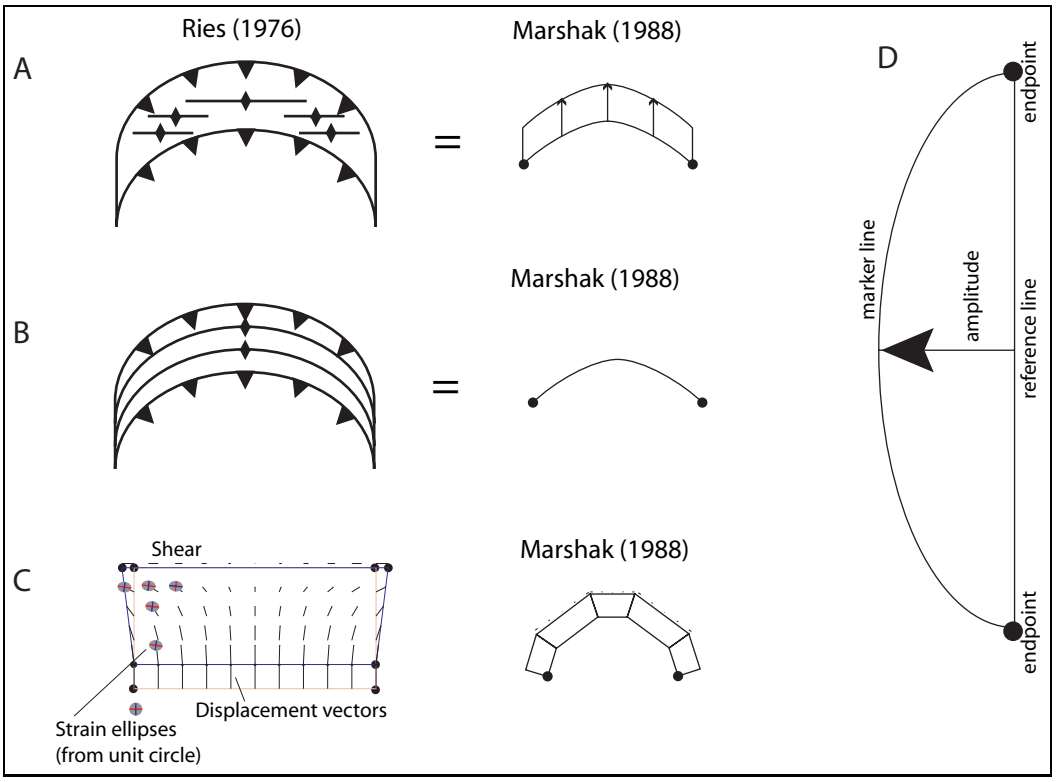

Figure 1.8: Illustration of the problems associated with creating a true primary or non-rotational arc. The ideas are based on models from Ries and Shackleton (1976) and from Marshak (1988). a) Primary arc, proposed by Ries and Shackleton (1976) is impossible. The straight fold axes implied by their model do not exist (see section 4). b) Case with 'vertical movement only'. There is no horizontal displacement. This is hard to imagine in nature. Such vertical movements around a bend in a continuum would provoke horizontal movements too. c) Although this model produces no rotation of a line parallel to a horizontal boundary, it has a shear effect across the rectangle which is analagous to the situation shown by Marshak (1988) and whose consequence is rotation. d) Definitions of arc geometry. 1) endpoint: point of inflexion in curve. 2) reference line: straight line linking endpoints. 3) marker line: line following structural grain of orogen. 4) amplitude: distance from reference line to crest of marker line.

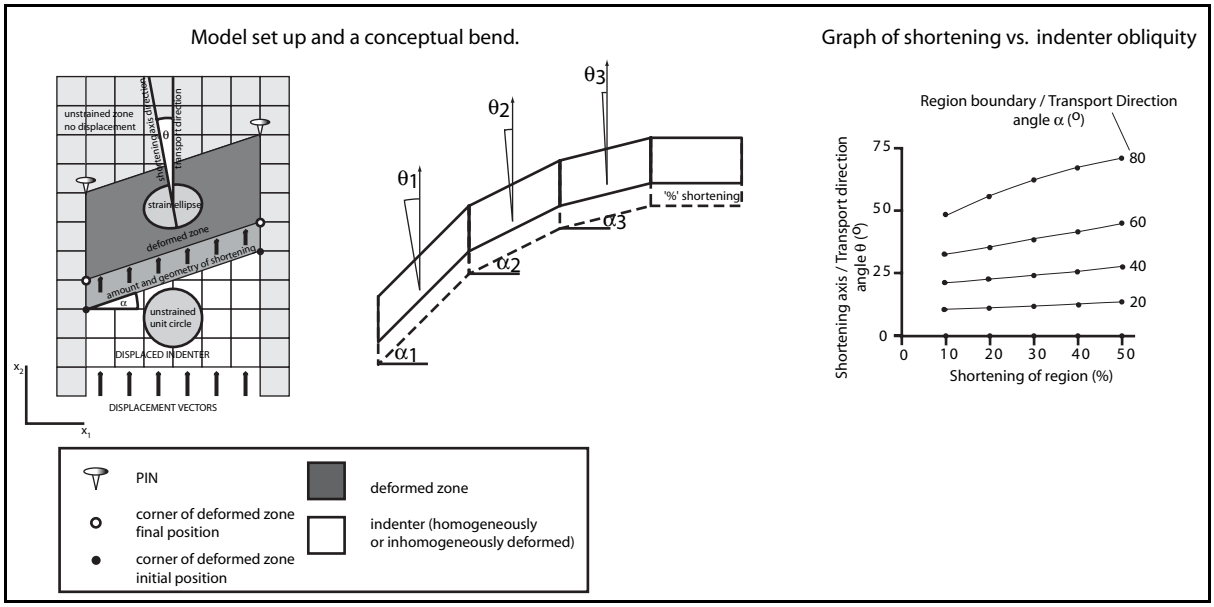

Figure 1.9: Model conditions for transport parallel simple shear with a rigid indenter, and the consequence of obliquity between a deformation zone and the shortening direction. Although shortening of any line parallel to transport is constant, there is still a shear across the region. The graph shows the consequent relationship between shortening amounts and deviation of shortening axes from transport direction.

is a primary feature. Secondary arcs form by some mechanism of bending of an originally straighter belt (in other words an orocline). Marshak (1988) stressed the timing of curvature formation in arcuate belts. Carey's definition of an orocline does not include a case where curvature forms at the same time as orogenesis, a possible consequence of transport parallel simple shear. Hence, Carey's original definition of oroclines has tended to be loosened. Marshak (1988) proposed a separation of arcs into those where rotation has occurred and those where rotation has not done so. These he called oroclines and non-rotational arcs. He based his conclusions on various reference lines and points defined in figure 1.8

Primary arcs or non-rotational arcs

Primary arcs or non-rotational arcs were originally defined by Ries and Shackleton (1976) and later by Marshak (1988) as mountain belts whose curvature is original and unchanged. Their models either envisage an annular segment of crust which is compressed and which shows an original and unchanging curvature of fold axes, or even a curved region but with parallel, constant fold axes orientations (figure 2a of Ries and Shackleton (1976)), showing the case of a primary arc (see figure 1.8). None of the primary arc models as defined by the authors allow for any shearing deformation in the zone. Since the boundaries of the region are inclined to transport direction, it is easy to prove that any movement of one boundary relative to the other will generate a shear and an inhomogeneous strain distribution across the zone. Figure 1.9 shows the boundary conditions associated with some of the models of primary arcs or non-rotational arcs. Displacement is everywhere constant and parallel. The variable is the inclination (α) of a region to transport. The result is a variable angle (θ) between the transport direction and the maximum shortening direction in a zone. A graph of this is shown with various values of inclination (α) and shortening (%). Conceptually, an arc could be made up of several segments of bend at different angles (θ) to transport direction.

Marshak shows three cases of non-rotational arcs (effectively primary arcs). These are summarised in figure 1.8. The same problems described above are associated with all these conceptual models.

Secondary arcs or oroclines

In the literature, authors attribute different meanings to the term secondary arc. For instance, Ries and Shackleton (1976) include shear mechanisms, and bending and buckling mechanisms amongst this group of bends. The original definition of an orocline by Carey (1955) only englobes bending and buckling models. The enlarged definition of

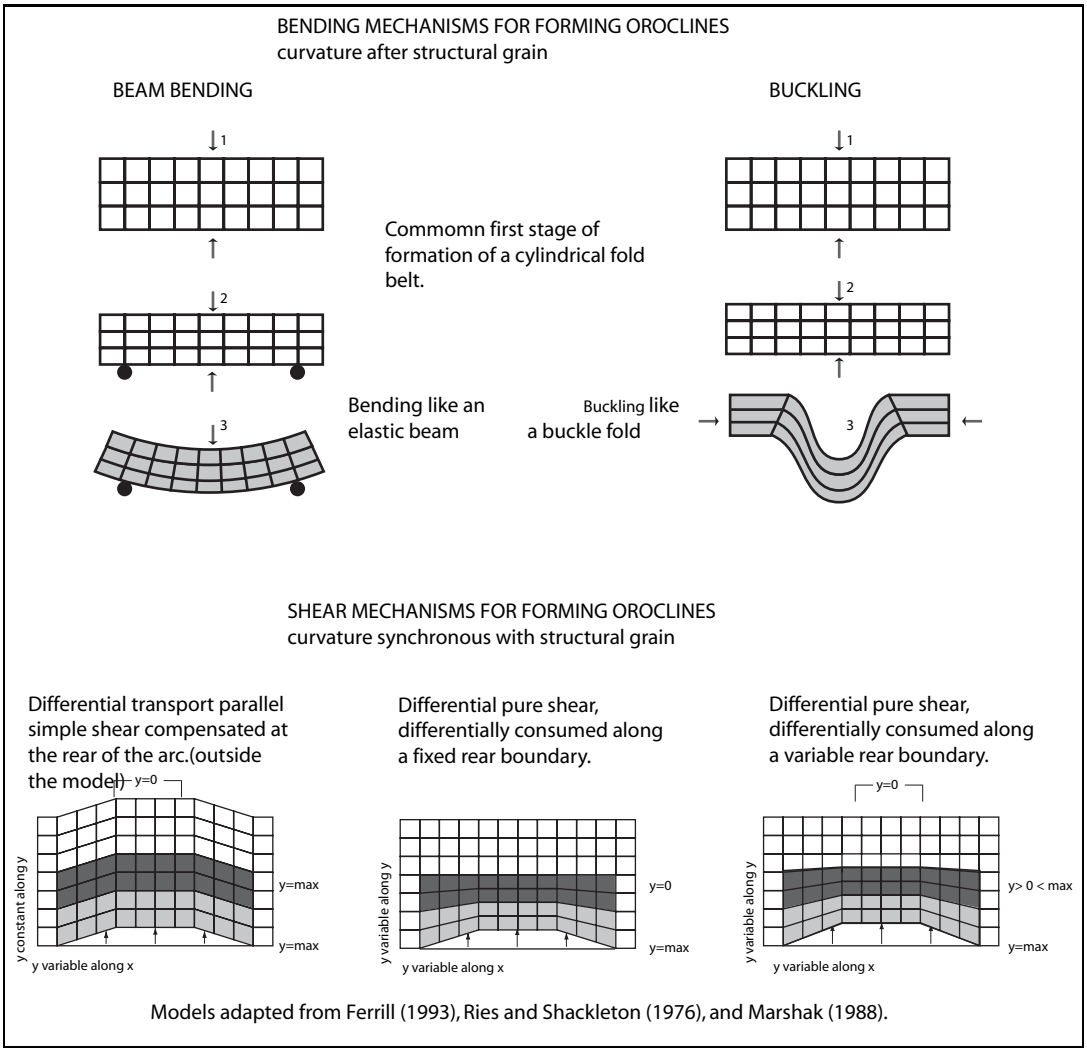

Figure 1.10: Oroclines or secondary arcs could form by any of the methods outlined below. These divide into two main groups, bending and shearing, and each of these is a set of possible geometries. The essential difference is the synchroneity of deformation and curvature formation in the shear models whilst bending involves a two phase evolution.

Marshak (1988), and also, because of the inclusion of a shear mechanism, that of Ries and Shackleton (1976), include arcs formed by a single event of progressive deformation.

This latter type of mechanism has since been defined as 'transport parallel simple shear' (Ferrill and Groshong, 1993). A series of different cases of this have been envisaged, but essentially, the model involves displacement of a lower boundary (reference line) by a series of parallel displacement vectors with changing magnitude along strike. Any such combination will at least cause simple shear in a zone affected by it. Compression may also occur if the zones width (distance between two reference lines) diminishes. The deformation will be homogeneous or inhomogeneous according to whether or not two reference lines remain parallel after displacement has occurred. These cases are shown in figure 1.10.

New classification for arcs

Previous definitions used for arcs overlap, are contradictory or worse, incorrect. A simplification of the classifications used can be proposed (figure 1.11). The separate classification of primary and secondary arcs is redundant. Instead, by examining the mechanisms of formation of arcs, and the associated displacement vectors, we can summarise all mechanisms by three end member models. These are

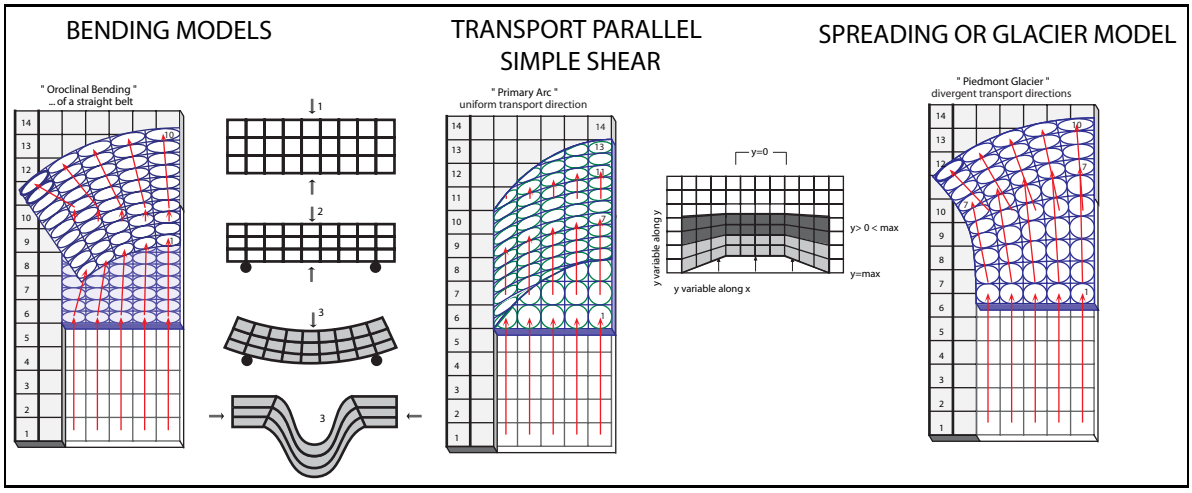

Figure 1.11: New arc classification based on the mechanism of formation leads to three end member models. BENDING MODELS correspond to original definition of an orocline (Carey, 1955): TRANSPORT PARALLEL SIMPLE SHEAR (Ferrill and Groshong, 1993) forms with an initial curvature, which may tighten as the arc develops: SPEADING OR GLACIER MODEL - behaviour like a piedmont glacier, spreads as it advances, will also form with an original curvature, which may tighten.

1) Primary arcs
2) Glacier spreading models
3) Oroclines (secondary bending)

Our primary arc involves a differential displacement along the deformed zone's width. The resulting strain pattern is arcuate. This definition effectively includes several models previously defined as secondary arcs. The glacier spreading idea involves a nappe like body detached and emplaced over an undeformed foreland. The body flows internally, shortening along flow lines and spreading perpendicular to them. The orocline idea is the same as the original definition of Carey (1955); a straight fold belt is bent around some obstacle.

1.2.4 Methods of discriminating between bend types and their mechanisms of formation

Palaeomagnetic

Eldredge et al. (1985) proposed the use of palaeomagnetic analysis of a curved mountain belt to test its method of formation. By comparing the structural trends along an arc (average strike) with the average magnetic declination recorded in rocks from a palaeonorth pole, they believed that three trends would be identifiable. However, their model classifications are to some degree based on those of Ries and Shackleton (1976) and Marshak (1988). Thus, a modified version of the palaeomagnetic end member models is shown in figure 1.12.

1) ORIGINALLY CURVED OROGEN: Could be either spreading Merle (1989) or primary arc models. Smaller change in magnetic declinations than in fold axis trend.

2) ORIGINALLY LINEAR CONFIGURATION: Bending / Buckling - a 'Carey' orocline. Perfect match between fold trend changes and magnetic declinations.

The plotting of a simple graph of the magnetic declination relative to a reference value for the rocks studied against change in structural trend relative to a reference or average trend for the whole arc should be sufficient to show the degree of 'oroclinal' character of an arc. Figure 1.12 shows graphical representations of arcs corresponding to different plots on such a graph. The original concept of Eldredge et al. (1985) contained 'non-rotational' or 'primary' arcs. The Jura mountains were taken as one example of an arcuate belt in the study (Eldredge et al., 1985), and it was concluded that the arc was 'always curved' - suggesting that they are a primary arc.

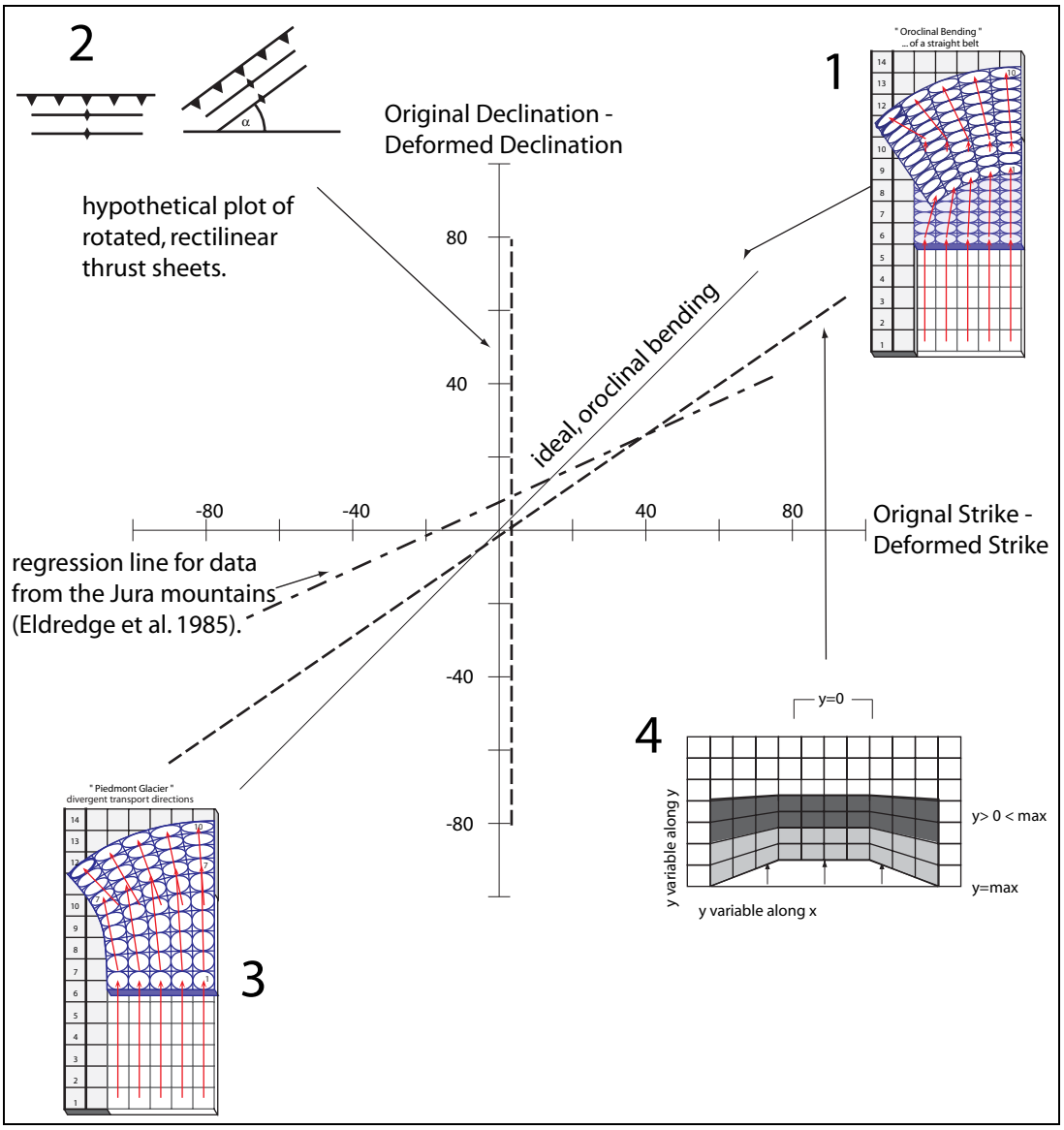

Figure 1.12: The method of Eldredge et al. (1985) for discriminating between end member arc models. It consists of finding the local difference between the averaged trend of strike across a section of an arc, and the local difference between a reference, pre-tectonic magnetic declination and the local post-tectonic one. Hypothetical situations are shown and compared to models. 1) Kinematically possible, involves something eqivalent to bending a beam, and would stretch outer section of arc, tangentially to the strike of the folds. 2) End member model of a passive, rigid body rotation, which would presumably plot somewhere along a line parallel to the y axis. 3) Spreading, or gliding nappe, will involve rotation throughout its development. 4) Transport parallel simple shear, will involve rotation. It is hard to know what the original curvature or average strike will be, but the case should resemble that of a 'tightened' arc.

Gehring et al. (1991) also used palaeomagnetic data from the Jura fold belt to try to discriminate between different hypothetical evolutionary schemes. However, this approach differs, as it tried only to distinguish between models of thick and thin-skinned formation, based on the assumption that thick-skinned models will generate anticlockwise rotations of blocks of up to 20°, whilst a thin-skinned model would require an 8° rotation clockwise. The study favoured a thin-skinned model following the ideas of Laubscher (1961, 1965). Its results allowed the construction of a block mosaic to represent the whole Jura and relied on strain partitioning between large tear faults and thrusts to rearrange the material in the arc.

Finite strain patterns and displacement vectors

All models of arc formation allow some prediction of the strain pattern seen across the deformed zone, and logically, beyond what we may consider to be its limits, within adjacent hinterlands (Ries and Shackleton, 1976; Merle, 1989; Marshak, 1988; Burkhard, 1990; Ferrill and Groshong, 1993).

We can depart on the basis of an analysis of displacement vectors or of finite strains. We can examine both from within the arc itself or from its hinterland. In any of these cases we will rely on making estimates or measures of either quantity in the field or from field data, then comparing it to one of a number of models (which are already presented) for which displacement fields and finite strains can be calculated.

So, our point of departure will be hypothetical geometries of deformation. Other attempts at this sort of analysis have been made, notably Ries and Shackleton (1976), Ferrill and Groshong (1993) and to some extent Marshak (1988). The latter two identified extension parallel to the strike of an arc (tangential extension) as an important quantity. The models presented here differ from this approach, as they rely on finite strains (as did Ries and Shackleton (1976)). Further discussions on the modeling of finite strains in deformed bodies are to be found in chapter 4.

1.2.5 Models applied to the Jura mountains

Palaeomagnetic work in relation to the Jura mountains has already been described. Gehring et al. (1991) interpreted results as lending support to the model of Laubscher (1965). Eldredge et al. (1985) interpreted the Jura as being a 'non-rotational arc' (one where curvature was 'original'), but did not consider the mechanistic consequences of this in detail.

Burkhard (1990) discussed the consequences of four models applied to the Jura arc itself. Using the indenting 'hinterland' - the Molasse, he examined the consequences of several pre-existing models on displacements across it and hence the supposed presence or absence of strain within it. The models are shown in figure 1.2. Two are grouped under non-deformed hinterland, since they both involve rigid body translations of the Molasse Basin into the Jura zone which deforms as a result. The model of pure translation (no rotation) was able to be ruled out since an East-West motion would appear to be required in the Molasse Basin. The rotational model has consequences behind the hinterland, in the Alps and requires extensions which are not found. These two models correspond to those proposed by Laubscher (1961, 1965). It should also be noted that the Molasse Basin shows evidence for at least small deformations (this thesis).

The deformable indenter models show contrasting transport directions, one model having divergent transport across the indenter, which consequently spreads behind the Jura, whilst the other pushes into the Jura by a shearing mechanism (transport parallel simple shear).

The finite strain pattern associated with these two models would differ considerably according to calculations made. However, broad indicators, such as the existence of extension along the length of the arc are not sufficient to discriminate since both models require this.

1.2.6 This Study

We shall therefore content ourselves to place the Jura arc in the context of the mechanistic classification already proposed. the questions this raises are the following:

1. Can we find evidence of shear due to differential displacement?
2. What is the deformation pattern in the hinterland, and which mechanism would this favour?
3. Is it possible to identify secondary bending or to rule this out?

We do this in the light of new data on finite strain from the Molasse Basin, compilations of existing finite strain data across the Jura arc, and an attempt at the restoration of deformed surfaces from the Jura mountains (figure 1.12). We also re-examine the mechanical questions of the Jura thrust sheet in the light of some new data on palaeostress magnitudes from the alpine foreland. Four different aspects of the evolution of the external western alpine arc (Jura/Swiss Molasse) from the Miocene onwards are examined. We begin (section 2) with finite strain measured in the alpine foreland and the Jura arc. We progress (section 3) to the treatment of the displacement field associated with the folding and faulting of the Jura in the region of the canton of Neuchâtel. Again, some arguments about the mechanism of formation of the Jura arc itself are discussed. In section 4 we model finite strain patterns in hypothetical fold belts represented in plan and using very simple rectangular geometries. This exercise allows us to see directly the link between displacement and strain. More arguments about the nature of arcs and their hinterlands are presented. In section 5 we present a paper now published in Journal of Structural Geology, which examines the fundamental questions of the relationship between displacements and finite strains and arc formation models. The possible mechanisms of formation of the Jura arc are discussed in detail and the new and existing finite strain data presented in section 2 are used as evidence favouring a particular arc formation mechanism. Finally, (section 6) we discuss the topic of 'force' in the Jura arc formation by using palaeopiezometry techniques to estimate differential stresses in the alpine foreland during the time of formation of the Jura.

Chapter 2

Calcite Twin Analysis from the Swiss Molasse Basin

2.1 Introduction

Fundamental to our analyses of arcuate mountain belts, are the conditions in the belt's indenter (Burkhard, 1990). Any variations in finite strains across the indenter are an indication of the mechanism that formed the arc. The finite strain pattern from within the arcuate deformation zone is also of great importance. Thus, any new data from the alpine foreland (indenter to the Jura) allow us to evaluate various models for the Jura arc formation. Adding to this the available finite strain data from across the Jura itself allows more precise considerations.

Finite strain data from the Molasse Basin itself is very restricted. The deformations involved are tiny - perhaps of the order of 1-2% by folding. Tectonic compaction (pressure solution / crystallisation) and intracrastylline deformation by twinning in calcite are another expression of minute strains present within this basin. Studies of deformation were previously carried out by (Schrader 1987; Schrader 1988) in the Molasse Basin, using striated or impressed pebbles yielding strain trajectories in the internal parts of the basin containing coarser materials. Major work in the Jura was carried out by Plessmann (1972) who analysed the orientation of horizontal stylolites from across the Jura arc. The new data we are able to add comes from calcite twin analysis across the Molasse Basin. Both the work of Schrader, and the new material presented here show results from Molasse sediments of Miocene age. Plessmann's stylolites come from far older rocks of the Jura. Thus, the direct comparability of all the studies is not certain. The age of the deformation events recorded by Molasse sediments is much more tightly constrained than other studies.

This section presents the new results from the Molasse Basin, and discusses the data analyses in more detail, with a complete presentation of the results and an evaluation of their quality. Data compilations across the region are also presented and discussed. The whole presents a partial introduction to section 5, where the results are discussed and used to propose arc formation models for the Jura as a whole.

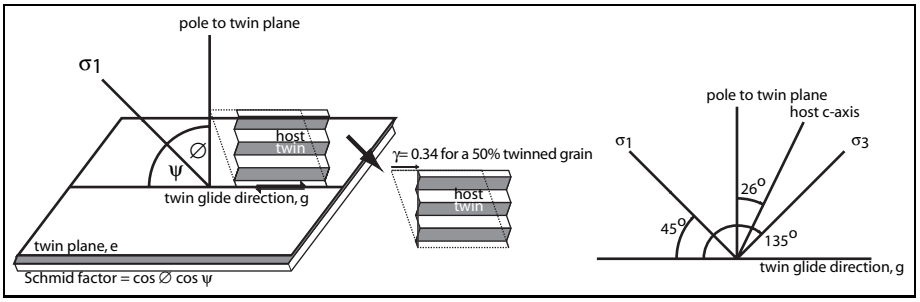

Figure 2.1: Twinning as a strain feature and the Schmid factor: dependent upon the angular relationship between σ_1 and the twin plane pole and glide direction, its value reflects the magnitude of a resolved shear stress across the twin plane (adapted from Jamison and Spang (1976)). Annex shows the g value for the case of a 50% twinned grain (maximum). Lower diagram shows the angular relationships between twin plane and pole and c-axis of calcite.

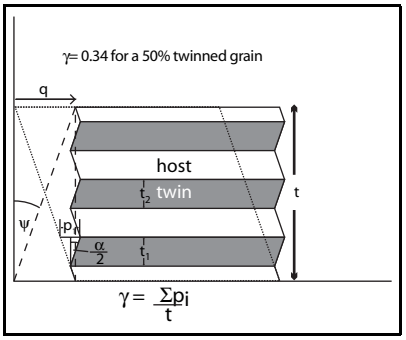

Figure 2.2: Derivation of an expression for the shear strain across the width of a calcite crystal as a function of the number of twins and their thickness. This diagram is adapted from Groshong (1972) and shows how the technique weights each twinset in the regression analysis.

2.2 Calcite Twinning

2.2.1 Mechanics

Twinning of calcite is a low temperature flow mechanism for accommodating strain. Any rock containing calcite crystals and subject to a deformation (at temperatures generally lower than 500°C) will generally show signs of twinning. Twins act as shear planes with a unique sense of shear, in the e-g direction parallel to the twin plane (figure 2.1). Assuming the resolved shear stress acting on a twin plane exceeds a critical value (10 MPa), twinning should take place. Twins may then thicken or new twins nucleate across a grain. The maximum degree of twinning normally visible across a grain is 50% (it may be possible to deduce when a grain is >50% twinned), which represents a tensor shear strain of 17% (half the engineering shear strain) (Groshong, 1972). This sets an upper bound to the degree of strain that can be recorded. Figure 2.1 also shows that a resolved shear stress on a plane will be at a maximum when the compression axis is oriented at 45° to the twin plane and in the positive sense. Thus, twins are formed in response to imposed stresses, recording information about the orientation of compression and tension axes, but they also accommodate strain and therefore behave as strain gauges.

2.2.2 Strain and Stress Gauge Techniques

Since the 1950's, techniques using calcite twins and aimed at orienting the stress and strain axes have been proposed. Turner (1953) proposed a dynamic analysis of twinning from limestones, whereby the compression axes and tension axes are assumed to lie at the optimum angles for maximum resolved shear stresses between the twin plane pole and the c-axis. Projection and contouring of the axes led to fairly close prediction of the applied stress axes.

Strain techniques came later, beginning in the 1960's e.g.. Conel (1962) but then developed in the 1970's (Spang, 1972; Groshong, 1972, 1974). The strain gauge techniques aim to construct a strain tensor for an aggregate on the basis of the orientations of active twin planes across the aggregate and on the degree of twinning of grains from the aggregate. The most sophisticated weighting achieved was by (Groshong, 1972, 1974) who considered the relative thickness of twins summed across a grain and the width of the grain perpendicular to the twin set under consideration to give relative weightings to particular twinsets. Some of this method is outlined here.

Each twinset yields a shear strain in the e-g direction (figure 2.2). We have

$$\gamma_{eg} = \frac{2}{t}\sum_{t=i}^{n} t_i \tan(\frac{\alpha}{2}) \tag{2.1}$$

which for tensor shear strain becomes on simplification (see figure 2.2)

$$\frac{\gamma_{eg}}{2} = \frac{0.347}{t}\sum_{t=i}^{n} t_i \tag{2.2}$$

This expression gives a shear strain for every twinset from every grain measured. The subtlety of the method of Groshong is to transform each twinset shear strain directly into thin section coordinates. This is easily achieved with appropriate direction cosines. Thus,

$$\frac{\gamma_{eg}}{2} = A\epsilon_{11} + B\epsilon_{22} + C\epsilon_{12} + D\epsilon_{13} + E\epsilon_{23}\ , \text{ where } \epsilon_{33} = -(\epsilon_{22} + \epsilon_{11}) \tag{2.3}$$

The coefficients A-E are functions of direction cosines between x,y,z thin section coordinates and the e and g axes. Equation 3 is for one twinset and contains 5 unknowns. Only 5 twinsets make it possible to solve directly for the aggregate strain. We measure generally ∼60 twinsets per sample to take account of a representative average. A best fit solution is then achieved by a least squares method, which allows amongst other things, a quantification of standard errors associated with the solution.

$$\frac{\gamma_{eg}}{2}_{\ i} = \beta_1 x_{i1} + \beta_2 x_{i2} + \beta_3 x_{i3} + \beta_4 x_{i4} + \beta_5 x_{i5}\ , \tag{2.4}$$

where x_{ij} are direction cosine functions for the i^{th} twinset and β_{1-5} are the aggregate strain components for the whole sample. Equation 2.4 is then used to find a matrix expression for the multiple regression,

$$\beta_j = (X^T X)^{-1} X^T Y,\ \ j = 1, 5 \tag{2.5}$$

where β_j is the least-squares estimate of the strain components in the sample. Expressions are also given for the standard error of the analyses Groshong (1972). The aggregate strain can then be compared to the orientations of all twinsets measured to see if the twinning sense is compatible with the aggregate strain. Those twinsets not compatible appear as 'Negative Expected Values' (NEV's). The number of NEV's for any analysis is a measure of the quality of the twin data available. Scattered twinning orientations which prove incompatible with a particular strain tensor may be evidence for complicated, polyaxial strain, and rotation of grains in an aggregate in a strain field. Inhomogeneous strains at a grain or thin section scale will reduce result quality. Further manipulation of data has been suggested in the form of cleaning. Twinsets are ranked for a sample according to the relative shear strain they record. High ranked grains may have a disproportionate influence on the calculated strain tensor, so it is suggested to remove the highest ranked grains from a population before carrying out a least squares calculation.

2.3 Molasse Basin Twin Data

2.3.1 Data Base

We sampled the Obere Meeres Molasse lumachellic sandstones wherever possible from across the Swiss Plateau in a region stretching from the shores of Lake Bourget in France, to Mägenwil near Zürich in the east. In total, 20 oriented samples were taken from different localities (figure 2.8, tables 2.3.1 and 2.3.3 2.3.3) . As samples mostly came from quarries, still active in some instances (e.g. Seiry, canton Fribourg) some concern was initially addressed to the potential effects of blasting quarry faces on twinning. However, pilot studies showed that the strains recorded did not seem affected by dynamiting. Thus, a data base was built of all these samples, with 30 twinsets measured from each of two orthogonal thin sections per sample.

2.3.2 Techniques

All twinset measurements were carried out on a universal stage microscope. Two or three orthogonal thin sections were used from each sample, and generally 30 twinsets per section were measured before combining the 60 measures and processing the data. Data treatment has consisted of Groshong's and Spang's techniques. The results have been cleaned as suggested above, removing the nine highest ranked twinsets for each sample and a significant improvement in data quality has been observed in almost every case. Tables 2.3.3 and 2.3.3 present the orientations of strain axes from both techniques and 'relative' strain magnitudes for Groshong's technique in raw and cleaned form as well as giving sample locations. NEV% values diminish for almost every analysis after cleaning. Orientations change by only a few degrees in most cases. Figures 2.3 and 2.4 show contoured stereograms for each sample prepared from a dynamic analysis. They give confidence intervals for a particular orientation of a compression axis. Groshong technique results are also projected in figure 2.4 for comparison.

Table 2.1: Twin sample locations from the Swiss Molasse Basin, giving, where possible a site description, Swiss grid coordinates of locality and corresponding 1:25000 Swiss geological map if appropriate.

Locations of twin samples from the Swiss Molasse Basin			
sample	grid ref.	location	Swiss 1:25000 sheet
dh2	547.5, 144.0	Chaneaz Thierrens, FR	
dh4	574.6, 201.2	Mt Vully, FR	Murten, 63, 1165
dh5	554.0, 184.8	?	
dh8	553.9, 185.3	Siery, FR	
dh12	552.9, 183.3	?	
dh15	548.2, 156.4	La Fruitière Demide, VD	Lausanne, 85, 1243
dh17	549.3, 164.5	?	
dh19	576.6, 195.6	Münschenwiler, BE	Murten, 63, 1165
dh21	547.7, 169.9	Aliérens, VD	Jorat, 27, 1223
dh22	547.7, 169.9	Aliérens, VD	Jorat, 27, 1223
dh24	548.6, 168.5	Corniez, VD	Jorat, 27, 1223
dh26	542.6, 161.2	Froideville, VD	Jorat, 27, 1223
dh28	544.2, 159.6	Jorat L'Eveque, VD	Jorat, 27, 1223
dh31	617.2, 212.1	Above Heimiswil, SO	Solothurn, 72, 1127
dh32	603.1, 219.3	Above Unterramsern, SO	Solothurn, 72, 1127
dh37	571.4, 208.1	Jolimont, BE	Bieler See, 60, 1145
dh39	467.0, 62.5	St. Pierre d'Alvey, France	
dh40		Alby sur Cheran, France	
dh41	659.95, 251.05	Mägenwil, ZH	
dh42	659.95, 251.05	Mägenwil, ZH	

2.3.3 Data Quality

In general, the NEV% values are low, encouraging confidence in the Groshong technique results. Cleaned data reach lows of 2 NEV% - an almost perfectly compatible set of twins. The majority of the data fall between 10 and 25 NEV%. These data can be considered as reliable. Cleaning procedures have consistently improved the NEV% values (by up to 23 NEV% - sample 28) , so cleaned results are preferred for the study.

The nature of the Molasse sandstones again raises questions about the applicability of a technique. In contrast to pure limestones or marbles used in previous studies, our analysis concerns polygenic sandstone with a high calcite content. Inhomogeneities of grain type and size will lead to stress concentration effects and produce inhomogeneous stresses at even the grain scale. Twinning will occur on grains of many orientations as a result, and resulting aggregate strains will be inhomogeneous in reality. However, the technique will only predict a unique, homogeneous strain tensor for the analysed sample. Over the area of a thin section, we assume therefore that strains are close to homogeneous. The low NEV% values are the best indication we have of such a situation.

Very low strains should also favour high quality results. The Groshong technique relies on the approximation of the small strain tensor Groshong (1972), which is a less precise measure as strain increases due to neglected rotations. This study will not suffer from any significant effects due to this approximation as strains fall in the domain where the small strain approximation is applicable.

2.4 Molasse Basin contour maps and folding

Schüppli (1950) made a contour map of the base OMM layer from the western Swiss Molasse Basin. We have attempted a similar analysis and extended the region covered to make a map scale analysis of the structure of the Western Swiss Molasse Basin Figure 2.5 shows a structure contour map for the USM (Untere Süsswasser Molasse) - OMM (Obere Meeres Molasse) limit. Topography from Swiss 1:100000 maps has been combined with a compilation of Swiss 1:25000 geological map data on outcrop. The data points have been hand contoured. The map shows very gentle folding into closed structures (domes and basins) . No major discontinuities have been identified at the scale of the map. The fold axes trend generally close to east northeast - west southwest. Some very gentle near north-south trending folding is identifiable in the central part of the map. The gentle structures of the basin are not cylindrical. We would propose inhomogeneous, shearing deformation, associated with wrenching of the whole basin to be responsible for their formation. The strain recorded in the folds remains tiny. A cross section across the basin along a line through coordinates 590 170 and 570 210 shows 40 metres of shortening in folding over a profile length of 31 km (ca. 1.3%).

By contrast, in the adjacent Jura, the structural relief of any geological surface is vastly more impressive. Figure 3.1 shows the 3D structure of the Argovien/Sequanien limit for the Neuchâtel Jura based on the map of

Table 2.2: Raw twin strain data from 20 sites in the Swiss Molasse Basin. All sites are within the Obere Meeres Molasse horizon. Results show azimuth and plunge and deformation percentage recorded by groshong analysis, and azimuth and plunge by spang analysis. NEV% is from groshong analysis.

Raw twin strain data from the Swiss Molasse Basin																
	groshongz			groshongx			groshongy			spangz		spangx		spangy		
sample	az.	dip	def%	az.	dip	def%	az.	dip	def%	az.	dip	az.	dip	az.	dip	nev%
dh2	67.0	22.8	-0.13	256.7	66.9	0.14	158.5	3.5	0.007	131.2	7.4	237.1	64.6	37.9	24.1	33.3
dh4	358.0	0.1	-0.19	267.7	61.5	0.18	88.0	28.5	0.005	150.0	3.8	11.5	84.9	240.2	3.4	27
dh5	183.5	23.1	-0.15	91.8	3.9	0.13	352.8	66.5	-0.190	355.8	0.3	85.8	5.1	262.5	84.9	35
dh8	162.8	44.1	-0.18	339.6	45.9	0.14	71.3	1.6	0.040	151.2	38.4	7.1	45.6	256.8	18.7	23
dh12	18.2	8.1	-0.11	152.5	78.5	0.13	287.0	8.1	-0.022	48.6	3.7	156.7	78.2	317.9	11.2	22
dh15	69.6	10.1	-0.21	284.9	77.7	0.15	160.9	7.0	0.062	262.6	10.8	168.1	22.6	16.4	64.7	38
dh17	345.1	22.7	-0.32	254.8	0.8	0.25	163.0	67.3	0.067	352.8	17.7	232.3	57.8	91.8	21.9	22
dh19	275.5	43.4	-0.17	90.1	46.5	0.17	182.9	2.7	-0.005	264.0	28.9	26.7	44.4	154.0	31.8	38
dh21	336.3	3.0	-0.13	67.9	26.7	0.15	240.3	63.1	-0.020	323.3	11.0	66.3	49.3	224.3	38.6	32
dh22	159.1	18.5	-0.19	258.5	26.1	0.14	37.9	57.1	0.050	162.2	20.8	67.0	13.4	306.3	64.9	23
dh24	173.7	8.3	-0.14	358.3	81.7	0.12	263.8	0.7	0.016	168.9	18.4	353.4	71.6	259.4	1.3	23
dh26	165.9	53.5	-0.05	332.8	35.8	0.05	67.3	6.3	-0.002	158.6	41.8	338.2	48.2	68.4	0.2	42
dh28	150.5	8.5	-0.12	56.3	26.0	0.07	257.1	62.5	0.049	152.4	14.7	248.1	21.0	29.9	64.0	25
dh31	131.8	26.2	-0.17	250.2	44.0	0.12	22.0	34.6	0.049	149.3	19.4	39.9	43.4	256.7	40.3	28
dh32	149.0	8.4	-0.21	318.6	81.5	0.20	58.7	1.5	0.309	156.4	10.7	323.3	79.1	65.9	2.4	18
dh37	112.7	13.0	-0.25	216.5	46.0	0.20	11.1	41.1	0.054	323.7	38.8	201.7	33.4	85.8	33.5	23
dh39	106.2	17.4	-0.09	324.9	68.1	0.10	200.3	12.8	-0.003	117.7	16.6	298.9	73.4	207.8	0.3	30
dh40	260.5	12.4	-0.12	109.6	75.9	0.11	351.9	6.7	0.01	290.4	14.5	64.3	69.6	196.7	14.1	21
dh41	29.6	7.5	-0.22	165.5	79.6	0.15	298.6	7.2	0.08	229.3	9.8	77.1	78.9	320.2	5.1	17
dh42	243.3	11.9	-0.12	13.6	72.0	0.12	150.4	13.3	0.0014	247.2	17.3	35.7	70.0	154.2	9.9	12

Table 2.3: Raw twin strain data from 20 sites in the Swiss Molasse Basin. All sites are within the Obere Meeres Molasse horizon. Results show azimuth and plunge and deformation percentage recorded by groshong analysis, and azimuth and plunge by spang analysis. NEV% is from groshong analysis.

Cleaned twin strain data from the Swiss Molasse Basin																
	groshongz			groshongx			groshongy			spangz		spangx		spangy		
sample	az.	dip	def%	az.	dip	def%	az.	dip	def%	az.	dip	az.	dip	az.	dip	nev%
dh2	87.4	15.4	-0.13	222.8	68.9	0.15	353.4	14.1	-0.025	132.5	5.1	233.6	65.0	40.2	24.4	20
dh4	145.4	3.9	-0.13	340.8	85.9	0.14	235.4	1.1	-0.008	147.9	3.9	35.4	80.0	238.5	9.2	23
dh5	183.1	25.2	-0.20	83.7	19.0	0.16	320.8	57.6	0.047	175.9	5.2	84.9	11.4	290.2	77.4	27
dh8	150.3	48.7	-0.14	332.2	41.2	0.12	241.4	0.9	0.012	150.3	38.1	7.9	45.3	256.7	19.7	20
dh12	17.7	8.1	-0.11	148.7	77.7	0.14	286.4	9.2	-0.029	51.3	2.0	152.0	79.1	320.9	10.7	16
dh15	73.9	0.3	-0.17	164.6	63.3	0.09	343.7	26.7	0.071	262.0	11.9	165.7	27.5	13.0	59.6	29
dh17	340.6	14.8	-0.24	235.3	44.9	0.15	84.0	41.4	0.095	352.8	16.0	233.1	59.8	90.4	24.8	12
dh19	275.5	43.4	-0.17	90.1	46.5	0.17	182.9	2.7	-0.005	264.0	28.9	26.7	44.4	154.0	31.8	38
dh21	153.4	2.9	-0.11	61.9	26.0	0.13	249.3	63.9	-0.013	321.7	8.7	61.6	48.6	224.3	40.1	31
dh22	164.1	19.7	-0.20	264.2	26.0	0.14	41.4	56.4	0.054	164.8	22.9	68.8	14.1	309.6	62.7	18
dh24	165.2	18.6	-0.13	5.4	70.3	0.11	257.4	6.3	0.022	163.1	23.2	349.1	66.7	254.0	2.2	22
dh26	189.6	39.4	-0.09	344.3	47.7	0.09	88.8	12.8	-0.004	168.9	38.3	342.6	51.6	76.5	3.1	29
dh28	145.3	3.9	-0.18	46.5	66.0	0.14	237.0	23.7	0.038	152.9	11.5	251.7	37.0	48.5	50.7	2
dh31	144.9	17.2	-0.10	236.5	5.3	0.07	343.0	71.9	0.037	152.3	18.4	45.0	41.8	260.0	42.4	25
dh32	144.3	7.7	-0.28	296.9	81.3	0.24	53.8	4.0	0.035	155.7	9.6	321.1	80.1	65.3	2.5	10
dh37	115.9	5.6	-0.11	210.6	39.8	0.14	19.2	49.7	-0.036	331.0	43.1	201.3	34.4	90.3	27.6	12
dh39	108.2	14.3	-0.10	281.1	75.5	0.11	17.8	1.7	-0.012	118.8	14.3	282.6	75.2	27.8	4.0	25
dh40	260.5	12.4	-0.12	109.6	75.9	0.11	351.9	6.7	0.01	290.4	14.5	64.3	69.6	196.7	14.1	21
dh41	39.5	1.5	-0.16	152.7	86.1	0.11	309.4	3.6	0.050	231.4	9.3	96.3	77	322.9	9.0	12
dh42	232.0	24.0	-0.09	43.8	65.7	0.10	140.8	3.2	-0.02	183.1	23.4	13.6	66.3	274.8	3.9	10

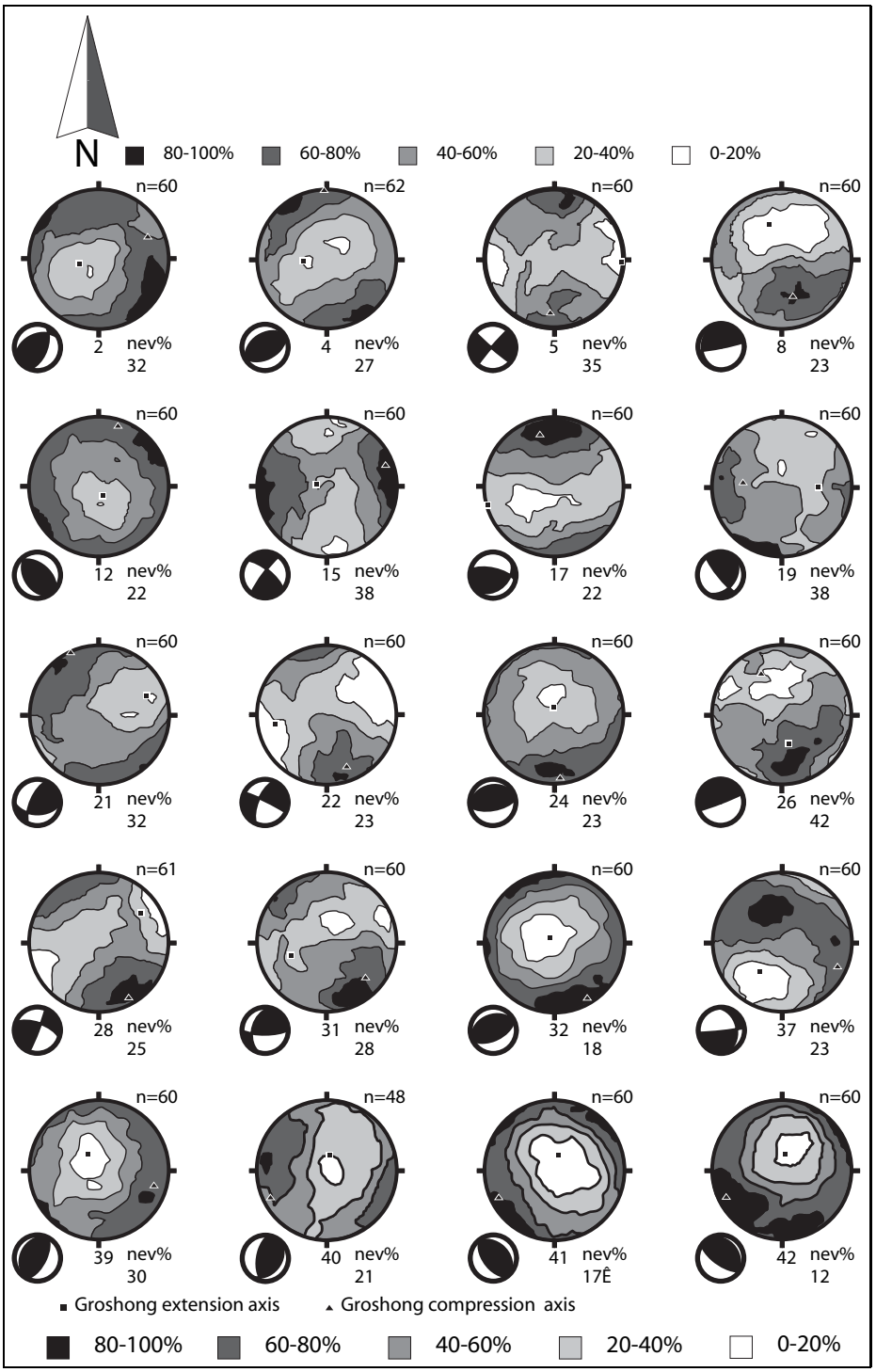

Figure 2.3: Equal area stereographic projection of compression axes contours from calcite twin data for the western molasse basin. The numbers under each stereogram correspond to the map (figure 2.5). Shows confidence intervals for compression axes(80-100% the maximum).Insets are fault plane solutions to show strike-slip or compressive regime. NEV% values and number of twins per sample are shown as NEV% and n respectively. All projections lower hemisphere. Data uncleaned.

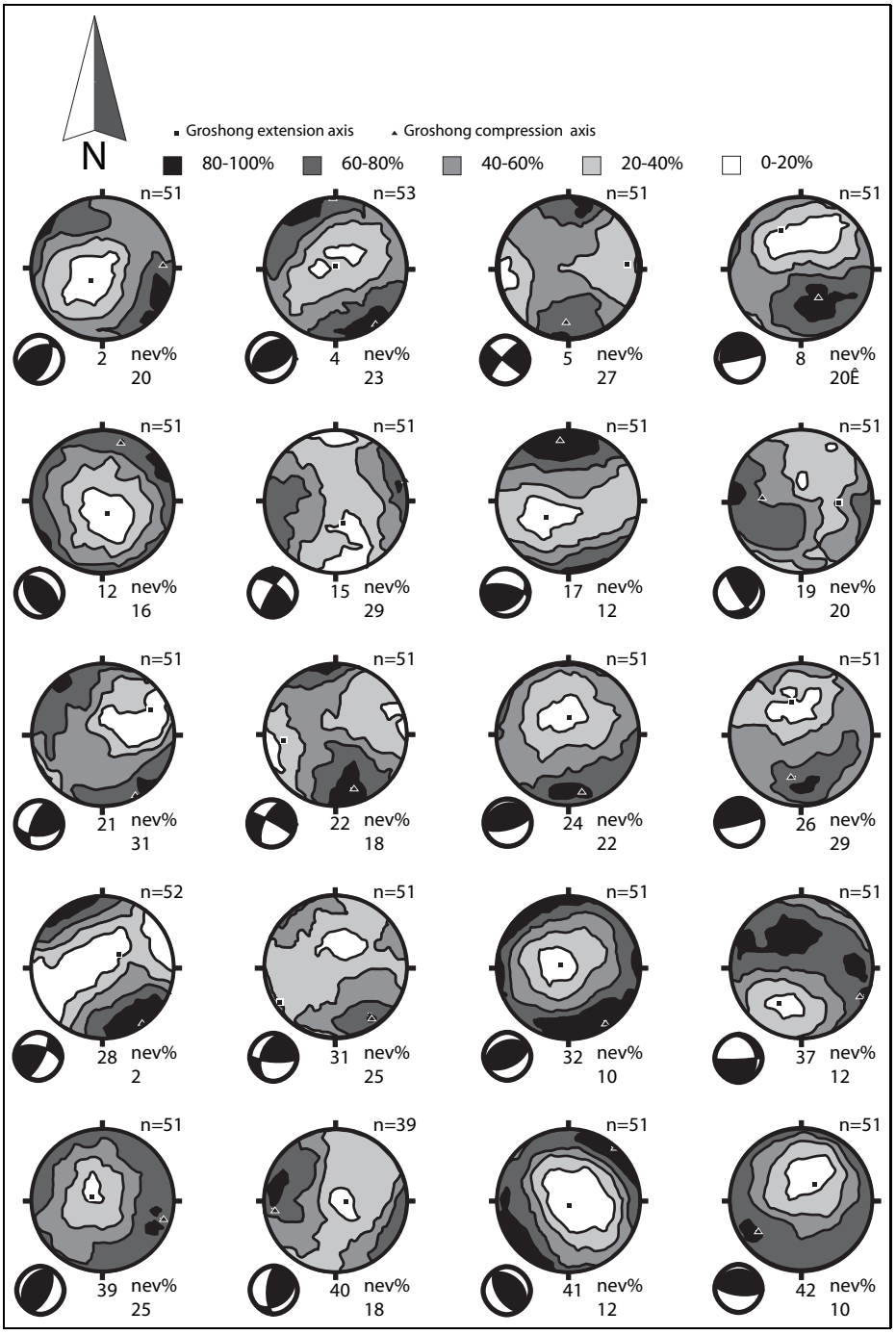

Figure 2.4: Equal area stereographic projection of compression axes contours from calcite twin data for the western molasse basin. The numbers under each stereogram correspond to the map (figure 2.5). Shows confidence intervals for compression axes(80-100% the maximum). Insets are fault plane solutions to show strike-slip or compressive regime. Shortening and extension axes from Groshong method are projected. NEV% values and number of twins per sample are shown as NEV% and n respectively.

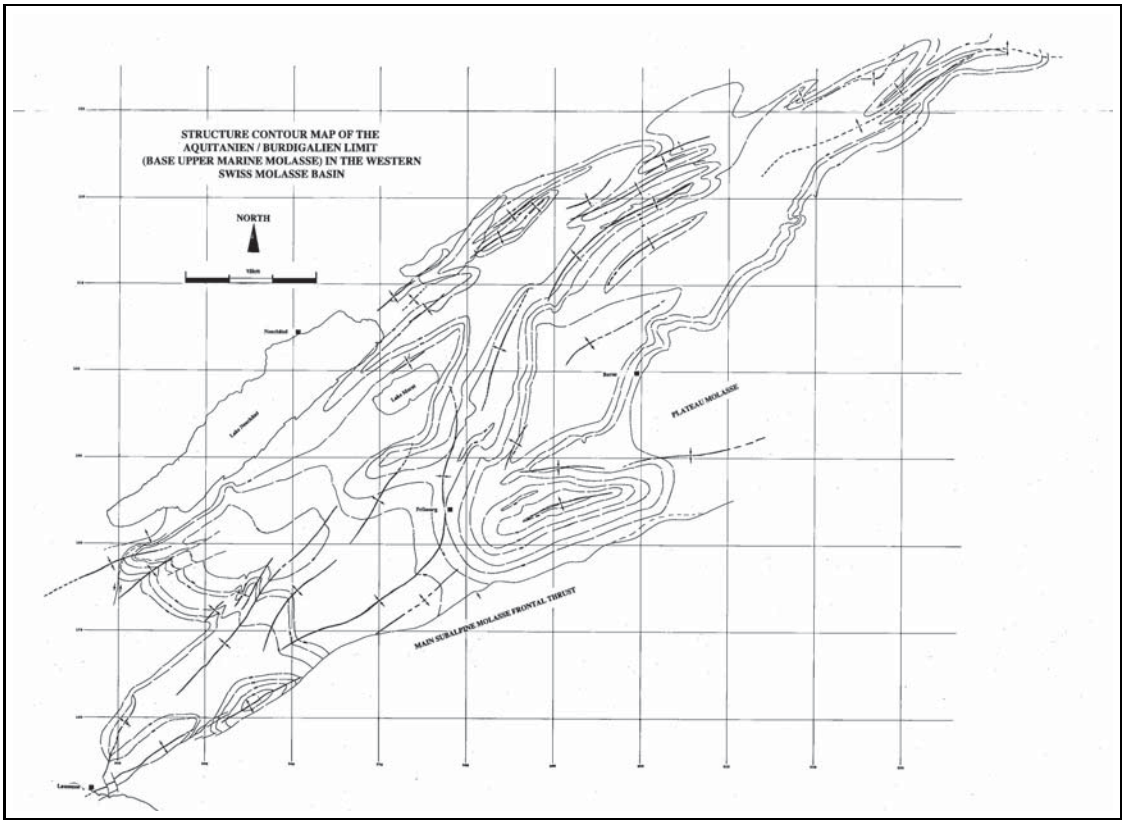

Figure 2.5: Structure contour map of the USM/OSM limit prepared for the Swiss Molasse Basin using available geological maps of the Swiss 1:25000 series.

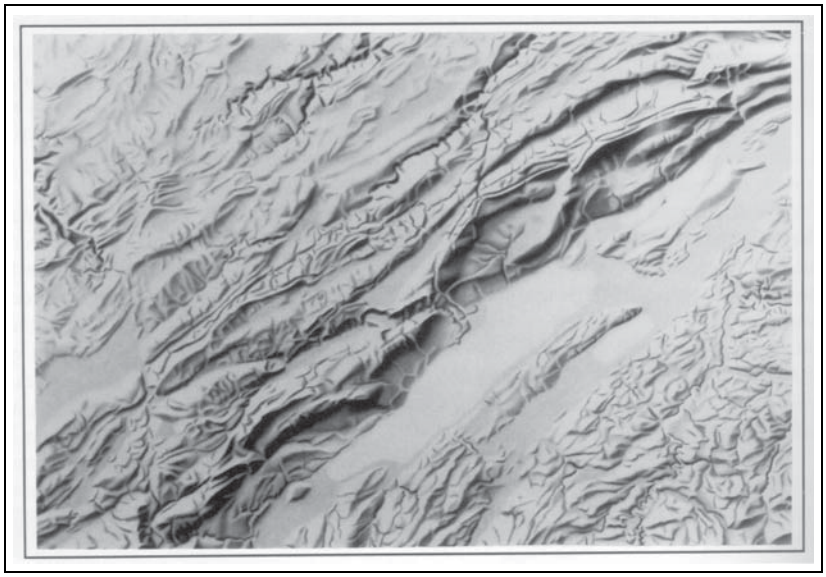

Figure 2.6: Digital topography of a region of the Neuchâtel Jura and afjacent Molasse, showing the lack of relief in the Molasse Basin, in strong contrast to the folding and relief of the Jura.

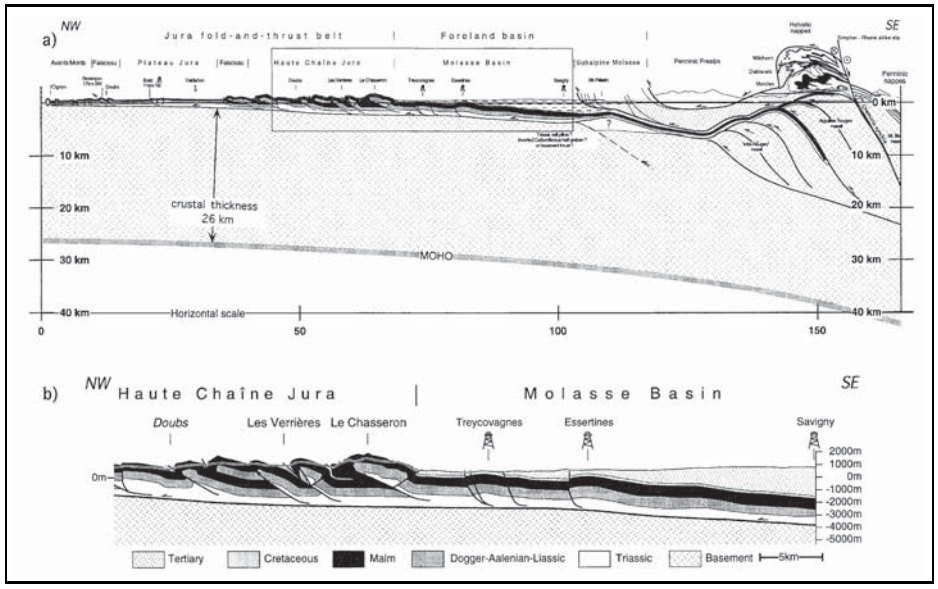

Figure 2.7: Cross section across the Swiss Molasse Basin, (from Sommaruga (1999))

Kiraly. The region shows important folding in variable orientations (similar to the gentle folds of the Molasse in many ways), and considerable thrust and tear faulting. The Jura folds contain easily 5% of shortening across the region. Figure 2.6 shows a digital terrain map for the part of the Molasse Basin and Jura mountains. It demonstrates neatly the difference between the visible, large scale folds of the Jura and the 'invisible' folding of the Molasse Basin.

Figure 2.7 shows two profiles from across the Molasse Basin. The difference between the Plateau Molasse showing virtually no large scale structure, and the more internal Subalpine Molasse is immediately apparent.

2.5 Strike-slip deformation in the Molasse Basin

Numerous authors have sought to link tear faults in the Jura to major strike slip faults supposed to run right across the Molasse basin from the alpine front e.g. Plancherel (1979).Seismic studies in the Jura however (Sommaruga, 1996) have shown the Jura faults to be tears localised above a Triassic detachment. Interpretations of seismic lines across the Molasse Basin (Chenevart, 1978) have been made suggesting that some 'blind areas' correspond to large strike slip faults. Berger (1994) interpreted satellite imagery in terms of 'lineaments' crossing the Molasse basin from the Alps and joining Jura tear faults.

A digital terrain map of the Molasse Basin and Jura (figure 2.6) gives a true impression of the regional topography which is difficult to obtain from normal satellite imagery techniques. The picture it generates shows no evidence for the lineaments identified by Berger and taken to represent large strike-slip faults across the basin.

Whilst the topography of the USM-OMM surface shows folding trending near north-south, we interpret this as due to wrenching deformation over localised lateral ramps developed in the detached cover. This is in accord with a detachment model for the Molasse and Jura. The majority of structures identifiable in the basin still remain proto-anticlines and synclines oriented close to the direction of the basin axis.

2.6 Summary and data compilations

Figure 2.8 presents a compilation of strain data across the Jura and Molasse. Plessmann's stylolite orientations are shown for the Jura, and Schrader's indented pebble data are shown for the alpine foreland. The twin data for this study together with data from previous studies (Plessmann 1972; Schrader 1987; Schrader 1988) are also shown. The orientations of the strain indicators are variable across the region. The western Jura termination shows data often close to east-west. The central Jura and the Molasse behind has orientations ranging between east-west and north-south. The eastern termination of the Jura is a zone where the trends approach northeast-southwest.

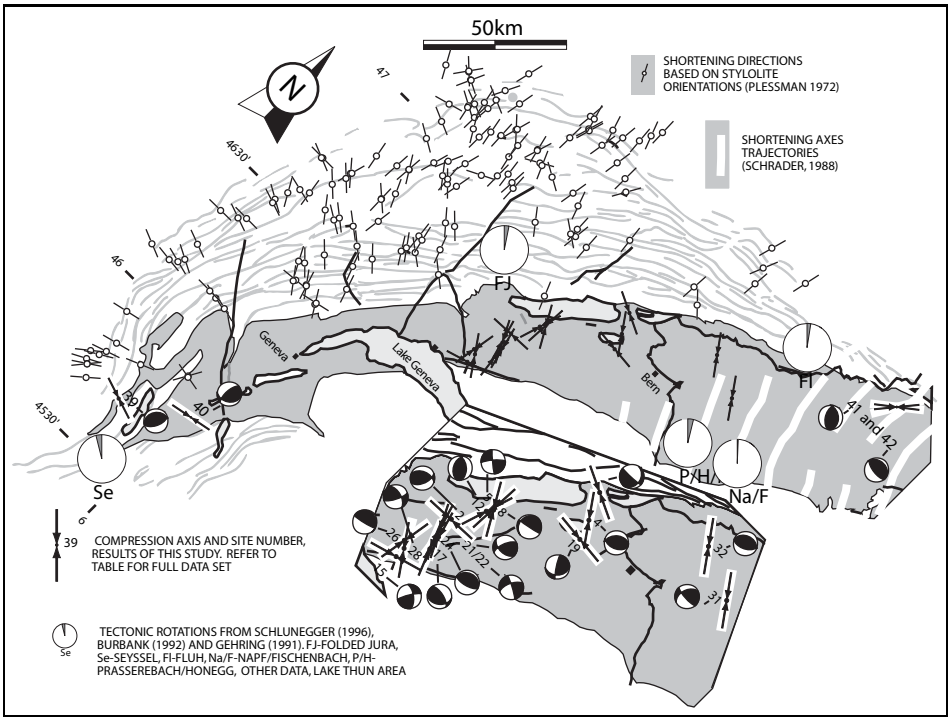

Figure 2.8: Compilation of strain data for the Jura Arc and Molasse Basin. Shows twin strains (this study), indented pebble strains (Schrader, 1988), and stylolite strains (Plessmann, 1972). Also shows fault plane solutions calculated form twin data (this study).

The shortening values recorded by calcite twinning are of the order of only 0.1%. These values are dependent on the value attributed to microtwin thickness, which is not measurable on a normal microscope. Thus, the magnitudes may be underestimates, or they may be the value of strain that twinning could accommodate, but do not represent the total strain in the bed, since other mechanisms operating in parallel will have accommodated shortening. There is no systematic increase or decrease in finite shortening as a function of orientation of the shortening axes. However, given the tiny magnitude of the strain recorded and likely competition with other mechanisms for shortening accommodation, it is unlikely that twinning would detect such small variations.

Thus, we see a broad variation of the orientation of shortening axes across the Jura arc as a function of position. Discussion of the data is presented in tne article in section 5.

Chapter 3

3 dimensional unfolding and restoration of the top-Argovien, Neuchâtel Jura

3.1 Introduction

Tectonic studies on all scales, ranging from continental to that of individual folds or faults, are concerned with the absolute and relative displacement of material points. On the fold or fault scale for instance, we may take the examples of Hobbs (1971) who analysed folding mechanisms and the resultant finite strain patterns, and Ramsay and Graham (1970) who examined the displacement-strain relationships across shear zones. At an intermediate scale, we can take the example of Howard (1967, 1968) who studied the internal deformation of actively deforming regions in California. At a continental scale, we may take the work of England and Jackson (1989). The theoretical analyses of Chinnery (1961) relating displacements to movements on dislocations are applicable at almost any scale. We are confronted with the problem that displacements in palaeo-tectonic studies are not visible or measurable directly. We rely on finding displacements and displacement fields from the process of integration of strains over a region e.g. Cobbold (1977). Only in special circumstances such as neotectonic studies based on geodetic surveys have we the luxury of measuring relative displacements directly. Thus, for most practical examples from folded and faulted belts, we need to determine fold and fault displacements quantitatively.

The external western Alps, forming an arcuate mountain belt, are characterised by folded and faulted cover rocks. We use the removal of the folds and faults together to retrace the movement of material that has occurred during the regions' development. When proposing models of arcuate mountain belt evolution we examine in plan view the displacement field associated with various possible kinematic models (see next section). The total finite strain implied by any such model is also calculated. Thus, both finite strain measures from the field and estimated displacements can be compared with models to check for any correspondence.

The Jura arc has a complicated, non-cylindrical structure along much of its length. Maps around the Neuchâtel area (figure 3.1 gives a 3D representation of the top-Argovien surface) show several orientations of thrust faults which provoke fault related folding. Structures die out along the strike of the mountain belt, implying the relaying of shortening between non-adjacent structures. Any surface from such a region shows complicated fold patterns, and is persistently cut by faults with variable displacement. An existing contour map of the top Argovien (Kiraly, 1969) is a possible starting point for a restoration procedure in a region of the Jura arc, aimed at establishing the likely displacement field. In combining reasonable geological cross sections (to give thrust displacements) and a three dimensional unfolding procedure (to give a more accurate unfolding of complicated structures), we are able to reconstitute a small part of the displacement field associated with the Jura.

3.2 Surface Restoration Techniques

When restoring deformed surfaces, we are quickly confronted with the problem that most deformation is heterogeneous. Variations in principle strain axes orientations and magnitude across a surface make direct restoration by some mathematical transformation practically impossible. Additional problems arise when the surface is (as almost always) faulted, and consequently has a discontinuous distribution of displacement across it.

Lisle (1992) contributed to the understanding of the nature of folded surfaces from structure contour maps. He pointed out the existence of 'developable' surfaces, or surfaces which are isometrically bent. They have suffered no stretch in the plane of the surface at any point, and are consequently restorable by unrolling along special lines called generators. Analysis of a structure contour map by simple methods he proposes in principal allows the identification of regions which are stretched and hence, not 'developable'. Generators will also converge towards faults, as they mark the limit of a developable surface, which should never be infinite (although a cylindrical fold

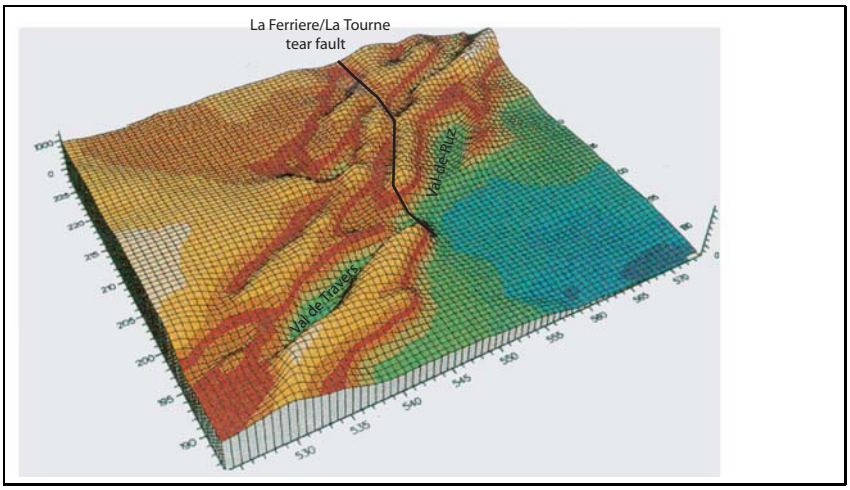

Figure 3.1: The top-Argovien surface, Jura mountains over the canton of Neuchâtel. Also shown is trace of La Tourne/La Ferrière tear fault. Digital model is based on the structure contour map of Kiraly (1969)

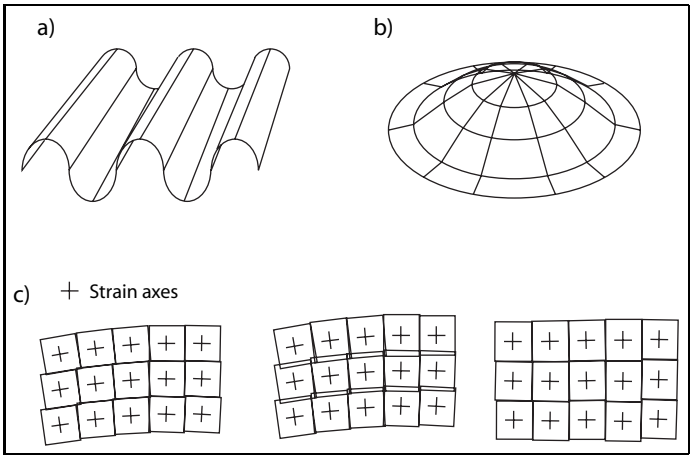

Figure 3.2: Lisle (1992) presented the ideas of isometrically bent or developable surfaces and non-developable surfaces. Cobbold (1979) proposed dividing regions of heterogeneous strain into finite elements whose strain was approximately homogeneous and then unstraining each element before fitting the unstrained elements with minimized voids and overlaps between them. The technique was successfully applied by Gratier et al. (1989) to the Subalpine Chains: a) Developable surface (cylindrical fold); b) Non-developable surface (dome), has in plane stretch. c) finite element decomposition and refitting by division into domains of known strain magnitude and orientation; initial unstraining of elements along strain trajectories; refitting of elements with rigid rotation and translation.

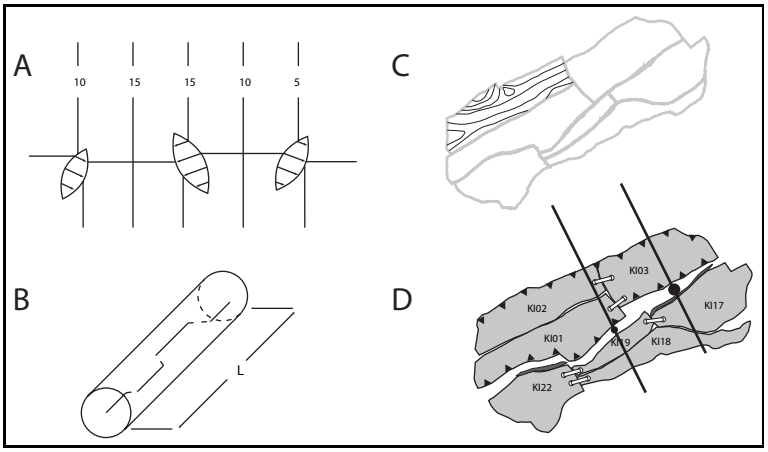

Figure 3.3: a and b) McCoss (1988) reconstitutes the segmented helical loci of originally straight lines on a plane (a). Such a line is shown in its cylindrical envelope (b). Total line segment length divided by the envelope length gives stretch. Differently oriented stretches can be used to construct a strain tensor. c and d) Gratier and Guiller (1993) uses a least squares method to fit triangular elements approximating a folded surface into a flat plane thereby removing folds and reshaping the boundary of the unfolded element of surface. In most cases, fault separations have to be integrated separately from cross sections.

would have generators converging at infinity). Thus, his technique is a predictive tool for finding discontinuities and aids greatly in the general understanding of the surface analysed. However, the practical question of 'unrolling' a developable surface as a means of surface restoration has not (to the author's knowledge) been addressed. It should be noted that most current cross section balancing techniques are based on a constant line length or 'no bed stretch' assumption of a developable surface. How valid such assumptions are is open to question. Two surfaces are shown in the first part of figure 3.2. The cylindrical folds of figure 3.2a satisfy the 'no bed stretch' assumption whereas figure 3.2b, a dome does not.

A so called 'finite element' method has been used as a means of restoring surfaces on several occasions (see second part of figure 3.2c. Cobbold (1979) proposed dividing a region into separate elements whose size permitted the strain within them to be considered as homogeneous. The elements could then be individually restored along the local finite strain trajectories, by the amount that the element was estimated to be strained. Thus, an undeformed configuration would be arrived at for an element. Natural variation of both orientation and magnitudes of strains from element to element will inevitably create both overlaps and voids between the new, unstrained elements. Rigid body translations and rotations are then suggested as being the best way to minimise these voids. After such a rearrangement, the whole surface can be said to be restored.

Gratier et al. (1989) also used a similar technique, applying it to a large region of the external western Alps. Using 15km squares in general, strains were estimated for each domain from at least three differently oriented cross sections constructed across the region. This necessitated the assumption that the fault displacements were relatively small compared to the size of the elements in order to maintain a reasonable assumption of homogeneous strain in each element. The reconstitution of the displacement field for the region was accomplished with some uncertainties, and added complications due to two phases of deformation. A separation of 'Alpine' and 'Pyrenean' phases was also attempted. The accuracy of the cross sections is of primary importance for such a method, but so is the choice of a suitable, undisplaced and undeformed hinterland to which the undeformed elements can be attached.

Schultz-Ela (1988) used a broadly similar approach for the restoration of an Archaean Greenstone Belt. His method successfully dealt with the ductile deformation that the region had undergone.

McCoss (1988) proposed a 'direct' restoration technique for whole regions which could deal with integrated fault and fold strains (see figure 3.3a and b). It relies on determining the length of originally straight lines in the originally plane surface. Constructions for originally straight lines across a folded surface can be made, but problems remain with faults, where slip vectors must be known. Measuring several lines gives the components of a strain tensor by comparing their three-dimensional, deformed length to their original length. The solution nevertheless attributes a homogeneous deformation to an entire region which is not necessarily a reasonable assumption at the regional scale.

Gratier and Guiller (1993) proposed a direct, automated surface restoration technique by approximating a folded surface by a triangular mesh, whose individual elements are then 'laid flat'. In so doing, voids and overlaps of triangles appear which are subsequently iteratively minimised by adjusting the triangle's positions relative to one another. This process works well only for developable surfaces. Hence, starting with a folded and faulted surface, the folds themselves can be removed as a surface restoration but the faults separating them have to be considered apart (see figure 3.3c and d). The method itself allows a more precise treatment of the two components of strain removed by the 'finite element' idea of Cobbold.

Further work on unfolding multi-surfaces has since been carried out (Léger et al., 1997). This method treats several surfaces at once which are unfolded so as to minimise three separate functions simultaneously. The parameters tested are horizontality, in-planar surface strain, and volume conservation. Each parameter can be weighted with more or less importance when finding a least squares solution to the inverse problem. Even this technique cannot deal with integrating fault and fold geometries in 3-dimensions.

Some mention of the work of Laubscher (1965) must be made. He attempted a restoration of both the eastern and central Jura using a 'block mosaic' technique. Using a number of limiting hypotheses about transport and kinematics, he divided regions into fault bounded blocks which he was able to restore by removing fault displacements. He constructed balanced cross sections across the Jura imposing a transport direction on the region. Fault bounded blocks were then displaced by the amount indicated from the cross sections and reassembled. Kinematically, this approach is impeccable. The detail of the work is admirable and the logic of the principles applied is very clear. (Philippe, 1995) also made a large scale restoration of the whole Jura working with block mosaic principles. He was able to reconstruct displacement vectors in this way.

3.3 Unfold Technique

We have chosen to restore the Neuchâtel Jura using the UNFOLD program developed at Grenoble (LGIT) by Gratier and Guiller (1993). The data set we use is the structure contour map of the top-Argovien surface prepared by Kiraly (1969), at Neuchâtel University.

3.3.1 Integrated or Bulk Strain

The concept of integrated or bulk strain is essential to this entire thesis. Numerical models presented in the next section go further to explaining the concept. Integrated strains are essentially reduced to a plane and effect the transformations of the boundary of a region or element (reduced to a plane) to its new position (assumed to lie in a plane too). A displacement field is reconstituted for the total movement of material. Displacement in the x-y plane occurs when a fold forms for instance, so that a line is shortened in the x-y plane. Lines contained in the folded surface are not necessarily changed in length, since they have the freedom to move along z. Length changes are hypothetical ones between two boundaries of an element of a surface shown in a plane. Faults also displace boundaries in a similar manner. Fault and fold displacements are easily integrated once working in a plane.

This is the same as taking a sheet of paper with a pencil line drawn across it. If we fold the piece of paper, the length of the pencil line measured in the plane of the folded sheet is unchanged - no bed stretch. The distance between the two endpoints of the line measured in a horizontal plane is smaller. Thus, the line's 'projection' is shortened.

The relative displacements of element boundaries are real quantities, but the 2-dimensional strain tensors which we can derive from them are physically meaningless from two points of view.

1) The lines in the horizontal plane that they propose to stretch are imaginary. Real lines deform in 3-dimensions
2) A bulk or integrated fault and fold strain does not exist as such in a continuous medium. The faults are discontinuities and violate the principles of continuous media.

Examples of fault and fold displacements reduced to a plane are shown in figure 3.4.

3.3.2 Unfolding in three-dimensions

As already described, the unfolding procedure used (UNFOLD, see Gratier and Guiller (1993)) removes the folding from a surface. In so doing, the boundaries of the element of surface are modified to their undeformed position. Fixing a line element of the boundary allows the relative, local displacements caused by folding to be estimated. Thus, we reconstitute a part of the integrated strain in plan.

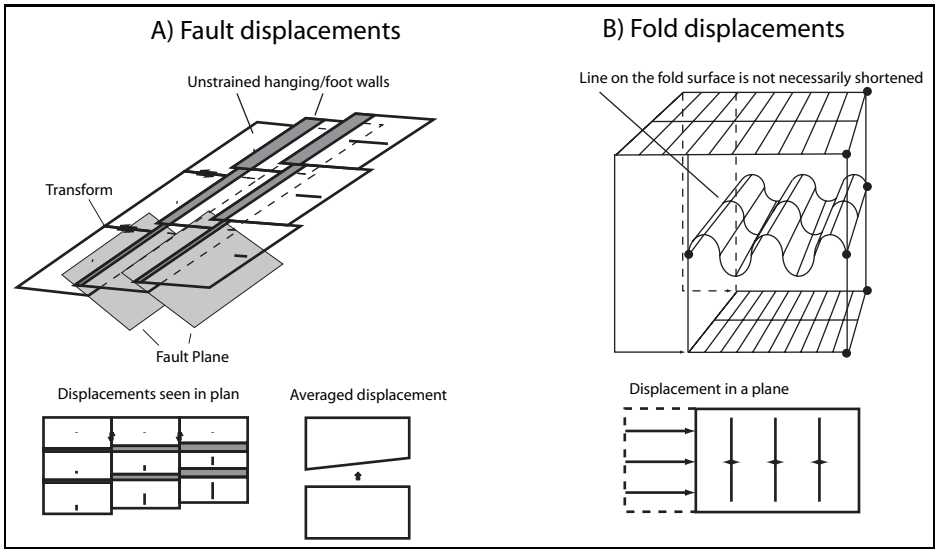

Figure 3.4: a) Fault and b) fold displacements leading to shortening in a 'plan' view of a region. True shortening of lines spanning the region is not necessarily present.

3.3.3 Fault displacements

In addition to folding, especially in a case like the Neuchâtel Jura, an important amount of displacement contained in faults has to be considered. The contour map we used does not show large enough displacements on the thrust faults. Large amounts of the footwalls are missing either due to underestimates on the map or because thrust structures were not recognised, and have been added by constructing balanced cross sections across the region. Thus, the individual elements can be placed into small groups when they have common boundaries, and are in turn separated by faults.

3.3.4 Missing strains

Even when we make an integrated strain across a region, we probably miss quite an important component of shortening. Horizontal 'compaction' of sedimentary layers may accommodate some strain. If the compaction is homogeneous, the layer's bounding surface will remain planar, subsequent folds being able to form in a developable configuration. The importance of such a missing component depends on the material characteristics of the sedimentary layer in question. Estimates of horizontal, layer parallel shortening come from the observation of horizontal stylolites Plessmann (1972). The presence of stylolites in layer parallel orientation around folds suggest a first phase of layer shortening prior to buckling and thrust faulting. Strains due to horizontal stylolites are estimated to be <5%, still large by comparison to 2-5% strains due to folding.

3.4 The Neuchâtel Jura

3.4.1 Structural Considerations

In the context of arc formation models, as already stated, an unknown component remains the displacement field associated with the formation of a mountain belt. Thus, by unfolding the Neuchâtel Jura, we hope to reconstitute a part of the displacement field leading to its formation.

The top Argovien surface exists in the form of a structure contour map over the area shown in figure 3.5. The structure contour map has been divided into 24 separate elements following the limits of faults, or using artificial boundaries where necessary. Each element has been unfolded. Fault displacements across the region have been added from the cross sections shown in figure 3.6. Their traces are also shown in figure 3.5. The cross sections are approximately line length balanced for all except the Cretaceous strata. There is reason to assume that Cretaceous layers deform independently above local dcollement horizons, and undergo tight, short wavelength folding. The remaining layers (from the Malm to the base Liassic are line length balanced. Below the Liassic, we assume a regional dcollement in Triassic evaporites, which has not been balanced. At all times,

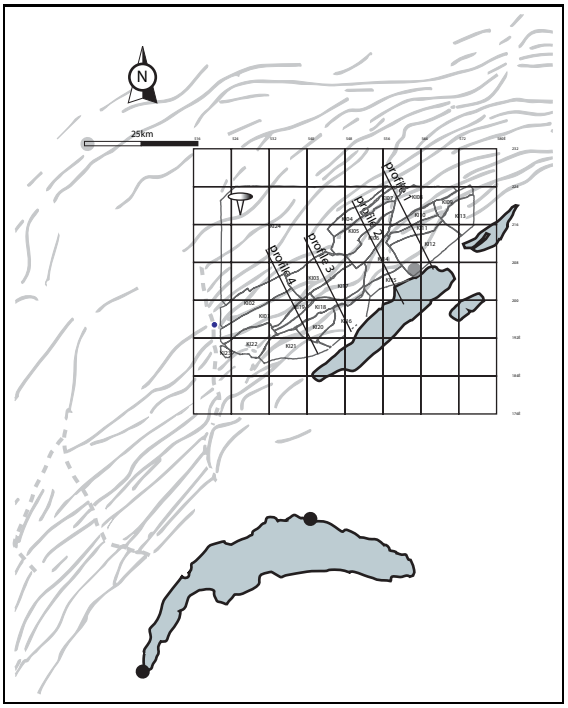

Figure 3.5: The elements used in the unfolding technique. The element boundaries are shown, as are the element numbers. These elements are in the deformed state. The grid is of Swiss coordinates (kilometric).Also shown are the traces of the balanced cross sections constructed across the region.

in fault-related folds, the amount of Triassic material filling the core of anticlines has been kept to a minimum. The basement profile used has come from seismic studies carried out across the region by Sommaruga (1996). Using the same seismic data, depth conversions correlated by several boreholes in the adjacent Molasse Basin give depths for some of the clearer reflectors. These depths are integrated as closely as possible into the profiles, and are particularly useful for placing material in synclines where no surface data is available due to the very thick cover of Quaternary and Tertiary material. Several of the sections cross tear faults. There are balancing problems immediately associated with this. In these cases, we are unable to balance across the tear structure, so balance instead from separate loose lines either side of it.

We have assumed a general north northwest transport direction in the region, and chosen to balance along this direction. Hence, the profiles remain parallel. The largest element (furthest northwest) has been fixed so that its north-south and east-west trending boundaries do not move. All displacements are defined relative to these lines. Thus, starting with the largest element, the other elements are in turn repositioned, with the fault separations added between them. The retro-deformed situation is shown in full in figure 3.7.

The repositioning of elements is not free from some constraints. Elements are linked by three types of limits: a) Thrust faults; since footwall cut-offs are not mappable, missing footwall has been added from cross sections. The retrodeformed picture shows the missing footwall as the white areas between blocks. Thrust faults are restored in plan by keeping a separation corresponding to a circle of the same diameter as the calculated separation of the footwall and hangingwall. This gives some freedom to rotate the unfolded pieces. When trying to satisfy the separations of the same fault measured at several positions along strike, the constraints become severe, and it may be impossible to totally satisfy all the fault requirements. We assume that the separations still remain minimum estimates of displacement and therefore can be exceeded where necessary. Our eventual aim is the best visual fit which satisfies the structural constraints described from the region.

b) Tear faults; these are mapped in the field. Adjacent pieces remain adjacent in the restored map. There is a freedom of movement along the tear faults. Two large tear faults (La Tourne and La Ferrire) cross the region. They therefore have a freedom of movement along their length. By simply restoring the thrust faults in the assumed transport direction, we would create holes along the tear faults. Any such void must represent a part of a footwall. Evidence for large overthrusting along the faults is lacking, and therefore when reconstituting the

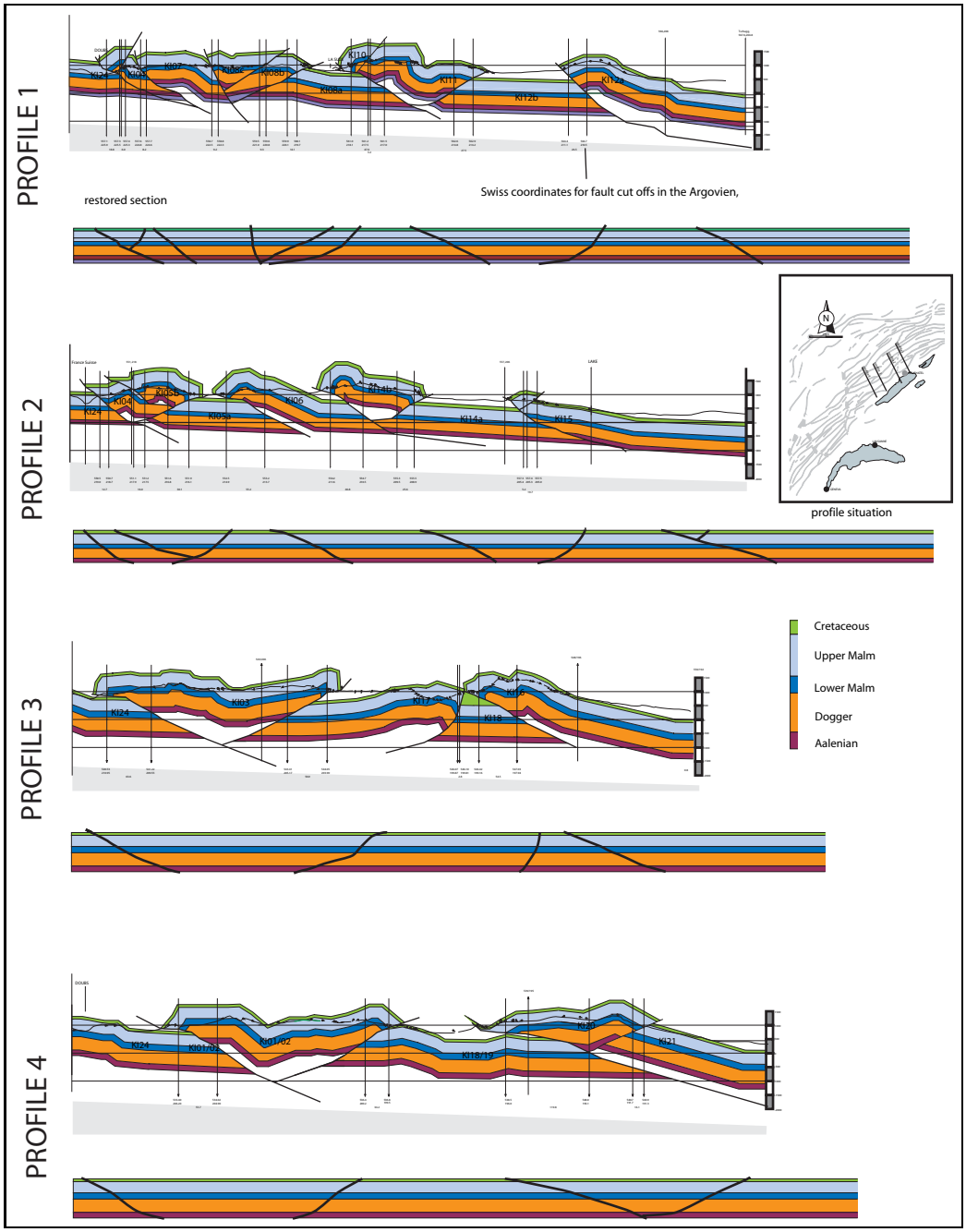

Figure 3.6: Four balanced profiles across the Neuchâtel Jura. Locations shown in inset and also in figure 3.5. Letter number combinations of form KI# # refer to the blocks shown in figure 3.7. Vertical lines mark positions of hangingwall and footwall cut-offs of faults in the Argovien - the offset is used to separate UNFOLD blcoks.

Figure 3.7: The result of retro-deformation, showing the grouped elements separated by thrust and tear faults. The deformed position of the elements is also indicated.

unfolded elements, voids along the tear faults must be reduced to a minimum.

c) Artificial cuts; some elements are cut artificially to link thrust limits for instance. The cuts are necessary to reduce the size of elements, and to keep their form acceptable for the unfolding program. When making a cut, we aim to take it perpendicular to a cylindrical structure if possible. This reduces problems of misfits between adjacent elements which are physically continuous. Groups of elements can then be composed across artificial cuts.

3.4.2 Results of retrodeformation

By taking a regular grid of 8km squares, the displacement of each grid node has been estimated in accordance with the displacement field for the Jura. The finite displacement vectors linking undeformed grid nodes to their positions in the deformed state is shown in figure 3.8. This is the missing quantity we are looking for by the analysis. The displacements are estimated at a scale ($8km^2$) which is perhaps too close to the displacements on the larger faults (up to 2.5km). However, a relatively even gradient of deformation develops across the region towards the fixed lines with respect to which the displacements are defined. Very little 'rotational' or shearing movement can be seen along strike. This suggests that the general deformation of the region should be near cylindrical. There is no drastic lateral displacement gradient.

The bulk strain across the region has been evaluated using an approximation by triangular elements. Each triangle corresponds to half an 8km grid square in the undeformed state and its vertices are translated along the displacement vectors defined at each grid node. Each deformed triangular domain has an associated homogeneous strain. The triangles together approximate the inhomogenous bulk strain distribution across the region. The results are shown in figures 3.9 and 3.10. Table 3.4.2 shows the strain orientations and values for corresponding, numbered triangular elements. The strain field is reasonably ordered, with a tendency of maximum shortening axes to be oriented near parallel to cross section directions across much of the centre of the region. This reflects the overall importance of the faults compared to the folds for accommodating displacement and 'bulk' strain.

3.5 Discussion

Several attempts to find kinematic models for the Jura mountains have already been made. Laubscher (1961) drew cross sections across the eastern and central regions of the Jura, which he divided into fault separated blocks. Their reassembly in plan view lead to a conclusion that there had been a general rotation of material in

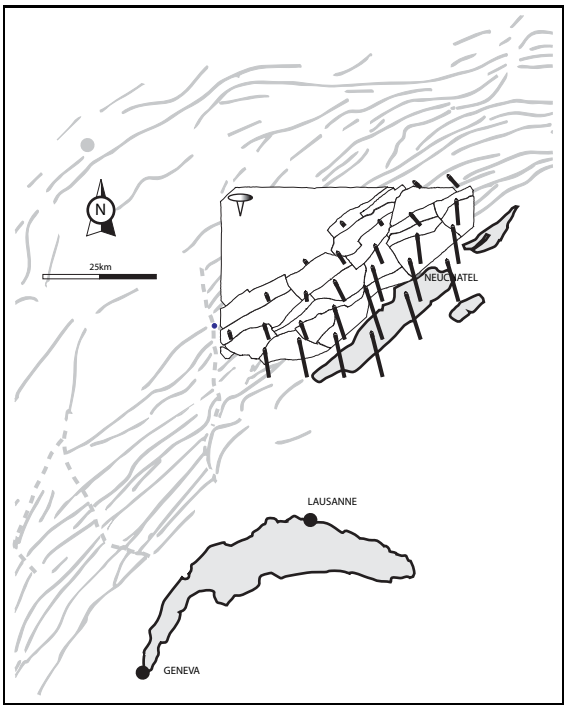

Figure 3.8: The finite displacement field for the Neuchâtel Jura. Showsthe undeformed elements and vectors corresponding to an 8km square grid placed over the region.

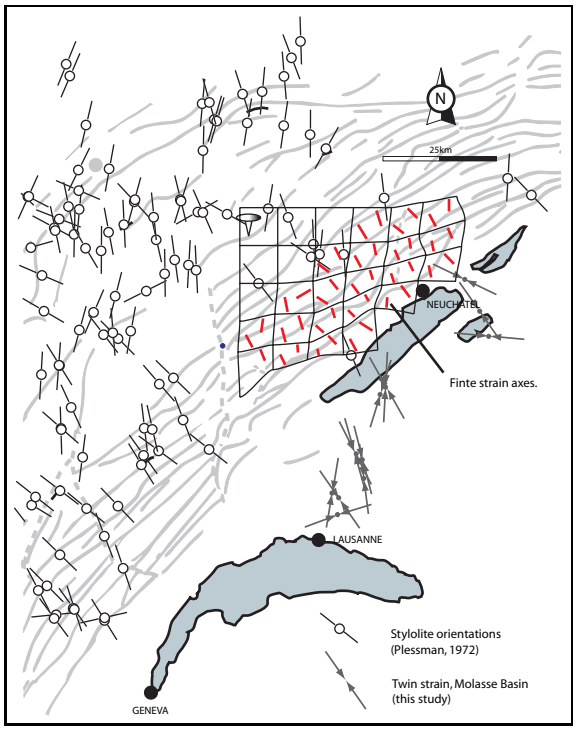

Figure 3.9: Deformation grid drawn from the displacements revealed by the restoration of the Neuchâtel Jura. Shortening axes directions are calculated for the grid (see figure 3.9)

Table 3.1: Bulk strain values calculated from the displacement field generated by retro-deformation of the Neuchâtel Jura. Element numbers correspond to figures. Values given include deviation of short axis from a regional 'transport vector' - assumed to be towards 335°.

bulk strain values for the Neuchâtel Jura					
Triangle no.	e_1 ° from north	e_2 ° from north	$1+e_1$ short axis	$1+e_1$ long axis	° from transport vector
5	26.57	-63.43	0.61	0.96	4.07
6	4.61	-85.39	0.42	0.98	-17.89
7	11.88	-78.12	0.41	0.98	-10.62
8	44.03	-45.97	0.62	1.05	21.53
9	29.38	-60.62	0.85	0.92	6.88
10	62.87	-27.13	0.85	1.12	40.37
17	14.88	-75.12	0.79	0.99	-7.62
18	16.93	-73.07	0.79	1.06	-5.57
19	47.63	-42.37	0.57	1.14	25.13
20	40.66	-49.34	0.56	0.90	18.16
21	44.61	-45.39	0.51	1.06	22.11
22	28.88	-61.12	0.41	1.14	6.38
23	-4.31	-85.69	0.55	1.08	-26.81
24	36.95	-53.05	0.78	1.07	14.45
28	17.02	-72.98	0.54	1.03	-5.48
29	36.50	-53.50	0.64	1.15	14.00
30	25.53	-64.47	0.56	1.21	3.03
31	18.26	-71.74	0.53	1.01	-4.24
32	44.14	-45.86	0.74	1.11	21.64
33	11.45	-78.55	0.65	1.02	-11.05
34	10.87	-79.13	0.64	1.00	-11.63
35	28.29	-61.71	0.71	1.07	5.79
36	9.12	-80.88	0.58	0.84	-13.38
37	23.51	-66.49	0.58	1.18	1.01
38	23.33	-66.67	0.60	1.30	0.83
39	11.50	-78.50	0.58	0.96	-11.00
40	-0.15	89.85	0.65	0.93	-22.65
41	28.19	-61.81	0.74	1.32	5.69
4A	21.92	-68.08	0.64	0.97	-0.58
101	33.78	-56.22	0.74	0.99	11.28
102	37.05	-52.95	0.75	1.02	14.55
103	10.98	-79.02	0.80	1.05	-11.52
104	-59.18	30.82	0.88	1.15	-81.68
105	57.19	-32.81	0.70	0.95	34.69
106	38.67	-51.33	0.69	0.99	16.17
107	53.35	-36.65	0.76	1.08	30.85
108	26.94	-63.06	0.74	0.94	4.44
109	31.43	-58.57	0.88	1.05	8.93
110	17.54	-72.46	0.86	1.02	-4.96
111	51.94	-38.07	0.72	0.99	29.44
112	45.05	-44.95	0.72	0.97	22.55

the Jura system. Burkhard (1990) attempted an analysis at the larger scale of the whole Molasse Basin and the Jura together. His large scale considerations were more directed at the behaviour of the indenter to the Jura. He ruled out several models (including rotation) by consideration of the material balance of the whole Jura-Molasse-Alps system. The western termination of the Jura was analysed by Philippe (1995). He selected a complicated strain-partitioning model for the region.

The new strain data presented here make interesting reading. There is a suggestion that the transport of material is in a nearly constant direction from the map views. This is in accordance with transport parallel simple shear models of arc formation. Table 1 gives precision to such observations. By far the most interesting value in the table in this context is "$1+e_1$". It is a reflection of arc parallel extension, and actually suggests that the Jura has been a little stretched (up to 15%) in places. However, the method used for estimating strains is a smoothed approximation. Enticingly, a trend of extension near parallel to fold axes is observable in some parts of the Val de Ruz basin, possibly agreeing with some of the results of Tschanz and Sommaruga (1993). Extension is generally oriented northeast-southwest, and a marked grouping of extensional regions is visible around the trace of the La Tourne/Ferrière tear fault. Such a feature will concentrate and accommodate necessary stretching produced by transport parallel simple shear, and this will be reflected by a strain approximation technique such as that employed here. These extensional strains are shown in figure 3.11.

The general 3-dimensional restoration of the non-cylindrical folds in the Neuchtel Jura does not reveal very

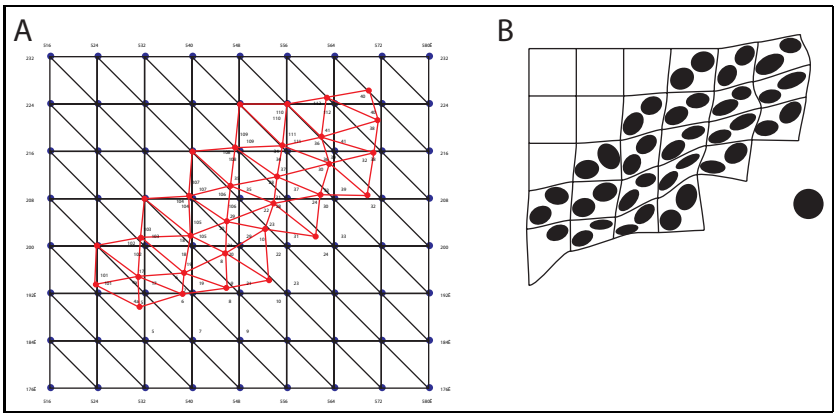

Figure 3.10: Triangular element mesh used to approximate the 'bulk' strain in the x-y plane for the deformation associated with the Neuchâtel Jura. a) triangular grid - each triangle vertex from a regular 8km grid (blue), is transformed along a displacement vector to a deformed triangle (red). The element numbers are paired between deformed and undeformed triangles. Finite strain can then be calculated for each triangle figure 3.9 b) Deformation ellipses calculated from the triangular elements.

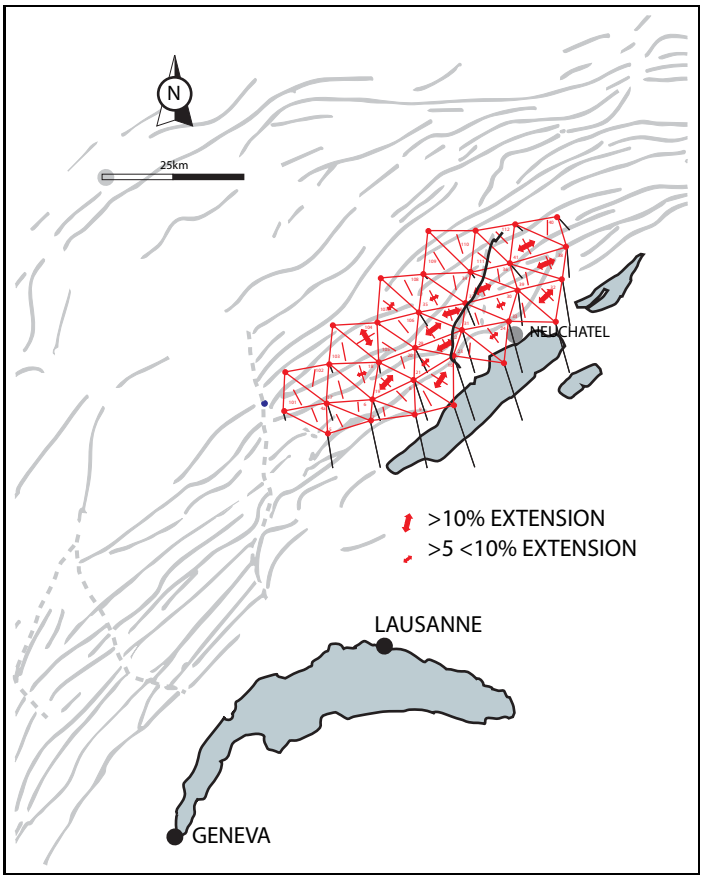

Figure 3.11: extension from UNFOLD for the Jura mountains

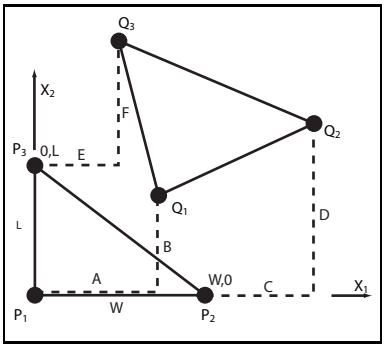

Figure 3.12: The derivation of transformation equation constants from the displacement of the nodes of triangles.

significant strike parallel extension. The presence of folds at up to 40° difference in strike, which locally appear to intersect one another in a dome and basin topography (e.g. Val de Ruz) could even be due to strike parallel contraction. Unfolding these structures and reassembly of the unfolded pieces along tear and thrust faults yields a parallel displacement field with an (overall) near 0% strain in a strike parallel direction (with regions particularly influenced by tear faulting locally showing extension). This is an important finding for arc models. Zero longitudinal strain in the central and frontal part of an arc (the Jura) rules out both spreading and oroclinal bending as arc formation models.

Drawing cross sections forces us to assume a transport direction for the whole region, which is an assumption we wish to avoid since the transport direction is a parameter we are seeking to find. Hence, to some extent, the validity of such analyses is questionable. The best hypothesis remains a cross section, but balancing them will inevitably be problematic.

The bulk strain of the region is a function of the displacements, and as there is no strong along-strike variation, the shortening axes keep a relatively constant orientation. It is questionable at what scale such bulk strain analysis should be carried out, since the 8km grid is probably too fine when compared to the displacements on the faults as pointed out by Gratier et al. (1989). The bulk strain parameter nevertheless lends itself to comparison with the numerical models which follow which treat the arcuate region as a continuum.

The problem thus remains that balanced cross sections make assumptions about the kinematics of a region. However, without good cross sections, restoration of a region is impossible. The addition of the fold strain, removed in three-dimensions is less significant. It also violates cross section balancing principles, as it implies movement of material out of the plane of cross section.

Total solutions to the restoration of an area still rely on two dimensional assumptions, and therefore suffer from some imprecisions, but an alternative three-dimensional model is not feasible for the moment.

3.6 Conclusions

In the Neuchâtel Jura, we have found near parallel displacements. The movements of material to accommodate strain at this scale have not involved significant amounts of rotation. It appears that the combination of folding and faulting allows the strain to be taken up by a transport parallel simple shear mechanism. The shear is small in this region since it is either nearly cylindrical, or since the size of the region analysed is too small to show large variations.

A variety of restoration techniques have been reviewed but only one adopted. At the scale we have worked, the combination of restoration in map and cross section planes is the most appropriate and adds precision. A strain trajectory method e.g. Cobbold (1979) would inevitably miss the small variations of strain in fold structures which unfolding can deal with.

Integrated or bulk strains can be successfully approximated using triangular elements. This gives an extra parameter which one can compare to models of strain in arcuate belts (see next section).

3.7 The triangular element method

The development of the mathematical methods for strain evaluation across quadrilaterals is given in the next section. The case for a triangle is greatly simplified since strain is homogeneous across the whole domain. Con-

sidering a right angled triangle, base W and height L, positioned at the origin (figure 3.12)

$$\begin{aligned} p_1 &= (0,0)^T \\ p_2 &= (0,W)^T \\ p_3 &= (0,L)^T \end{aligned}$$

A general transformation of the triangles' corners can then be described by the position vectors:

$$\begin{aligned} q_1 &= (A,B)^T \\ q_2 &= (C+W,D)^T \\ q_3 &= (E,F+L)^T \end{aligned}$$

We can derive three functions which individually attribute a value of 1. to one point and simultaneously 0. to all others

$$\begin{aligned} \phi_1 &= (1 - \frac{X_1}{W} - \frac{X_2}{L}) \\ \phi_2 &= \frac{X_1}{W} \\ \phi_3 &= \frac{X_2}{L} \end{aligned}$$

and multiplying each function ϕ_k by each new coordinate q_k yields an equation of the form

$$\vec{x} = \sum_{k=1}^{3} \phi_k \vec{q}_k \tag{3.1}$$

The resulting displacement equations take the form

$$\left| \begin{array}{lll} x_1 = \frac{C-A+W}{W} X_1 + & \frac{E-A}{L} X_2 & + A \\ = & & \\ x_2 = & \frac{D-B}{W} X_1 + & \frac{F-B+L}{L} X_2 + B \end{array} \right. \tag{3.2}$$

The deformation gradient matrix from these transformations takes the form

$$\left[\begin{array}{cc} \frac{\partial x_1}{\partial X_1} & \frac{\partial x_1}{\partial X_2} \\ \frac{\partial x_2}{\partial X_1} & \frac{\partial x_2}{\partial X_2} \end{array} \right] = \left[\begin{array}{cc} 1 + \frac{C-A}{W} & \frac{E-A}{L} \\ \frac{D-B}{W} & 1 + \frac{F-B}{L} \end{array} \right] = \mathbf{F} \tag{3.3}$$

As all the terms in eq. 3.3 are constants, the strain in the body is homogeneous. We use the deformation gradient matrix $\mathbf{F}$ to find the deformation tensor $\mathbf{B}$ as follows

$$\mathbf{B} = [\mathbf{F^{-1}}]^{\mathbf{T}} . \mathbf{F^{-1}} \tag{3.4}$$

Hence, if $\mathbf{B}$ has elements

$$\mathbf{B}_{ij} = \left[\begin{array}{cc} a_{11} & a_{12} \\ a_{21} & a_{22} \end{array} \right] \tag{3.5}$$

then the eigenvalues and eigenvectors of the matrix are derived as follows. The eigenvalues are the solution of the equation

$$(\lambda - a_{11})(\lambda - a_{22}) - a_{12}a_{21} = 0 \tag{3.6}$$

This equation has two roots (may be equal or different) which are the two eigenvalues of the strain tensor. These values correspond to the reciprocal quadratic extension. The amount of principal strain in each direction is thus given by

$$\frac{1}{\sqrt{\lambda_i}} \quad i = 1, 2 \tag{3.7}$$

The orientation of the two principal strain axes is given by

$$arctan\left(\frac{\lambda_i - a_{11}}{a_{12}}\right) \tag{3.8}$$

The *largest eigenvalue* will give the *short* axis length (a value of 1 would be unstrained, a value less than 1 shortened, greater than 1 lengthened). The *smallest eigenvalue* conversely gives the size of the *long* axis of strain. Now, the orientation equation is such that the *smallest* eigenvalue gives the orientation, positive anticlockwise from the x_2 axis of the *short* axis (negative goes clockwise from it). The other eigenvector is by definition oriented at 90°

A-F, the constants in equation (3.3) are simply the components of the displacement vectors affecting the vertices of an individual triangular element. Thus, by discretising the Neuchâtel Jura displacement field into a continuous mesh of such triangles, the strain field can be approximated in a *piecewise* fashion. Strain calculations have been carried out using a FORTRAN routine written for this thesis.

Chapter 4

A model of displacement and strain for arc shaped mountain belts applied to the Jura arc

Pre-amble

This section contains the finalised version of an article which appeared in Journal of Structural Geology

D. Hindle, O. Besson and M. Burkhard, 2000, A model of displacement and strain for arc shaped mountain belts applied to the Jura arc, *Journal of Structural Geology*, 22, pp 1285-1296

4.1 Abstract

A geometric model in plan view for simple, parallel, differential displacements is presented. As an analogue for models of arcuate mountain belt formation we use the model to predict strain patterns produced by parallel displacement in front of a rigid versus deformable indenter. A rigid indenter is simulated by an irregular quadrilateral displaced a constant amount along its hinterland boundary. A deformable indenter is simulated by an irregular quadrilateral displaced along a hinterland boundary that is allowed to rotate. Some simple test cases show that the deformable indenter model leads to a pattern of strain very similar to that encountered in arcuate mountain belts. Short axes orientations are most deviated from the transport direction along the lateral edges of the model with minimum displacement and shortening and vary across the central domain, mirroring strain features with variable orientations from mountain belts such as fold trends and minor deformation features such as horizontal stylolite peaks. The rigid indenter model also generates short axes deviated from the transport direction but showing far less variation. Displacement-strain relationships from the Jura mountains (Switzerland and France) are quantified based upon a simplified version of Philippe's (1995) finite displacement field for the Jura fold-thrust belt. We find that the model short axis orientation pattern is very similar over at least the eastern and central Jura to the stylolite patterns from the region whilst the long axes closely match the fold axes trends. The model suggests that the Jura mountains could have formed as a result of a progressive deformation with uniform transport in a general northwest direction.

4.2 Introduction

The form of arcuate fold and thrust belts has long fascinated geologists (Argand, 1922; Carey, 1955; Ries and Shackleton, 1976; Marshak, 1988; Ferrill and Groshong, 1993). Intuitive interpretations of a curved mountain belt suggest the need for radial movement of material to produce the curved fold axis patterns we witness (Argand, 1922; Carey, 1955). Radial displacement of any form will immediately create a space problem for the material in the arc which will have to "stretch" drastically to accommodate the movement (Ferrill and Groshong, 1993). Restoring such a system could lead to all material moving back to a single point - a source-sink. Evidence for the large strike parallel extensions required by such a mechanism is lacking. More careful consideration of the problem has led to the conclusion that material constrained to move in a uniform direction can create strongly curved fold patterns (Ries and Shackleton, 1976; Ferrill and Groshong, 1993). Such differential shear models have, up until now, focused on distinguishing fold-thrust belt curvature forming mechanisms. These studies particularly emphasised the importance of the pattern of tangential elongation as the key parameter for distinguishing between curve forming mechanisms (e.g., transport parallel simple shear, radial thrusting, pure bending, etc.). There has also been some confusion over what are the possible arc geometries resulting from different variants of differential shear. Displacement-strain relationships have sometimes been drawn intuitively, and incorrectly. For instance, both Ries and Shackleton (1976) and Marshak (1988) suggested that uniformly shortened regions with boundaries that are not orthogonal to transport direction would have fold axes orthogonal to the transport direction. This is shown (see figure 4.2, model 1) to be untrue. Often relationships between displacement and strain are counter-intuitive, and only a mathematical derivation of the strain pattern from the displacement field is sure to give correct results. This is an extension of the relationship between displacement and strain of which geologists have long been aware (Howard, 1968; Means, 1976; Ramsay, 1976). If we accept differential shear as a mechanism for arc formation, two model classes can be distinguished based on what happens not in the thrust belt itself, but in the region indenting it. These follow from the work of Hindle and Burkhard (1999) which clarifies the fundamental differences between many proposed arc formation models. We only produce models of the "Primary arc" type defined by Hindle and Burkhard (1999) and give more precise numerical data on the effects of deformation and its relationship to different displacement geometries. The aim is to try and identify which model is the most plausible for forming arcs. Therefore, we demonstrate the rationale of displacement-strain models for very simple, geometric analogues to arcuate fold and thrust belts and then compare these models to a real example, the Jura arc, part of the western alpine collisional system.

The Jura mountains are the latest (Middle Miocene onward) and most external part of the northwestern alpine deformation zone (Sommaruga, 1999). They are a small (ca. 350km long) arcuate (the trend of the mountains varies by 90° along their length), fold and thrust belt, varying in width from 0km at the eastern end to around 65km in their central portion. They have been interpreted as being both a thick-skinned fold and thrust belt with various basement structures thought to be involved in their evolution (e.g., wrench faulting in the basement folding the cover above (Pavoni, 1961), penetration of basement thrusts into the cover (Aubert, 1945), crustal

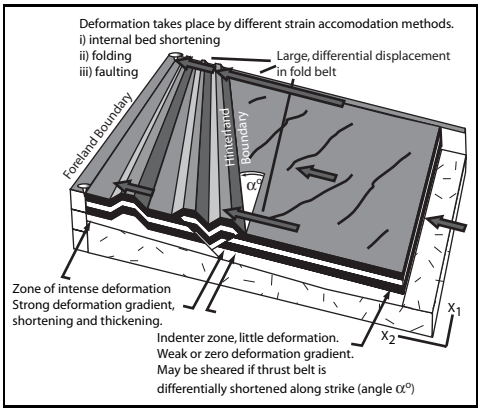

Figure 4.1: A hypothetical fold and thrust belt illustrating the idea of a displacement gradient. In the picture above, there are gradients in the transport direction, which is considered to be unique, and also along strike of the mountain belt, since there is a differential displacement in this direction. The diagram makes a clear separation between an indenter region undergoing passive transport but also lightly deformed by shearing, pushing into a mountain belt which is strongly differentially shortened along strike and which deforms by thrusting and folding. Displacement drops to zero across the width of the fold belt (shown by "pins") creating a displacement gradient orthogonal in the X_2 direction

delamination due to a shallow dipping basement thrust soling out in the crust (Ziegler, 1982)) or a thin-skinned, allochthonous belt, with the Mesozoic cover shortened above an evaporite detachment regionally present within the Triassic (Schardt, 1906, 1908; Buxtorf, 1916; Burkhard, 1990; Sommaruga, 1995; Burkhard and Sommaruga, 1998; Sommaruga, 1999). Most recently, these ideas have been based on regional interpretation of industry seismic lines across the Swiss Molasse Basin and Jura which are now publicly available. When combined with balancing arguments, the autochthonous, thin-skinned interpretation for the Jura mountains is the most reasonable. We base all our modelling on a thin-skinned interpretation. The results of our modelling show that the fold axes trends and orientation of horizontal stylolite peaks (regional strain markers for the Jura) can be simulated by the long and short axes produced by a model of differential shortening with uniform transport direction.

4.3 A simple, geometric, displacement-strain model

4.3.1 Model characteristics

In order to show the effect of displacement of material seen in plan view on the strain pattern within that material we adopt a geometric approach. Mechanical properties of rocks are considered isotropic and homogeneous. A starting point for a model is a quadrilateral. This geometry was used before by Ferrill and Groshong (1993) describing the parallel displacement of material across the length of arcuate fold belts.

With suitable mathematical manipulation (see appendix), we can use any quadrilateral form we wish. However, to create a parallel displacement field, the corners must move in a parallel direction. The behaviour of an indenting region to an arcuate fold and thrust belt is also of considerable interest in these problems. The indenter and thrust belt are joined to each other (see figure 4.1), and any movement of their common boundary must also be present in the indenting region. Consequently, if the common boundary twists or rotates, this component of movement will be present in the indenter too, and should be reflected in the deformation pattern found there. If there is no twist or rotation, but simply a constant translation of the boundary, it is possible that the indenter will behave as a rigid block and show very little deformation. Burkhard (1990) discussed some of the different possible arc-indenter configurations in the context of the Jura arc and identified four models for the indenter, all variants of deformed or undeformed indenters. These broad categories provide useful boundary conditions for the models. A rigid indenter neatly translates into constant displacement of material along the thrust belt/indenter limit, whilst a deformable indenter allows variable displacement along this boundary. We apply the additional constraint of material always moving parallel, and produce four illustrative models, two with an "undeformed indenter", two with a "deformed indenter".

The rigid indenter models (figure 4.2a, and models 1 and 2) have deformed zone boundaries which are oblique to the transport direction of the rigid indenter. The common indenter/deformed zone boundary moves by a constant amount along its width (D1=D2). The same movement distance is applied to every point in the indenter, which

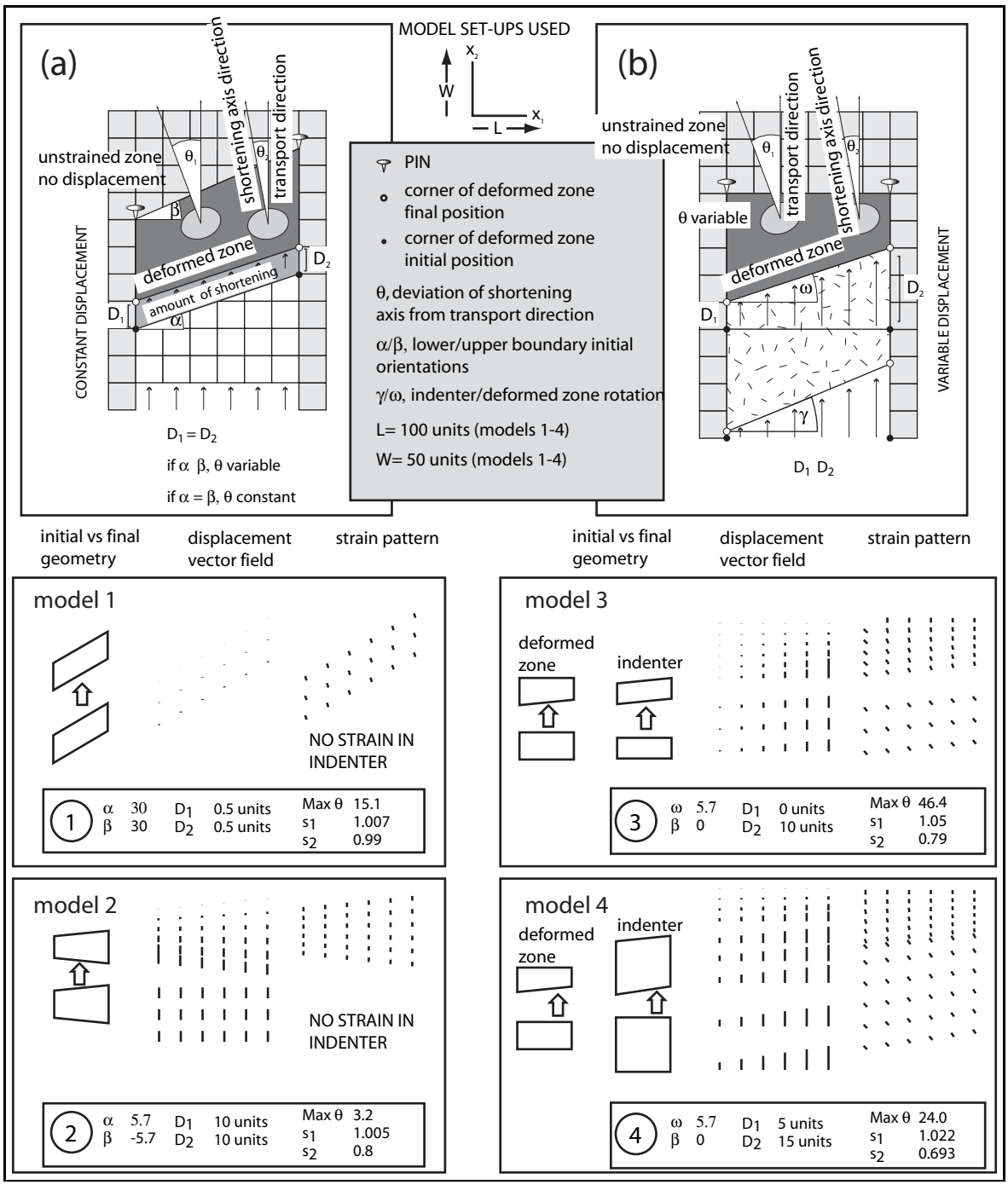

Figure 4.2: Illustrative models for deformation patterns generated by transport parallel simple shear. Two types of model are used, (a) shows a "rigid indenter" and (b) shows a deformed indenter. Model results numbered 1-4 are presented which show graphical plots of both displacement vectors and shortening axes (in their correct orientation) shown to scale and summarise the boundary conditions α, β, ω,D) and the resulting maximum values of shortening and lengthening (s_3 and s_1) and maximum angle (θ) between s_3 and the transport direction in smaller numbered boxes.

undergoes a rigid body translation. Within the deformed zone, the displacement decreases smoothly to zero by the foreland edge of the deformed zone, generating a displacement gradient in the direction of transport. The models vary by changing the inclinations of the foreland and indenter/fold belt boundaries, producing homogeneous (α=β) or inhomogeneous ($\alpha \neq \beta$) deformation.

Such models were seen as analogous to arc forming mechanisms by many authors (Carey, 1955; Ries and Shackleton, 1976; Marshak, 1988). They are a direct analogue to Burkhard (1990) model B, for the Molasse-Jura system where a rigid Molasse Basin pushes east-west, obliquely into the Jura mountains.

The deformable indenter models (figure 4.2b) have a deformed region/indenter common boundary undergoing a rotation (angle ω, which also affects material in the indenter region. The indenting region may have a hinterland boundary undergoing a different rotation (γ). The indenter region is deformed as a result. The "thrust belt" itself will be inhomogeneously deformed as the model is set up with a fixed foreland boundary and a rotated boundary common with the indenter. The two models presented have similar characteristics similar to the transport parallel simple shear idea of Ferrill and Groshong (1993).

4.3.2 Mathematical principle

The quantity known as the displacement gradient is the key to the following models. Displacement gradient refers to changes in the total displacement of points between the original state and the deformed state along a particular direction. Hence, we could define such a quantity along only one co-ordinate axis, and have effectively a one dimensional quantity, or we could envisage it existing in all directions in a plane, and have a fully two dimensional quantity, shown conceptually in figure 4.1. The idea is thoroughly dealt with by Means (1976).

In our analysis of fold-thrust belt curvature formation, we make a distinction between the indenter zone and the fold-thrust belt itself (figure 4.1). The two regions are joined and continuous but there is a jump in the displacement gradient between them. The displacement vectors in the thrust belt diminish in magnitude in the transport direction, reaching zero along the outer boundary of the thrust belt. There is a consequential horizontal shortening (and would be a vertical thickening) of the crust to accommodate the differential movement, which occurs through folding and faulting. The indenter undergoes the full movement of the most translated part of the fold thrust belt, but all parts of the indenter move (approximately) the same distance in the transport direction at least, and hence the displacement gradient and consequently deformation, is very small.

A gradient orthogonal to the transport direction may also develop, resulting in transport parallel differential displacement (or what one may term differential shear). As the fold thrust belt is pinned (see figure 4.1) along an arbitrary foreland boundary, all displacement of material reaches zero along this line. If any point of the indenter region moves further into the fold thrust belt than adjacent points, there is a differential shortening in the fold thrust belt itself according to the position in a direction orthogonal to material transport vectors for the thrust belt. This can be seen in figure 4.1, where displacement vectors have different lengths along this direction. The consequence of transport parallel differential displacement is a transport parallel, differential shear which produces a variable strain pattern in the region. We note (see figure 1) that in many thin-skinned mountain belts, horizontal movement of material is often more than an order of magnitude greater than vertical. In this paper we think particularly of the Jura arc, where horizontal shortening of 25-30km is likely whilst relief due to thrusting is restricted to 1-2km. Hence we can justify modelling displacement and strain in the horizontal plane only (i.e. in map view) and the problem reduces to 2 dimensions.

The displacement gradient can be described by a co-ordinate transformation matrix from which we derive the finite strain tensor for the region. In a simple quadrilateral for instance, there is a relationship between the displacement gradient matrix **F**, and the components of the individual displacement vectors affecting each of the quadrilateral corner points (n=1 to 4) which is demonstrated fully in the appendix. If we calculate this, we have a simple model for plan view strain. We use a quadrilateral domain since this evaluates a continuous function for strain across its domain, equivalent to "averaging" the displacement field due to folding, faulting etc.

4.4 Model Results

We have used four general models, two for undeformed indenters, and two for deformed indenters. They all have uniquely parallel material displacement vectors (assumed to be parallel to the X_2 axis of a general, Cartesian co-ordinate system) and yet all have short axes which are deviated from the transport direction. The degree of deviation varies according to the boundary conditions used. However, any model with a rotational boundary (indenter/fold belt common boundary) generally shows the strongest variability of orientation of short axes. In

all models including those with constant boundary displacements we find differential displacements are generated along any line parallel to the X_1 axis and there are displacement gradients in all directions in the model plane. This occurs in spite of the uniquely parallel movement of material. The general model characteristics and specific results are laid out in figure 4.2.

4.4.1 Model 1

Model 1 involves constant displacement applied to a region of uniform width which is oblique to transport direction. It is a case previously considered by Sanderson and Marchini (1984). He recognised that even though shortening across a region is constant, if the transport is oblique to the region and even if it has a "symmetrical" geometry (parallelogram) a differential displacement is generated. The result is a uniform directed θ (homogeneous deformation) differing from the transport direction (15°). The angle θ will vary as a function of both the obliquity of a region to transport and the amount of shortening.

4.4.2 Model 2

In model 2, a rigid indenter pushes into a zone of variable width and geometry, with both boundaries inclined to the transport direction (β=-5.7°, α=5.7° measured from X_1). The resulting deformation is symmetric about the median line of the deformed zone, and is inhomogeneous. There are only tiny variations in the angle θ. The largest difference between the short axis and the X_2 axis is 3.2°. In the direction of maximum stretch, there is hardly any lengthening (s_1=1.005 maximum). This small difference in orientation of shortening axes reflects the very weak differential displacement along strike in the model.

4.4.3 Model 3

In model 3, we represent a deformable indenter, since the common indenter / deformed zone boundary undergoes rotation. This is a composite model of an arc and its indenter. The deformed zone is initially rectangular in shape, the common indenter / deformed zone boundary undergoing a zero displacement at its left extremity, and a maximum displacement at its right extremity (rotation, ω=5.7°). This produces an inhomogeneous deformation in the deformed zone, as there is no movement of the foreland boundary. To accommodate the movement, the indenter behind the deformed zone must also be sheared. In this case, both a homogeneous simple shear and shortening is applied to the indenter, which undergoes a small shortening and an equal rotation (=simple shear) of its foreland and hiknterland boundaries. Deviations of shortening axes from the X_2 direction are far greater with this configuration. Maximum deviation occurs along the left hand (unshortened) edge, where the state of strain is simple shear only. The remainder of the deformed zone is increasingly shortened resulting in lower angular deviations. A surprising consequence of this model is the 0° deviation of shortening axes along the upper boundary where the state of strain is pure shear only. This implies an instantaneous passage at some point from θ >45° to 0°. Assuming fold axes perpendicular to the local direction of s3, the model would produce a series of curved folds becoming progressively more parallel to X_1 in the positive X_1 direction (similarly along X_2). There is also considerably more (up to 1.05) extension in the direction of the long axis.

4.4.4 Model 4

Model 4 contains the following important features. The deformed zone is shortened by a translational component of the common indenter/deformed zone boundary, in addition to a differential displacement of this boundary along strike. The indenter region also undergoes a differential shortening along strike. It is sheared to accommodate the displacements in the deformed zone, however, its hinterland boundary rotates more than its foreland boundary, creating differential shear (γ=8.5°). Moreover, a small shortening component is applied to the whole zone (less than that applied to the deformed zone). Every point in the indenter has an additional translation applied to it. The translation is of the same amount as the additional shortening applied to the deformed zone. The indenter thus configured has a strain pattern with the deviation of shortening axes from X_2 decreasing in both positive X_1 and X_2 senses. The result of additional shortening in the fold belt region of the model is to reduce the deviation of shortening axes from the X_2 direction (compare to results for model 3 for instance).

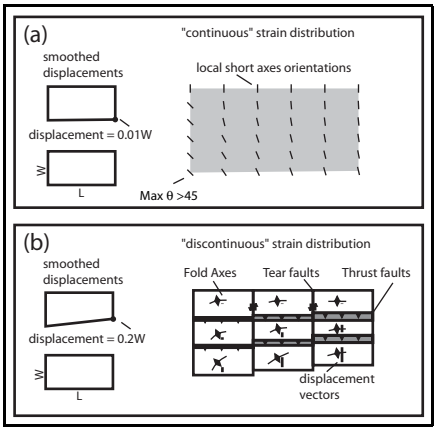

Figure 4.3: Finite strain accumulates in small increments but the geometry of each increment may remain relatively constant over time. Small deformation features form from the onset of deformation whilst large scale ones (faults and folds) form after many increments. (a) shows a tiny increment of transport parallel differential shear. The resulting fanning strain pattern has θ >45 ° along one lateral edge of the model and θ = 0 ° along the opposite edge . Early strain features like stylolites should exhibit this sort of strain pattern too. (b) shows a larger amount of transport parallel differential shear, which could be thought of as resulting from 200 increments of (a). Deformation mechanisms change to accommodate the larger strain (shown schematically). Once faulting has begun, most new deformation will accumulate on faults, and the system will behave as a series of differentially translated, semi-rigid blocks. However, earlier formed, low deformation features would be present within these blocks and may preserve their original orientations.

4.4.5 Discussion

The model results demonstrate how differential shear in a deformed region leads to strains which are highly variable in both orientation (θ) and magnitude (stretches, s_1 - maximum extension and s_2 - maximum shortening). Differential shear is generated by both uniform displacement of the lower boundary to an irregularly shaped region or by rotation of a lower boundary of a regular or irregular region. Rotations cause large differential shear and consequently larger maximum θ and s_1/s_2. Any general, additional shortening across the region (D1>0), leads to a reduction in maximum θ (see difference between models 2 and 3).

The geometries shown are scale independent and analogous to many geological situations. In arcuate mountain belts, we may examine the relationship between fold axis orientations and other finite strain markers such as stylolites or calcite twins, and transport direction of material in the region. We may assume predicted θ to be locally parallel to stylolite teeth and at 90° to fold axes. The conclusion would be that a configuration such as model 2 would resemble an arcuate mountain belt in many ways. However, this is slightly unrealistic since in a mountain belt, at such high strains, a large amount of displacement is taken up by faulting.

Indeed, all the deformation accumulated by different mechanisms in a thin-skinned thrust belt can be thought of as accommodating some regional scale strain. The important thing to remember is the progressive nature of the deformation. Features such as stylolites and possibly some heterogeneities provoking early folding would begin forming in the very earliest stages of deformation of a region (figure 4.3a) when total strain is very low. This initial geometry of deformation may still be similar to that seen at the end of the episode. Indeed, the total finite deformation for transport parallel simple shear could be thought of as accumulating by a succession of increments such as in figure 3a. Taking a similar rectangular domain as we have used for our first strain models, we apply a tiny displacement to one of its corners (figure 3a) and simulate one such increment. We see that even the smallest differential shear will give θ >45°. If this is the deformation geometry affecting an arcuate mountain belt, we would expect early strain features such as stylolites to form with orientations similar to predicted θ. Some early folding (and possibly faulting) could also be initiated in the same orientation. Further deformation (figure 3b) would be accommodated by faulting and folding, and may occur by translation of discrete, semi-rigid blocks. However, already formed folds and stylolites would keep their early orientations, which might be rotated passively if the differential shear continues.

Therefore, though the detailed processes governing formation of strain features are complicated, the orientations and patterns we find should be related to the geometry of deformation applied. Our modelling simulates the average or total strain applied to a region which may be accommodated by a number of mechanisms. Reches

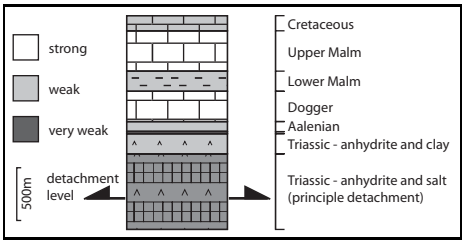

Figure 4.4: Mechanical stratigraphy for the Jura mountains, adapted from Sommaruga (1999). Thicknesses shown are correct for the central Jura mountains, but vary across the chain as described in the text. The main dcollement layer is illustrated by thrust arrows, and the approximate relative strengths of the lithologies are shown according to the shading of the units.

(1978) also suggested that groups of faults act together to accommodate regional strains and their orientation would have a clear relationship to the regional scale strain field that was developing. Even for simple homogeneous strains, four differently oriented fault planes would exist. Molnar (1983) suggested an inverse process where earthquake magnitudes on differently oriented faults could be summed to give an average regional strain. Both point to the fact that faults (and folds and intergranular deformation) are allowing change of shape of a large region. We argue that at the scale of a whole mountain belt, an overall deformation geometry exists and this is the key to the regional strain pattern we find.

4.4.6 The Jura Arc example

Taking these arguments further requires a real example. The Jura fold and thrust belt is an arcuate region of more than 350km lateral extent, lying northwest of the northern alpine foreland basin (Swiss Molasse). The belt is composed of thrust Mesozoic strata detached from a Permo-Carboniferous basement by Triassic evaporite layers. Lateral thickness variations and pinch-outs of the Triassic 'Muschelkalk' and 'Keuper' series are a major control on displacement and shortening of the cover sequence over the width of the chain and its arcuate form (Debrand-Passard et al., 1984; Philippe, 1994). Following Sommaruga (1996), the mechanical behaviour of the Jura strata can be broadly characterised as follows (see figure 4.4): Limestone dominated lithologies are generally strong and brittle; shale and marl dominated lithologies are weaker and may be either plastic or brittle according to associated temperature, fluid pressure and relative amount and type of clay; evaporite dominated lithologies are weak, and generally plastic. Hence, the lowermost, salt-gypsum-dominated Triassic units of the Jura are mechanically by far the weakest, and form the principle basal dcollement whilst the Upper Malm, a thick, limestone unit is by contrast very strong and has deformed under a brittle regime across much of the belt to produce the fold-thrust system we see today. The Jura mountains contain remnants of the Tertiary foreland basin Molasse sequence proving that the foreland basin's foredeep unconformity extended into the chain before it was formed. In the alpine foreland basin, hinterland to the Jura, the same Mesozoic layers dip below Molasse sediments up to 3km thick at the alpine front. The entire wedge of Molasse and Mesozoic material remains relatively undeformed. Contractional deformation of the Mesozoic sequences in the Jura mountains develops from the post-Middle Miocene (Serravallian), onwards (Burkhard and Sommaruga, 1998).

Previous models of curvature formation in the Jura belt can be summarised according to two types of approach used. The first are based on 2 dimensional, plan view restorations of the Jura (or parts of it). Hence, Laubscher (1961) originally formulated a model involving rotation of the Molasse/Jura limit, by 7° in the eastern part of the Jura mountains, constrained by the variations in shortening estimated along the strike of the belt from 2d restoration. This model implies that the Jura mountains are then indented by a Molasse region which would also have been sheared. More recently, Philippe (1995) produced the most complete 2 dimensional restoration of the Jura belt yet. The displacement field he derived relative to a pin line in the stable European foreland to the Jura shows an explicit rotation of the Jura/Molasse boundary, which could also mean that the Molasse Basin is a deformed (sheared) indenter. The second group of interpretations are based on static models for stress patterns suggested by different strain features found in the present day Jura belt. Laubscher (1972) for instance, suggested a conceptually different model for curvature formation where the indenting block was effectively the western Alps (Helvetic and Prealpine nappes) pushing as a rigid block into the Molasse and Jura (i.e. both are indented but only the Jura shows significant deformation). This interpretation was chosen because the (instantaneous) stress pattern generated by such a rigid block pushing into a deformable hinterland would resemble a pattern of stress

trajectories related to the variable orientation of the fold axes across the belt. Homberg et al. (1999) have recently proposed a modified indenter model in which the Molasse Basin is the direct indenter to the Jura arc; furthermore, Homberg proposes that this indenter would have broadened over time. The broadening is used as an explanation for two differing orientations of stress axes determined from sets of Mio-Pliocene fault slickenslides which pre or post date folding in the Jura.

The difference between the two approaches is manifest. The first, by attempting to unravel the displacements which produced the structures found in the Jura will, if carried out correctly, restore the positions of the Jura/Molasse boundary to its original position before deformation. If this limit changes shape (e.g. twists) between the undeformed and deformed states, the Molasse Basin must also have been internally deformed. The second approach attempts to find a model based upon analyses which are related to an instantaneous state of stress. As such, they ignore the large differential displacements along strike of the mountain belt accumulating over time. The arguments related to stress states are correct but do not take account of the dynamic evolution of the system over time.

We have adopted the results of Philippe (1995) and modified them slightly to model the total finite strain for the displacement field generated by 2d plan view restoration of the Jura belt. Our model is simplified because rather than allowing a slight divergence of displacement vectors, we take only the displacements of four points along the Jura/Molasse boundary, and constrain them to be parallel (in an approximately northwest direction). We then pin the Jura/foreland boundary. Finally, as we model total finite strain by such a technique, i.e. strain from displacement (in reality due to cumulative faulting and folding), we interpolate the displacements to decrease linearly to zero along the Jura/foreland boundary, from the values given along the Jura/Molasse boundary. These values are close to 30km shortening (maximum) along the central and western Jura boundaries, but decline to zero at both the western and eastern Jura culminations. We substitute a continuous displacement function for what is in nature discontinuous and calculate a cumulative finite strain pattern for the Jura mountains, based on the sum of all displacement during their history. We compare the model strain data with observed strain features such as folds and horizontal stylolite peaks. The four points of known displacement are actually simulated by using quadrilateral domains as in the illustrative models.

Our results give directional information for short and long axes of the total finite strain ellipses predicted across the Jura. A rigidly parallel displacement field (figure 4.5a) produces a fanning strain pattern (figure 4.5) across a modelled Jura arc. Comparison with field data shows predicted short axes not fanning as strongly as stylolite teeth (figure 4.5b), with angular deviations of approximately 45° between measured and calculated values at the eastern and western terminations of the Jura. Predicted long axes orientations (figure 4.5c) match those of Jura folds across most of the eastern and central Jura with deviations of $<10°$. Calculated strain axes swing by 73° in orientation across the model, which we may compare to the often quoted 90 swing in orientation of the Jura structural grain along strike.

There are probable mechanical reasons for the difference in correspondence between the large, cumulative finite strains and different natural features. In the case of the stylolites, as already discussed (figure 4.3a), small deformations produce a widely fanning strain pattern, and since deformation is small, this would correspond closely to local principal stress trajectories. We also notice two contrasting orientations of stylolites in some places in the Jura. This has been interpreted as corresponding to two different regional stress fields. Other kinematic indicators (e.g. fault slickenslide analysis cf. Homberg et al. (1999)) also show these two trends. Such instantaneous measures of stress (or tiny strain) are not directly comparable to total finite strains. The fanning pattern is present for both model and natural data. However, deviations from transport direction are always lower in the case of the model where total shortening is large. The additional shortening component tends to pull strain axes closer into line with transport direction. Fold axes by contrast are far larger scale features and form over the course of the total deformation history of the mountain belt. The model is in very close correspondence with fold axes trends, since we compare the model to a quantity more representative of cumulative finite strain. This admittedly only offers a qualitative explanation, and the precise mechanics of the processes involved are far more complicated. Nevertheless, the likely overall geometry of total finite displacement in the Jura even when constrained to be rigorously parallel everywhere, produces the divergent pattern of strain we see in the Jura arc. It may be invoked as a mechanism for generating the arcuate geometry of the whole belt. There is no requirement of divergent transport along strike or secondary bending.

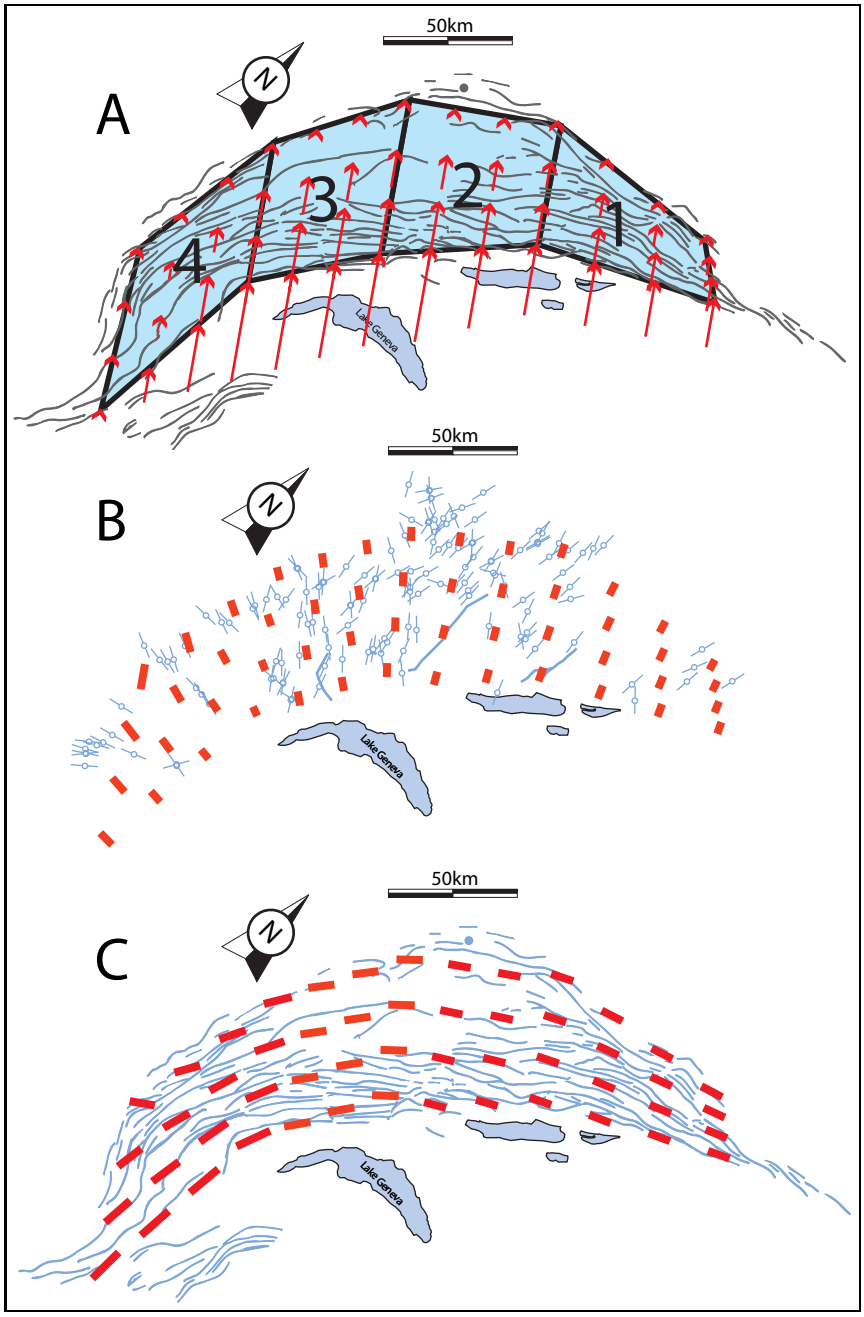

Figure 4.5: Modelling the Jura using 4 quadrilateral domains. a) The displacement field of Philippe (1995) is simplified to 4 points on the Jura/Molasse boundary, displaced differentially, in an identical direction. Jura/foreland boundary is fixed relative to these points. Four quadrilateral domains model the boundary conditions, and displacements (red vectors) are smoothly interpolated across them. Note that here, we pass from a reference element (rectangular) to two different deformed elements as outlined in the appendix. b) Short axes calculated for the displacement field (red) compared to horizontal stylolites from the Jura (blue). c) Long axes calculated for the displacement field (red) compared to fold axes from the Jura (blue).

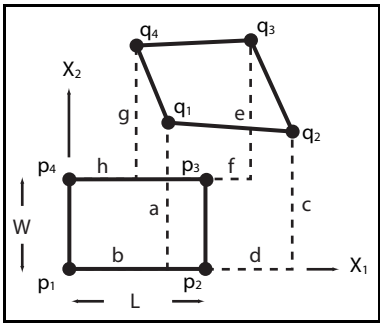

Figure 4.6: Deriving transformation constants. The components a-h are shown positioned according to the equations derived in the appendix. All models begin from a reference element with dimensions L,W as shown.

4.4.7 Conclusions

1. Illustrative models of transport parallel shear have shown any region inclined to transport direction undergoing constant displacement of one boundary will develop a fanning strain pattern, divergent from the transport direction.
2. If a regions width varies along strike and its boundary is moved a constant amount (even if the boundary is orthogonal to the transport direction) the shortening is consumed differentially along strike, generating a differential shear and again giving a fanning strain pattern, divergent from the transport direction. However, the degree of divergence for such a case is normally very small.
3. When a boundary of a region is displaced differentially along strike, the resulting fanning strain pattern is very clear, and shows strongest divergence from the transport direction along the line for which shortening in the model is a minimum. When shortening is zero along one line in such a model, the predicted strain axes along this line will diverge by at least 45° from transport direction.
4.In general, these models illustrate that differential, parallel displacements of material in a region will generate fanning strain patterns.
5. A model of the Jura arc, allowing only parallel displacements and variable amounts of differential displacement and shortening along strike produces a fanning strain pattern across the width of the model region.
6. The orientations of stylolite teeth measured in the Jura (and also other kinematic indicators e.g. fault slickenslides) show a similar fanning pattern but a stronger deviation from an assumed transport direction. Local angular differences of ca. 45° in orientation are found. Discrepancies most probably stem from modelling large, finite strains, and comparing them to features probably developed at a much earlier stage (lower strain) cf. point 3.
7. Fold axes trends, a measure of the 'structural grain' of the Jura arc, show a very close match to the orientations of modelled, long axes of finite strain ellipses (modelled variation along strike is 73°, change in trend of the Jura is ca. 90°). We attribute this to the fact that fold axes orientations develop over the entire deformation history of the belt, and consequently are closely related to the total calculated finite strains.
8. We conclude that geometrically constrained models of arcuate fold and thrust belt indentation give valuable information about the evolution of the indenter. Based on the evidence of several restorations (Laubscher, 1961; Philippe, 1995), the Molasse Basin has been deformed as it has a common boundary with the Jura arc, shown to have been rotated. Moreover, applying the finite displacements predicted by such a model generates a fanning strain pattern. Models of indentation based on stress patterns developing ahead of a rigid indenter (Laubscher, 1972; Homberg et al., 1999), predict fanning stress/strain patterns, but are instantaneous solutions to a problem. They ignore the accumulation of incremental strains over time and the changes in geometry of the system that this requires.

Appendix - Mathematical Derivations

Figure 4.6 shows the general set up for the model. We see an initial rectangular element, $\mathbf{p}_n$(n=1 to 4), dimensions (L,W) transformed onto a general quadrilateral, $\mathbf{q}_n$. The components of the vectors linking the two are named individually. These transformations give:

$$p_1 = (0,0)^T \Longrightarrow q_1 = (B,A)^T$$

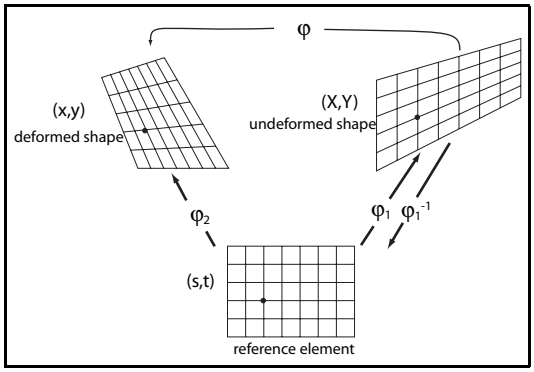

Figure 4.7: Although we want a single function φ, it is easier to work from a reference element and carry out two separate transformations. We therefore work between three separate co-ordinate systems, (s,t), (X,Y), (x,y) defining the original coordinate grid in (s,t). Functions mentioned in the text are shown schematically.

$$p_2 = (L, 0)^T \Longrightarrow q_2 = (L + D, C)^T$$
$$p_3 = (L, W)^T \Longrightarrow q_3 = (L + F, W + E)^T$$
$$p_4 = (0, W)^T \Longrightarrow q_4 = (H, W + G)^T$$

We then derive four functions which individually attribute a value of 1 to one point $\mathbf{p}_n$ and simultaneously zero to all others (shape functions)

$$\phi_1 = (L - x_1)(W - x_2)\frac{1}{LW}$$
$$\phi_2 = x_1(W - x_2)\frac{1}{LW}$$
$$\phi_3 = x_1 x_2 \frac{1}{LW}$$
$$\phi_4 = (L - x_1)\frac{1}{LW}$$

Now multiplying each function ϕ_n by each new co-ordinate $\mathbf{q}_n$ yields an equation of the form

$$\vec{x} = \sum_{n=1}^{4} \phi_n \vec{q}_n \tag{4.1}$$

where $x = (x_1, x_2)^T$ is the transformed co-ordinates of a point.
The resulting displacement equations take a general form

$$\left| \begin{array}{l} x_1 = a_{11}X_1 + a_{12}X_2 + a_{13}X_1X_2 + a_{14} \\ x_2 = a_{21}X_1 + a_{22}X_2 + a_{23}X_1X_2 + a_{24} \end{array} \right. \tag{4.2}$$

We then differentiate with respect to X1, and X2 in turn. This gives us the deformation gradient matrix.

$$\frac{\partial x_i}{\partial X_j} = \left[\begin{array}{cc} a_{13}X_2 + a_{11} & a_{13}X_1 + a_{12} \\ a_{23}X_2 + a_{21} & a_{23}X_1 + a_{22} \end{array} \right] \tag{4.3}$$

The matrix can be used in the manner $\mathrm{d}\mathbf{x} = \mathbf{F}.\mathrm{d}\mathbf{X}$, thereby associating a vector at initial position $\mathbf{X}$ to another vector at final position $\mathbf{x}$. This specification (sometimes called Lagrangian) refers to the undeformed configuration. We find it more relevant to work in a deformed (Eulerian) configuration, since when making field measurements, we work in deformed material and ignore its initial position. We therefore prefer a specification $\mathrm{d}\mathbf{X} = \mathbf{F}^{-1}\mathrm{d}\mathbf{x}$, and require the inverse of the tensor $\mathbf{F}$. Various strain and deformation tensors exist and are well presented by Malvern (1969) (chapter 4). We use the Cauchy deformation tensor $\mathbf{B}^{-1}$. This gives the initial squared length ($\mathrm{d}S^2$) of an element $\mathrm{d}\mathbf{x}$ identified in the deformed configuration.

$$\mathbf{B}^{-1} = [\mathbf{F}^{-1}]^{\mathbf{T}}.\mathbf{F}^{-1} \tag{4.4}$$

So, we have the general displacement equation for the rectangle onto any quadrilateral. If we wish to take a general quadrilateral as the initial shape and deform that, a solution is also possible. We work from an initial rectangular element - a reference element. Equations (4.2) govern the transformation of the rectangle onto both any initial quadrilateral and any final quadrilateral. Thus a co-ordinate point (s,t) in the reference element (figure 4.7) is associated to a point (X,Y) in the initial configuration by application φ_1 and to a point (x,y) in the final configuration by application φ_2. Both applications φ_1 and φ_2 are of the form of equations 4.2. A global application φ can be imagined which directly associates a point (X,Y) to a point (x,y). It is equivalent to the composite function

$$\varphi_2(\varphi_1^{-1}(X,Y)) \text{ or } \varphi_2 \cdot \varphi_1^{-1} \tag{4.5}$$

It is also equivalent to associating either 'end' of the equations

$$\varphi_1(s,t) = (X,Y)) \text{ and } \varphi_2(s,t) = (x,y)) \tag{4.6}$$

By using (s,t) this way, we can effect a co-ordinate transformation of a known point in all co-ordinate systems, without directly knowing φ_1^{-1}. To calculate deformations, we need to know $\mathbf{D}\varphi$.

$$\mathbf{D}\varphi \;=\; \mathbf{D}(\varphi_2 \cdot \varphi_1^{-1}) \;=\; \mathbf{D}\varphi_2 \cdot \mathbf{D}(\varphi_1^{-1}) \;=\; \mathbf{D}\varphi_2 \cdot \mathbf{D}\varphi_1^{-1} \tag{4.7}$$

We need to find $\mathbf{D}\varphi^{-1}$

$$\mathbf{D}\varphi^{-1} \;=\; \mathbf{D}(\varphi_2 \cdot \mathbf{D}\varphi_1^{-1})^{-1} \;=\; \mathbf{D}\varphi_1 \cdot \mathbf{D}(\varphi_2)^{-1} \tag{4.8}$$

Then, like equation 4.4

$$\mathbf{B}^{-1} \;=\; (\mathbf{D}\varphi^{-1})^T \cdot \mathbf{D}\varphi^{-1} \;=\; (\mathbf{D}\varphi_2^{-1})^T \cdot \mathbf{D}\varphi_1^T \cdot \mathbf{D}\varphi_1 \cdot \mathbf{D}\varphi_2^{-1} \tag{4.9}$$

Acknowledgements

Very helpful reviews by David Ferrill and François Jouanne have substantially improved the scope of the manuscript. This study was supported by Swiss National Science Foundation Grants No. 20-43055.95 and 20-50535.97; it is a part of the PhD thesis of DH.

Chapter 5

Strain, Displacement and Rotation associated with the formation of curvature in fold belts; the example of the Jura arc

Pre-amble

This section contains the finalised version of an article which appeared in Journal of Structural Geology

D. Hindle and M. Burkhard, 1999, Strain, Displacement and Rotation associated with the formation of curvature in fold belts;the example of the Jura arc, *Journal of Structural Geology*, 21, pp 1089-1101

5.1 Abstract

A new simplified genetic classification scheme for arcuate fold-thrust belts is proposed. Based on total strain patterns and displacement vector fields, we distinguish three extreme end member models : 1)'Oroclines', pure bending of an initially straight belt, 2) 'Piedmont glacier' with divergent transport directions and 3)'Primary arcs'. With a simple geometric model set-up for the simulation of strain patterns in Primary arcs with uniform transport direction, we demonstrate that divergent strain trajectories and rotations of passive marker lines do not require any divergence in displacement directions. These often quoted arguments are insufficient for the identification of "Oroclinal bending" or 'Piedmont glacier' type of arc formation. Only 3-D restorations of an arc do provide the critical information about displacement directions. In their absence, arc parallel stretches and rotations in comparison with total strains provide the most useful criteria for the distinction of arc formation modes. As an example, the Jura fold-thrust belt of the external Alps is discussed. A large set of strain data includes total shortening estimates based on balanced cross-sections, local strain axes orientations from the inversion of fault populations (Homberg et al., 1997), tectonic stylolites and micro-strains from twinning in sparry calcite. Strain trajectories (maximum shortening direction) computed from these data define a strongly divergent fan with a 90° opening. A complete displacement vector field for the entire Jura has been determined from balanced cross sections augmented with 3-D 'block mosaic' restorations (Philippe et al., 1996). Displacement vectors diverge by about 40°, markedly less than strain trajectories. The non-parallelism between strain trajectories and transport directions indicates that considerable wrenching deformation did occur in both limbs of the Jura arc. Paleomagnetically determined clockwise rotations of 0 to 13° from ten sites (Kempf et al., 1998) behind the right-hand half of the Jura arc and two sites with a combined 23° anticlockwise rotation behind the left-hand half of the arc are and additional argument in favour of such a wrenching deformation. We conclude that the Jura arc formed as a 'Primary arc' with a minor component of 'Piedmont glacier' type divergence in transport directions.

5.2 Introduction

Arcuate mountain belts range in scale from tens of kilometres in thin-skinned foreland fold-thrust belts (Marshak, 1988) up to hundreds of kilometres, where the entire crust or lithosphere is involved (Isacks, 1988). Seen from the foreland side, arcuate folding patterns strongly suggest radial spreading of material (Argand, 1922; Platt et al., 1989a). Considering the concave side of an arc, however, spreading models are faced with severe space problems because the same area in the centre of the arc is claimed as source region to large amounts of material, which supposedly moved in divergent directions. Despite their widespread occurrence along compressional plate boundaries few if any examples exist where the arc forming processes are well documented and understood (Wezel 1986). We simplify and modify existing classification schemes (Marshak, 1988; Ferrill, 1991) and concentrate on three extreme end members in Figure 5.1): A)Oroclinal bending, B)'Piedmont glacier' and C) 'Primary arc'. This conceptual and genetic classification puts the emphasis on the complete displacement vector field and resulting total strain patterns. These key parameters are portrayed in Fig. 1 with the aid of a strain grid and strain ellipses for internal bulk deformations, rotations and structural trends. Although such a classification seems straightforward in principle, geologists are confronted with the inverse problem. Based on the structural grain in a mountain belt as seen in a satellite picture or tectonic map, strain determinations from balanced cross sections, maybe completed with some paleomagnetic data for rotations, we try to reconstruct the total displacement vector field of an arc. With such quite incomplete data-bases, it is questionable if we are ever able to distinguish the subtle differences which exist between the displacement vector fields of up to eight different arc formation modes proposed by Marshak (1988) fig.6. Here we try the less ambitious task to establish criteria for the distinction of only three end-member cases.

Based on a simple model set up of a primary arc, we examine the complex relationships between strain, rotation and displacement in oblique deformation zones. Simple geometric modeling shows indeed that neither fanning strain trajectories, nor rotations about vertical axes, nor arc-parallel extensions are sufficient arguments for a divergence in material flow. The difficulties in distinguishing arc formation modes are discussed for the case of the Jura fold-thrust belt. There are probably few if any other arcs in the world with more strain data, and still, there remains considerable uncertainty about the arc formation mechanisms responsible for the formation of this late alpine arcuate fold-thrust belt.

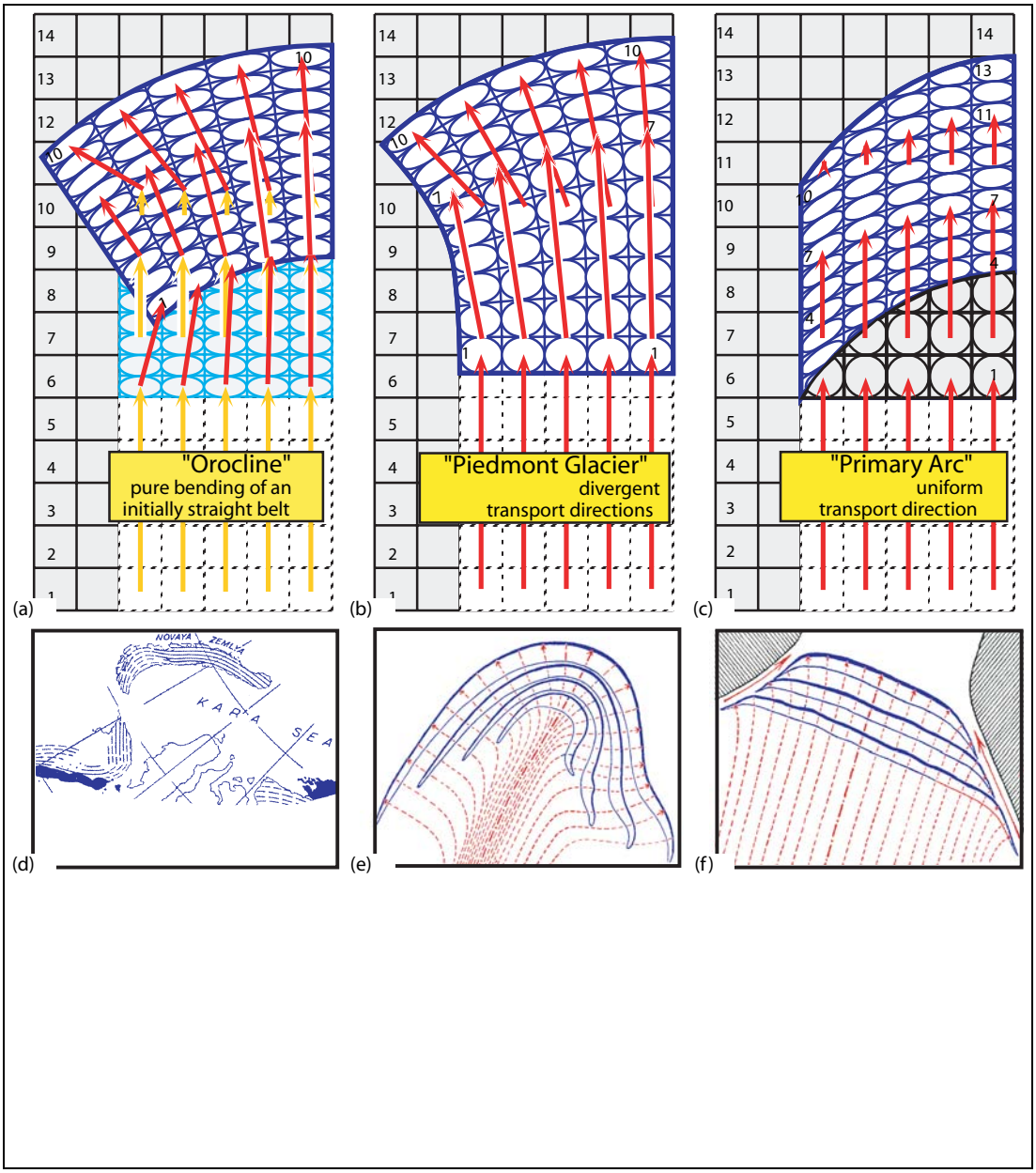

Figure 5.1: Conceptual arc formation models. Strains and rotations in map view are illustrated using an initially square grid and finite strain ellipses (in blue). Undeformed Foreland is shaded in grey, some grid positions are numbered for comparison with the deformed grid within the arcs. Finite displacement vectors in red are superimposed for grid lines 1, 7 and 10. a) Orocline model : according to Carey (1955), an initially straight belt is bent into an arc shape during a second stage of deformation, modeled here as a pure bending. b)'Piedmont glacier' model with strongly divergent displacement directions. c) 'Primary arc' with uniform transport direction. d) The Novaya Zemlya arc formation in two steps according to Carey (1955) (details out of his figures 15 and 16). e) Modified detail out of Argand (1922) schematic figure 2 showing a 'virgation du premier genre'. f) Modified detail out of Argand's (1922) schematic figure 4 showing a 'virgation du deuxième genre'.

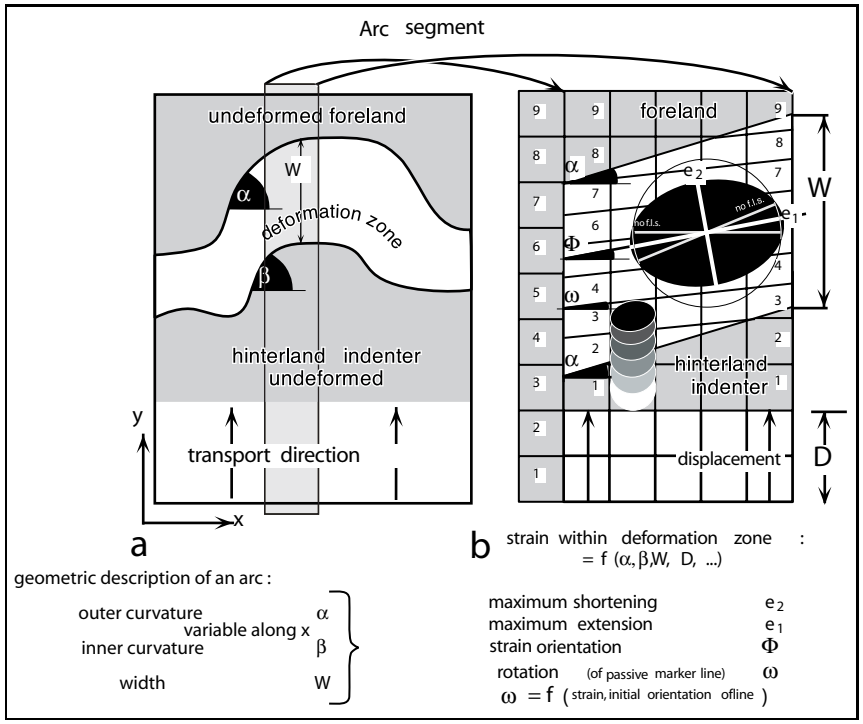

Figure 5.2: Primary arc model with uniform displacement direction. a) Schematic arcuate deformation zone and definitions of some geometric parameters used for the modeling of strains within a segment of this oblique deformation zone. b) Model set-up of a segment of an arcuate deformation zone, used to investigate the relationships between finite strain, displacement and curvature. Letters describing various lengths and angles are used for calculation of strain parameters (Fig. 5.3) and discussion in main text.

5.3 Arc formation Models

In the 'Orocline' according to the concept of Carey (1955) the arcuate shape of a mountain belt is achieved in two steps: an initially straight fold-thrust belt is bent into an arc during a second deformation event e.g. when such a belt is moulded onto an irregularly shaped continental margin or other 'basement' obstacle during final stages of collision. In Fig.5.1a, this sequence of events is sketched by a first pure shear shortening (light blue ellipses) followed by a second event of pure bending. The resulting finite strain pattern is illustrated by superimposed dark blue ellipses. Although Carey (1955) did not elaborate on the possible mechanisms of bending the first straight belt into a curved one, the 'orocline concept' is most often used to infer a pure bending. Such an 'orocline' in the restricted sense is characterised by arc-parallel extension on the outer side and arc-parallel compression on the inner side of the arc. As shown in Fig. 5.1a, strain incompatibilities both in the foreland and the hinterland of the orocline are large. In particular, shortening in a general direction perpendicular to the symmetry axis of the arc would be expected on the inner side. This shortening increases with the rotation of the two limbs of the arc. Passive rotations of these limbs are equal to their angle with the supposedly straight line they formed prior to oroclinal bending. Such rotations around vertical axes are directly quantified with paleomagnetic methods (Eldredge et al., 1985; Isacks, 1988; Lowrie and Hirt, 1986; Tait et al., 1996) and the term 'Oroclinal bending' is most often used in the context of paleomagnetically determined 'rigid block' rotations in an arcuate fold belt. Limb rotation alone is not a sufficient argument for the identification of pure 'Oroclinal bending', however, since substantial rotations also occur from other possible arc formations modes such as differential transport to the foreland (Marshak et al., 1992) figs. 1,2,3 and/or shortening deformation within an oblique zone as will be shown below (Fig. 5.1c, Fig. 5.2). The Bolivian Andes as one of the classic paleomagnetically documented examples of Oroclinal bending has convincingly been reinterpreted by Sheffels (1995) as a 'primary arc'.

The 'Piedmont glacier' model of 'radial thrusting / spreading' (Fig.5.1b) (Merle, 1989), requires a clear separation of an arcuate fold nappe emplaced upon an undeformed foreland. Nappe internal strains are characterised by foreland-ward increasing arc-parallel extensions. Along radially divergent transport- ('flow-') directions, strains may vary from extensional at the rear to compressional at the front. As in the oroclinal bending model, passive

rotations of initially straight marker lines in the arc's limbs are as large as suggested by the curved outline of the 'spreading' arc. Radial thrusting/ spreading is probably the most popular type of arc formation model ever since Argand's "La Tectonic de l'Asie" (1922, p.207ff and fig. 2) where his drawings clearly show such 'virgations du premier genre' to be responsible for almost any arcuate belt in the Alpine - Himalayan chain (op. cit. fig. 9 and 10).

The 'Primary arc' is a fold-thrust belt which adopts an arcuate shape right from the beginning of its formation. Such a curvature in the thrust front of a foreland fold-thrust belt may be induced by a series of boundary conditions. Lateral variations in facies, thickness, layering in the hangingwall and/or irregularities in the footwall/foreland are all potential sources for the generation of curvature in fold-thrust belts (Marshak et al., 1992). A very simple geometric model of an idealised primary arc is shown in Fig. 5.1c. This model set up demonstrates, that an arcuate deformation belt can even be produced in an environment of rigorously uniform displacement direction (Ferrill, 1991). The consumption of the advance of an arcuate indenter within a curved deformation zone, i.e. a primary arc, leads necessarily to divergent, fanning strain trajectories within this deformation zone. The limbs of any arc produced in this way are characterised by transpressional wrenching deformation (Marshak et al., 1992; Sanderson and Marchini, 1984; Sylvester, 1988; Wilkerson et al., 1992). Argand (1924, p. 210 and fig. 4) called this mechanism 'virgation du deuxième genre' and clearly considered it of lesser importance.

The key parameter used in distinction of arc types, namely the displacement vector field, is the most difficult to obtain in nature. This explains why so many different arc classification schemes have been proposed in the past. Critical examination of the three end member models portrayed in Fig. 5.1 shows that it may even be difficult to distinguish between three extreme arc formation models of Fig. 5.1 if only the central, frontal portions of an arc are considered. All models involve rotations of passive marker lines as well as strike-parallel extensions within the limbs of the arc. Large strike-parallel extensions in the frontal parts of the arc are a strong argument in favour of either oroclinal bending or divergent thrusting / spreading. Regarding rotations, however, only the precise angles of rotation in relation with the strike of the arc's limbs, and total strain provide a sufficient criterion to discriminate the 'Primary arc' from the other two models (Eldredge et al., 1985). Ideally, the total strain distribution or at least gradients in extensional strains across and along strike should be known, because this is the only way to determine the displacement directions in various parts of an arc.

5.4 Modeling strains in a 'Primary arc' with uniform transport direction

A simple geometric two-dimensional model has been designed in order to evaluate the relationships between displacement vector fields, arc shape and finite strain axes orientations in variations of a Primary arc model (Fig. 5.2a). In this conceptual model set-up, a two-dimensional sheet is deformed within a rectangular box (Fig. 5.2b). Transport direction is held strictly unidirectional toward the foreland. Deformation takes place within an oblique deformation zone which makes an angle a with the transport direction. This oblique deformation zone can be viewed as a segment of an arcuate fold-thrust belt (Fig. 5.2a). Deformation is imposed within this zone by advancing a rigid hinterland indenter. For simplicity, deformation is assumed to be homogeneously consumed within the entire N-S length of the deformation zone, and without any slip on the limits between foreland, deformation zone and rigid hinterland indenter. North-south oriented marker lines thus remain perfectly straight and do not rotate. In other words, no material is allowed to be squeezed out on the right- or left-hand side of the modeled arc segment shown in Fig. 5.2b. For comparisons with the starting conditions, the left hand side of Fig. 5.2b shows an undeformed row with grid numbers for a rapid identification of corresponding positions in the deformed grid of the arc segment. Given these boundary conditions, finite strain within the modeled deformation zone is homogeneous and can be calculated. Geometrically, finite strain can easily be understood as the superposition of a pure shear deformation followed by a simple shear deformation. The pure shear component is required to shorten any N-S line to its deformed length (W) as imposed by the advance (D) of the indenter. The 'pure shear' shortening in transport direction (ps) is calculated as the length change (D) over the initial length (W+D):

$$ps = D/(W+D)$$

A component of 'transport parallel' simple shear (ss) is required to twist this shortened material into the oblique deformation zone in order to avoid any misfit between the deformed zone, its foreland and the rigid hinterland indenter respectively. The simple shear component is calculated as :

$$ss = ps * \tan(a)$$

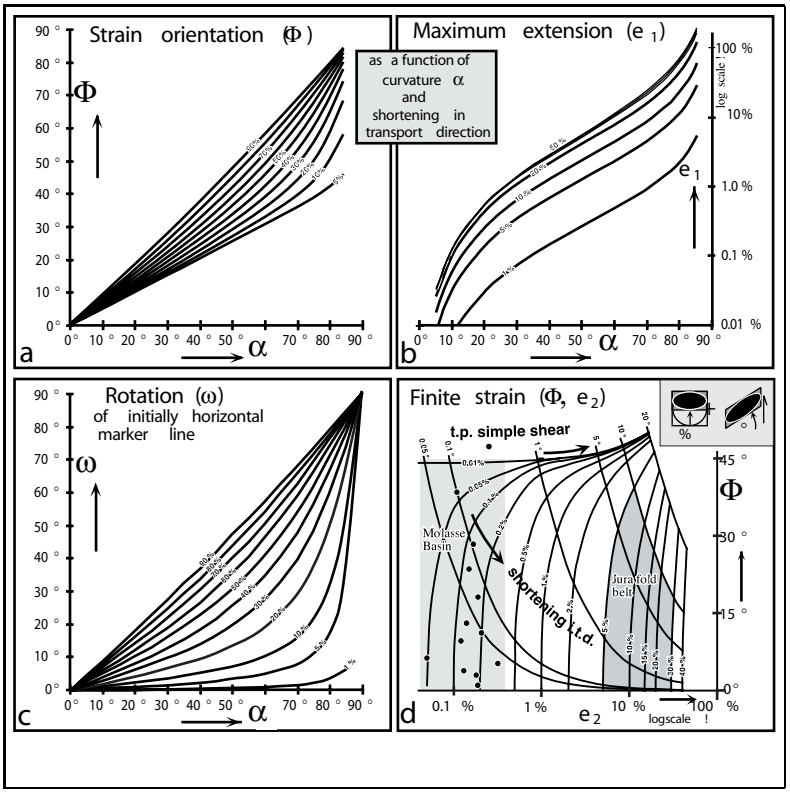

Figure 5.3: Strain parameters resulting from deformation in an oblique arc segment shown in Fig. 5.2b: a) Finite strain orientation (F) with respect to transport direction vs. the obliquity of the deformation zone (a) as a function of variable amounts of 'pure shear' shortening in transport direction (indicated in % along the curves). b) Maximum extension (e1, finite strain) in % on a logarithmic scale vs. the obliquity of the deformation zone (a) as a function of variable amounts of "pure shear" shortening in transport direction (indicated in % along the curves). c) Rotation (w) of an initially transport perpendicular marker line vs. the obliquity of the deformation zone (a) as a function of variable amounts of 'pure shear' shortening in transport direction (indicated in % along the curves). d) The effects of the superposition of variable amounts of "pure shear" in transport direction (expressed as %shortening) followed by transport parallel simple shear (expressed as the angle of simple shear) are illustrated in terms of resulting finite strain orientation (F) and maximum shortening (e2) expressed as % on a logarithmic scale. Calcite twinning strain determinations from the Swiss Molasse basin are reported as black dots within a grey shaded box at the left hand side of the graph, a second box at the right hand side illustrates the estimated strain field for the Jura fold thrust belt (compare fig. 5.4).

Rotations (w) of initially horizontal passive marker lines (perpendicular to the transport direction) result from the simple shear component of deformation and are calculated as:

w = atan (ps*tan(a))

Rotations in general are dependent on the initial orientation of a marker line and decrease to zero for marker lines oriented parallel to the transport direction.

Some of the most striking results of these considerations are shown graphically in Fig. 5.3. The orientation of finite strain axes orientation (F) has been calculated as a function of the amount of shortening in transport direction (ps) and for variable curvatures (a) in Fig. 5.3a. Note that even very weak shortening in transport direction within an oblique deformation zone leads to considerable deviations of the finite strain axes from an 'expected' orientation perpendicular to the imposed transport direction. Maximum horizontal extensions (e1) are calculated as a function of the curvature and shortening in transport direction in Fig. 5.3b. Extensions increase exponentially with curvature and shortening in transport direction. However, Fig. 5.3b clearly illustrates the difficulty associated with the identification of any obliquity between transport direction and finite strains as seen in a fold-thrust belt. Consider an oblique deformation zone with an angle a of 45 ° and a shortening of 30% in

transport direction. The resulting arc parallel stretching of around 5 % only may easily go unnoticed! Passive rotations (w) of an initially horizontal marker line has been calculated as a function of the amount of shortening in transport direction (ps) and for variable curvatures (a) in Fig. 5.3c. This figure shows that passive rotations are a significant component of strain within an oblique deformation zone (Fig. 5.2b); passive rotations are in all cases less than the obliquity of the deformation zone (a) and less than the long axis orientation of the finite strain ellipse produced within this deformation zone (compare Fig. 5.3c with 5.3a).

More general models of oblique deformation zones can be set up by varying the width W along strike, by varying both outer and inner curvature of the belt, i.e. angles a and b in Fig.5.2a, by varying the total imposed displacement D along strike and so on (Hindle, 1997). In all such models, deformation within the deformation zone can be viewed as the superposition of variable amounts of 'pure shear in transport direction' and 'transport parallel simple shear'. The relative importance of these two deformations determines the deviation of the principal finite strain axis orientation (F) from the transport direction. The general case of superimposed transport parallel simple shear on pure shear shortening in transport direction is shown in Fig.5.3d which demonstrates that large deviations of up to and more than 45° between the maximum finite shortening direction (e2) and the transport direction are obtained even in very weakly deformed transpressive zones.

A counterintuitive conclusion of these models is that very weak simple shearing deformations within an arc (and its hinterland) are capable of producing strong deviations between strain axes orientations and transport direction (non-coaxial deformations). Furthermore, the extremely simple model set-up of Fig.5.2b demonstrates that deformations within an oblique deformation zone with parallel foreland and hinterland borders (a = b), will provoke rotations (w) in passive marker lines with progressively increasing advance of the hinterland indenter by the distance D.

Some key points regarding strains within an arc formed by the 'Primary arc' model with uniform displacement direction are summarised as follows. Compressional deformation across the arc is accompanied by longitudinal extension in a direction close, but not parallel to the structural grain of the arc's 'limbs'. The amount of this extension is strongly dependent on the intensity of simple shear deformation and increases non-linearly with increasing angle of the 'limbs' of the arc (a). The direction of maximum extension is oblique to both the overall 'limb' angle and the transport direction (Fig. 5.2b). The fact that an arc-parallel line of 'no finite longitudinal strain' exists in this model has often been misinterpreted in the sense that no longitudinal extensions existed at all (Ries and Shackleton, 1976; Ferrill, 1991). This line, however, is merely one of two symmetric lines of no finite extension within the general strain ellipse produced by transpression (Fig. 5.2b). Rotations are a direct consequence of the simple shear component and increase with the increasing angle of the 'limbs' of the arc and with increasing shortening in transport direction.

Marshak (1988) proposed a modified, loosened definition of Carey's 'orocline', as "a bend in which the strike of segments of the bend does change during and/or subsequent to the formation of the orogen" (op. cit. p. 74). This type of arc is opposed to the 'non-rotational' bend, "in which the strike of segments of the bend does not change during the formation of the orogen" (Marshak, 1988) (p. 74). Such a distinction of arcs is problematic for several reasons : The primary arc model sketched in Fig. 5.2b demonstrates that progressive compressional deformation within an oblique deformation zone necessarily leads to rotations of passive marker lines and to a progressive rotation of the structural grain in the oblique deformation zone. The term 'strike' used by Marshak with regard to rotations during arc formation is not clearly defined and would apply only to the boundaries between rigid hinterland indenter and deformation zone (b) or the limit between the latter and a rigid foreland (a, compare Fig. 5.2a), but the term 'strike' does not apply to the structural grain within the deformation zone itself. We pretend that there is no 2-D or 3-D arc formation model which is capable of producing a bend in a compression belt without involving rotations of some passive marker lines seen in map view of this belt. Nevertheless, a non-rotational arc fitting the above quoted definition of Marshak (1988) does exist : in our classification, it would be a 'Primary arc' with divergent transport directions (as in the 'Piedmont glacier' type). Transport directions would have to be strictly perpendicular to the imposed, pre-existing arc shape ('strike of the arc') - passive marker lines in general would be rotated, but not the 'strike' of the arc. Our own classification scheme of arcs suffers from a similar problem, however. Using the 'displacement vector field' rather than strains, rotations or shape as the main criterion to distinguish different types of arcs, we rely on the one parameter which is the most difficult to obtain in a natural deformation belt. These difficulties and possible ways to resolve them are discussed in the following section where the Jura arc of the external Alps is discussed.

5.5 The Jura Arc

5.5.1 Tectonic overview

The structural grain of the Jura arc in the NW foreland of the Alps swings a full 90 degrees from a N-S direction at the south-west end to an E-W direction at the north-east end (Fig. 5.4). This latest and most external fold-thrust belt of the Alps developed after the Middle Miocene (Serravallian) on the external side of the Molasse foredeep (Laubscher, 1992; Burkhard and Sommaruga, 1998). Mesozoic platform carbonates (up to 2.5 km) as well as an Oligo-Miocene clastic Molasse wedge (0 to 4 km) are involved in folding and thrusting above a major basal décollement within Triassic evaporites (Buxtorf, 1916; Jordan, 1994; Sommaruga, 1996). The palaeogeography of the Triassic 'Muschelkalk' and 'Keuper' series is largely responsible for the arcuate shape of the Jura fold-thrust belt (Debrand-Passard et al., 1984; Philippe, 1994). The external border of the Jura arc coincides with the salt/gypsum pinchout and the arc mimics directly the original shape of the Triassic basin border. The western and eastern limbs of the Jura arc owe their asymmetry to palaeogeography. In addition to lateral variations in the basal décollement level, a lateral increase in total thickness of the folded Mesozoic cover explains a striking westward increase in fold amplitude and wavelength. While the outer curvature of the Jura arc can largely be interpreted in terms of palaeogeographic prestructuration, the inner curvature, i.e. the rather abrupt change between virtually undeformed Molasse basin and strongly folded and thrust Jura still remains a matter of debate. It could be induced by the late Variscan structural grain within the pre-Triassic basement (Philippe, 1995). Reflection seismic surveys across this boundary at the eastern termination of the Jura show some weak normal fault off-sets in the Triassic series above the Permo-Carboniferous grabens and below the basal dcollement (Diebold et al., 1991). Such irregularities within the Triassic basal dcollement horizon are thought to have triggered major thrust fault splays breaking through to the surface across the entire Mesozoic cover sequence (Laubscher, 1986). In terms of critical taper geometry (Chapple, 1978; Dahlen, 1990) the internal border of the Jura arc may simply be regarded as the line behind which the taper angle of the combined thickness of Mesozoic and Neogene sediments was sufficient for thrust translation whereas north of this line, some internal deformation, thickening and increase of topographic slope was a requirement for further thrust propagation to the NW. The Jura fold-thrust belt is located above the present day flexural bulge region in the alpine foreland (Karner and Watts, 1983; Burkhard and Sommaruga, 1998), an area where the cover thickness is at a minimum. A large amount of strain data has been collected over the last decades within the curved Jura fold-thrust belt. Different categories of strain measurements can be distinguished; they are discussed below.

5.5.2 Strain measurements and their relevance to Arc formation

2-D cross section balancing: The best large scale strain estimates are provided by balanced cross-sections, available at various degrees of sophistication for all parts of the Jura. Bulk shortening perpendicular to the fold trends ranges from more than 35 km (in W-E direction) in western parts to some 25 km (in NW-SE direction) in central parts (Mugnier et al., 1990; Philippe, 1995). Towards the east, bulk shortening decreases regularly to zero (Laubscher, 1965; Bitterli, 1988; Burkhard, 1990). Despite their accuracy, estimated at better than 20%, cross section balancing results are incomplete measures of strain, however. Transport directions are an input - assumed to be known - and not an output of cross section balancing techniques. The postulate of no material moving in or out of section sideways obviously limits their applicability within oblique deformation zones of wrench folding. In terms of arc formation models and attempts at their discrimination, three dimensional strains or at least estimates of the arc parallel extensions are required in addition to the shortenings obtained from 2-D section balancing.

Strain trajectories: The Jura fold-thrust belt was deformed under very little cover, mostly less than 1 km, at temperatures well below 100°C. Accordingly, outcrop and handspecimen scale deformation features are limited to joints, veins, faults and tectonic stylolites. Cleavage development is restricted to the proximity of larger faults and shear zones within marl and shale horizons. The systematic mapping of meso-scale strain-axes orientations includes tectonic 'horizontal' stylolite peaks (Plessmann, 1972) interpreted as indicators of the local maximum horizontal shortening direction. Small scale striated faults with displacements on the order of a few mm to dm are a widespread phenomenon, seen in virtually any fresh outcrop of limestones be it folded or subtabular. Most minor fault surfaces in Jura limestones carry slickenfibers, slickolites or some asymmetric wear-features on slickensides which enable an easy identification of both displacement direction and shear sense. The systematic measurement of many small scale faults and their inversion at any given site permits the determination of palaeo-stress (or strain-) axes directions (Angelier, 1994). The most complete palaeo-stress data set to date has been

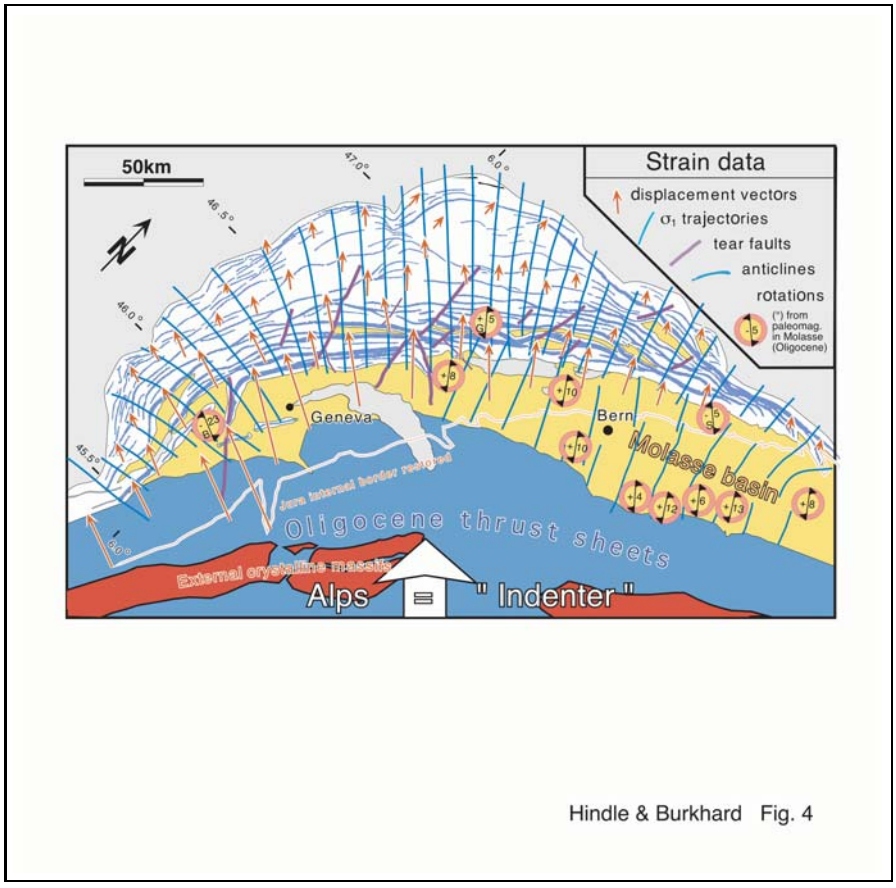

Figure 5.4: Tectonic overview of the Jura arc in front of the northwestern Alps with compiled strain data. The arcuate shape of the Jura is materialised by the trend of major anticlines (Heim, 1921). Strain trajectories (in blue) have been computed from a large data set of 180 stations where populations of minor faults have been used to calculate paleo-stress tensors by inversion methods (Homberg, 1996). Strain trajectories within the Molasse basin are based on striated and indented pebbles (Schrader, 1988) and twinned calcite cements (Hindle, 1997). Displacement vectors (red, to scale) are based on balanced cross sections augmented by 'block mosaic' restorations in map view (Philippe et al., 1996). A thin red line marks the approximate restored position of the inner boundary of the Jura arc. Rotations have been paleomagnetically determined by Kempf et al. (1998) with three additional sites from Gehring et al. (1991), Burbank et al. (1992) and Schlunegger et al. (1996), marked G, B and S respectively. Oligocene data have been corrected systematically by -10° according to a paleo-pole from Besse and Courtillot (1991)

acquired by Homberg (1996). This data set includes 180 sites, often with up to four successive deformation phases distinguished. The latest and most important Mio-Pliocene folding phase data have been used to construct a strain trajectory-map (Fig. 5.4, blue lines) according to an interpolation- and smoothing- procedure which considers the spatial distribution of sites as well as the data quality at each site (P.Dick 1998, unpublished; using software provided by Lee and Angelier (1994)). The deformation style in the Jura alternates between a dominant thrusting regime with a subordinate strike-slip component. The former is expressed in conjugate small scale thrust faults and bedding parallel slip planes associated with folds while the latter is materialised in form of conjugate sets of strike slip faults at a high angle to bedding. Both thrusts and strike slip faults were active simultaneously and no relative chronology can be established between the two regimes (Laubscher, 1972; Tschanz and Sommaruga, 1993; Homberg et al., 1997).

Micro- scale strain-determinations from twinning in calcite (Tschanz, 1990) reveal shortening directions which are mostly at high angles to the map scale fold axes; local obliquities have been interpreted in terms of wrench folding (Tschanz and Sommaruga, 1993). These techniques have also been used to reconstruct the alpine palaeo-stress field in front of the Jura fold thrust belt (Bergerat, 1987; Lacombe et al., 1993). In order to complete the regional scale strain data set we determined micro-strains within the flat-lying layers of the Molasse basin adjacent to and behind the Jura arc. Microscopic investigation of a competent member of lower Miocene marine Molasse sandstones revealed the ubiquitous presence of deformation twinning in calcite cements and bioclasts. Calcite grains larger than about 10 mm are frequently twinned and permit the determination of strain orientations and magnitudes. We used the Groshong (1972) technique to determine strains within the apparently undeformed Molasse rocks (Hindle, 1997). Our study fills an important gap in the central, hinterland portion of the Jura arc. Twin strain data indicate minute strains, between 0.01 and 1 % shortening and extension respectively. The strain regime varies between thrust and strike slip. Detailed data tables are found on the internet at http://www-geol.unine.ch/Structural/DHdata.html.

At the southern border of the Molasse-Basin, conglomerates show macroscopic evidence for horizontal tectonic compression in the form of striations, slickolites and stylolites on 'pitted' carbonate pebbles (Schrader, 1988). A regional scale survey of these features has enabled Schrader (1988) to construct a strain trajectory map for the southern rim of the Molasse basin (included in our Fig. 5.4). Based on the symmetry of strain features on conglomerates, Schrader was also able to characterise the form of the strain ellipsoid, which varies between oblate (pure compression) and plane strain, often in a strike slip regime.

The strain trajectory map shown in Fig. 5.4 describes a strongly divergent, radial pattern with NE to N directed compression at the eastern end of the Jura and W directed compression behind the western termination of the arc. This gross pattern confirms the large scale structural trend of the Jura fold-thrust belt as depicted by a tectonic map (Heim 1921, tafel XX). Local irregularities in the strain trajectory map and detailed relationships between tear faults, faults and 'back-ground strain' axes directions are discussed by Homberg et al. (1997) in terms of stress-deviations in the vicinity of major tear faults. So far, however, no attempts at integrating the strain-trajectories into balancing considerations, be it 2-D or 3-D have been made in the case of the Jura arc.

3-D restorations $\Longrightarrow$ Displacement vector field : 3-D balancing work in the Jura was pioneered by Laubscher (1961, 1965) who developed what he called the 'block mosaic' restoration technique. The Basel school applied it to eastern parts of the Jura fold-thrust belt in ever increasing detail (e.g. Bitterli (1988)). In essence, the 'block-mosaic' technique is based on series of balanced 2-D sections, made mutually compatible with each other by trial and error. Restored bedding surfaces or '3-D blocks' are obtained by filling spaces in-between balanced sections. In this technique neither the true surface of marker horizons nor their capacity to 'unfold' without bed internal stretching (Lisle, 1992) is verified, however. Similarly, in the 'pseudo-three-dimensional approach' of Wilkerson et al. (1991) (fig. 1) oblique folds are produced and balanced without any consideration of true 3-D bed-internal stretches required to allow for the differential displacements in the first place. Gratier and Guiller (1993) have developed a more objective 'UNFOLD' - method of smoothing out entire contour maps of folded marker beds. Folds in this technique are still treated as 'folds in a sheet of paper', however, i.e. no stretches are allowed within the sheet itself. With this premise, folds are always restored in a direction perpendicular to their fold axis. Smooth folds in a 'sheet of paper' cannot form in a direction oblique to transport direction (e.g. in a model such as shown in Fig. 5.2b). Wrench folds require the development of tear faults or some other kind of intrabed strain. Both Laubscher's and Gratier's approaches at 3-D restoration stand and fall with the quality of the initially drawn cross-sections and contour-maps. Applied to faulted and thrust series, the most important uncertainties do not reside with the smoothing out of individual folds, however, but with ill defined fault off-sets between different folds and along tear faults, and of course from unknown intrabed stretches. When

it comes to reassemble unfolded, (restored) blocks in a possible prefolding configuration, Laubscher's and Gratier's approaches are identical and meet with the same difficulties. Thrust fault off-sets are constrained from section balancing whereas no direct way exists to determine off-sets along tear-faults. In assembling unfolded pieces of a flattened structure contour map, gaps and overlaps indicate the quality of the 'block-mosaic' restoration. Reducing these incompatibilities is a very time consuming trial and error process which may include reassessment of initially drawn contour maps - and possibly the search for previously undiscovered tear faults. Automated procedures to minimise such incompatibilities have been proposed by Cobbold (1979) but rarely applied in regional studies (Gratier et al., 1989). The comparison between a completely restored and reassembled 'block mosaic' and the present day deformed state (structure contour map) permits the determination of a displacement vector field as well as the calculation of inferred regional strains in plan form.

Large scale tear faults affect the Jura arc at regular intervals of some tens of kms. N-S trending sinistral faults are more important than conjugate dextral ones (major tear faults are shown in purple in Fig. 5.4). Some of the N-S trending faults inherited their orientation from Oligocene faults formed during development of the Rhine - Bresse graben system (Illies, 1974), while others were demonstrably formed only during Late Miocene Jura folding and thrusting (Homberg et al., 1997). Tear faults clearly accommodate some arc-parallel extension (Heim 1915) which is difficult to quantify, however, because of the lack of suitable passive markers. Folds clearly developed independently on either side of tear faults, simultaneously with tearing, and cannot be used as markers. Block mosaic restorations, backward from the undeformed foreland into the increasingly deformed hinterland, is the only way to determine the map scale strains associated with these faults in particular and the entire displacement vector field on the scale of the arc in general. Our own restorations in the central Jura (**?**) as well as those of Philippe (1995) in the western Jura, indicate that fold axes parallel extensions do not exceed a few percent.

The most complete 3-D block-mosaic restoration of the entire Jura so far has been constructed by Philippe et al. (1996). The displacement vector field derived from this restoration is shown in Fig. 5.4 (red arrows, drawn to scale). Despite some divergence in this displacement vector field, there exists a marked difference between displacement vectors and the significantly more divergent strain trajectories (in blue). Discrepancies are largest in the western limb of the Jura arc (30° and more). Not surprisingly, coaxial deformations prevail in the central portion of the Jura and discrepancies increase again eastward. Due to small total displacements at the right hand side of the arc, however, discrepancies are not so obvious. Given the limitations in the 3-D block mosaic restoration procedure discussed above, the true displacement vector field for the Jura arc can be expected to be less divergent than shown in Fig. 5.4. In the restoration used by Philippe et al. (1996) only the largest tear faults (purple in Fig. 5.4) have been included as free boundaries in the re-assemblage of internally non-stretched flattened blocks. Intrabed wrenching deformations does occur within those blocks, however, as testified by meso-scale fault analyses which show often a component of strike slip deformation regime (Homberg et al., 1997).

Rotations about vertical axes : Based on map scale restorations, Laubscher (1961) proposed a rotation model to account for the westward increase of shortening seen in Jura fold-thrust belt, estimated at some 8° clockwise for the Molasse basin behind the eastern part of the Jura (compare the thin red line behind the internal Jura in Fig. 5.4). Similarly, the strong westward decreasing lengths of sub-parallel displacement vectors behind in the western limb of the Jura arc (Fig. 5.4; data from Philippe et al. (1996)) implies a substantial anticlockwise rotation of material in a sinistral wrenching regime. These expected rotations are still small, however, in comparison with the strong curvature of the limbs of the arc which swing a full 90° angle. Given the lack of suitable passive marker lines, rotations about vertical axes are notoriously difficult to measure directly. Some constraints on rotations are provided by paleomagnetic data. While older studies in Middle Jurassic iron oolites of the Jura fold belt (Eldredge et al., 1985; Gehring et al., 1991) detected only very small and barely significant rotations of less than 10° clockwise, two recent studies in Oligo-Miocene Molasse sandstones from the hinterland of the Jura have identified small but systematic clockwise deviations of paleo-poles from present day geographic north, on the order of 5 to 25° (Schlunegger et al., 1996; Kempf et al., 1998). There are only two published sites from behind the western half of the Jura (Burbank et al., 1992). The combined result of the Findreuse and Fornant sections shows a small anticlockwise rotation of ca. 13° from the present day geographic north (although this deviation was not considered as significant by the authors). The tectonic interpretation of the paleomagnetically determined declinations for Oligocene Molasse sandstones is somewhat hampered by the fact that there are no directly comparable sites available for the undeformed foreland of the Jura. The maximum difference between paleo-pole declinations east and west of the symmetry axis of the Jura arc is on the order of 30 to 35° for rocks of the same Oligocene age. According to Besse and Courtillot (1991), the European paleo-pole position for Oligo-Miocene times was located some 10° to the 'east' of the present day geographic pole. Accordingly, tectonic

rotations shown in Fig. 5.4 have been systematically corrected by -10° with respect to the published declinations (see also discussion in Kempf et al. (1998).

A fundamental question in rotation studies regards the strain partitioning and deformation mechanisms leading to the rotation of 'passive' marker lines. Perfectly homogeneous deformation within an oblique deformation zone, such as modeled in Fig. 5.2 can be opposed to perfectly rigid blocks, rotated in-between discrete faults. In the latter case, block rotations are strongly dependent on the organisation and hierarchy of faults in a fault network. Analogue experiments of dextral simple shear (Schreurs, 1994) provide some interesting insights into the relationships between distributed background strain and localised faults. In the simple shear model of Schreurs' (1994, Fig.2a and b), distributed 'homogeneous' deformation is dominant in early stages (γ up to 0.17) leading to rotations of transport perpendicular marker lines up to 10°. Transport parallel lines have not rotated at all. In later stages ($\gamma = 0.17$ to 0.39), rotations increase locally to about 30° clockwise between synthetic 'cross faults', more than the overall total 21° rotation imposed by dextral simple shear! However, transport parallel marker lines have significantly less rotated, indicating that internal 'distributed' strains are an important component. The question arises if and how paleomagnetically determined paleo-pole directions are affected by weak internal deformations. Assuming that such internal deformations up to 10 to 20% stretching/shortening are not sufficient to have any effect on the minute magnetic particles and their distribution in a rock, the paleomagnetic method provides a very powerful tool to determine 'rigid block' rotations. The size of such rotated 'blocks' is certainly larger than the rock sample, but probably smaller than the average mapped distance between major faults in an area. Large scale tectonic interpretations are limited by our sketchy knowledge about the organisation of intermediate size faults, fault networks and their rotation effects on 'blocks' in-between them.

Significant improvements of 3-D balancing could probably be obtained by the integration of micro- and mesoscale observations into large scale 3-D restorations. Fault patterns observed in the outcrop have been used so far only for the construction of paleo-stress directions; the same data sets, augmented with displacement - lengths - frequency observations could provide very useful estimates of fault-related strain magnitudes (Scholz and Cowie, 1990; Cowie and Scholz, 1992). Similarly, paleomagnetically determined 'block' rotations provide and additional constraint on fault related intra-bed strains on a larger scale.

5.6 Conclusions

(1) A straight forward genetic classification scheme of arcs into three end member models is proposed. Key parameters are the displacement vector fields and the resulting finite strain patterns. The identification of mechanisms which lead to the formation of arcuate mountain belts relies on the recognition and mapping of subtle large scale strain components such as bulk arc-parallel extensions and rotations about vertical axes. Neither of these quantities are obtained from the routinely applied 2-D balancing of cross sections, which require an a priori knowledge of transport direction.

(2) The intuitive interpretation of arcuate fold belts as 'virgations du premier genre' (Argand, 1922), with fanning transport directions as seen in 'Piedmont glaciers' should not be accepted in the absence of positive arguments such as large arc-parallel extensions in the outer, frontal portions of the arc. Rotations and arc-parallel extensions in the limbs of arcs, generally used as arguments in favour of either 'oroclinal bending' or 'divergent spreading' do also result from the superposition of variable amounts of pure and simple shear in transport direction even in a strictly parallel displacement vector field of 'Primary arcs'.

(3) Strain determinations on all scales are available for the late Miocene Jura arc which shows a marked 90° change in structural grain as well as a radial pattern in mesoscopic strain trajectories. Deformation type varies between pure shear compression (thrusts and folds) and strike slip faults on all scales. Strain trajectories show a strongly fanning pattern with a 90° divergence (Homberg, 1996).

(4) 3-D restorations of the Jura arc (Philippe et al., 1996) are based on section balancing data, augmented with 'block mosaic' restorations. The resulting displacement vectors diverge by about 40°, markedly less than strain trajectories. Non-coaxiality between displacement vectors and strain axes indicates significant wrenching deformations in both limbs of the Jura arc.

(5) Bulk arc-parallel stretches are difficult to determine; estimates based on 3-D restorations reveal only minor amounts of less than 10%. Integration of small scale strain features such as 'distributed' tear faults in 3-D restora-

tions would probably increase arc parallel stretches and at the same time decrease divergence in the displacement vector field.

(6) Rotations about vertical axes are predicted by 3-D restorations and constrained by some paleomagnetic measurement sites. Rotations in the Jura arc and its hinterland are barely detectable and range from 0 to 25°, much less than the 90° change in strike around the arc. This discrepancy is a strong argument against pure 'oroclinal bending' and 'piedmont glacier' type spreading. The small observed rotations are best explained by passive rotations in a wrenching regime. The size of individual 'rigid' rotated blocks remains undetermined.

(7) We conclude that the Jura formed as a 'Primary arc' with a dominant NW ward displacement direction and some spreading of material sideways, i.e. a component of 'Piedmont glacier' type. Transport parallel simple shear combined with variably consumed pure shear in transport direction provides the most satisfying explanation to the strains observed in and around the Jura arc at all scales.

(8) Arc formation studies will greatly benefit from future developments of true 3-D balancing techniques and the integration of micro- and meso-scale strain determinations into regional scale 3-D restorations. This is the only way to obtain the single most important item in arc classification schemes : the total displacement vector field.

Acknowledgements

This study was supported by the Swiss National Science Foundation Grants No. 20-43055.95 and 20-50535.97; it represents part of the PhD thesis of D.H. We should like to express thanks to Ph. J. Keane at the Science and Technology Library, University of Tasmania, for promptly sending us a copy of Carey's paper; F. Schlunegger, O. Kempf and P. Strunck for preprints of papers with paleomagnetic data; Y. Philippe and C. Homberg for unpublished ms. of their theses. Discussions with A. Becker, O. Besson, P. Dick (thanks for producing the strain trajectory map), D. Ferrill, J.P. Gratier, R. Groshong, C. Homberg, G. Schönborn have helped to shape our ideas about arc formation. S. Marshak and J.P Evans are thanked for helpful reviews.

Chapter 6

Paleostress estimation from the Molasse indenter

6.1 Introduction

Whilst stresses are a fundamental part of any model of the earth's crust, to quote a famous structural geologist, '..you can't see them'. There has been a tendency to emphasise on the measure of finite strain alone in field geology and the question of stress levels in the crust has received less attention. Yet any notion of the strength of the lithosphere depends on determining the peak differential stresses that the crust supports. High differential stresses drive earthquakes and the stress magnitudes around major, active faults are of great interest. Very complicated interactions between fluid at high pressures and rock under tectonic loading govern fluid movements in the crust. Predicting such behaviour requires a detailed knowledge of stresses in the lithosphere. Still, it remains very difficult to determine reliably the differential stress levels in the lithosphere, for both the past and the present day. A variety of palaeopiezometric techniques have in part grown out of a need to ascertain the reliability of present day measures. These techniques themselves need evaluation and this is best achieved by comparison to rock strength limits.

Studies of past differential stresses, both regional and associated with movement on faults and shear zones have been carried out over the past two decades (House and Gray, 1982; Lacombe et al., 1990; Rowe and Rutter, 1990; Tourneret and Laurent, 1990; De-Bresser, 1991; Lacombe and Laurent, 1992; Newman, 1994). Present day differential stress magnitudes, especially those associated with faulting, have also generated considerable recent attention e.g.((McGarr and Gay, 1978; McGarr, 1980; Zoback et al., 1980; Becker et al., 1987; Bai et al., 1992; Becker and Werner, 1995).

In analysis of past differential stresses, we rely on palaeopiezometric techniques usually based on theoretical relationships between intracrystalline deformation mechanisms of minerals and applied differential stress. Verification of relationships is only possible directly in laboratory studies, hence on limited ranges of samples, and often only over a limited range of pressure, temperature and strain.

In particular, twinning in minerals has been proposed as a robust palaeopiezometer (Tullis, 1980), because of its apparent independence of temperature (to a certain limit), strain rate, and confining pressure (Turner et al., 1954; Klassen-Neklyudova, 1964; Tullis, 1980). Tullis (1980) proposed that lower limits to differential stresses could be placed on a region according to the presence of twins in any type of calcite, dolomite and clinopyroxene, with differential stress minima increasing from 20 MPa for calcite twinning to 200 MPa for dolomite and 280 MPa for clinopyroxene. These values are based on the assumption of a unique and determinable critical resolved shear stresses across twin planes necessary to initiate twinning (Turner et al., 1954; Higgs and Handin, 1959; Klassen-Neklyudova, 1964; De-Bresser, 1991). A further assumption is that the average stress in an aggregate containing such twins must be as large or larger than the critically resolved shear stress of the twinned mineral. Orientation statistics of these minerals are used to derive more precise conclusions regarding stress orientations and/or stress magnitudes.

Two prominent methods for stress determination from calcite twinning have been proposed (Jamison and Spang, 1976; Rowe and Rutter, 1990). Both give numerical values to stress differences supported by aggregates containing calcite or dolomite as a function of the percentage of grains twinned. If the theory on which they are based is sound at a range of temperatures and for a range of aggregates, both should yield corresponding differential stress values for the same data set. However, De-Bresser (1991) and Newman (1994) and new data in this study show this not to be the case. Palaeostresses appear to be dependent on the palaeopiezometer employed. In failing a cross-check both methods' results are placed in doubt. Whilst we cannot necessarily favour one method over the other, consideration of the geological conditions can guide us. Burkhard (1993) pointed out that Jamison

and Spang's method is best applied to low temperature (<200°C) deformations with low strains, whilst Rowe and Rutter's approach is best applied to the range of temperatures and pressures and strain rates over which it was defined (namely 200°C-400°C, and moderate strains). Above these temperatures, dislocation density and recrystallized grain size techniques e.g. (Twiss, 1977) can be used.

However, even if we know which piezometer to apply, we still rely on an extrapolation of the laboratory results to a natural example when we work in the field. What other constraints might we apply to test palaeopiezometers?

Present day stress measures in the crust provide one control. Theoretical differential stress gradients have been established for a variety of rock types (McGarr, 1988), and can be compared to palaeopiezometer readings. The strength of the crust and earth materials provides an additional constraint. Previously fractured rock strength under frictional sliding investigated by Byerlee (1978) has been used to draw a simple strength profile for the crust (Brace and Kohlstedt, 1980). This can be used as an upper limit to differential stresses from palaeopiezometry. Brittle failure by a Coulomb or Mohr criterion also affects sound, unfractured rocks, and direct laboratory comparison of the failure envelope for a rock sample to an appropriately placed Mohr circle of diameter equal to the differential stress determined from palaeopiezometry is another test of confidence in results (Rowe and Rutter, 1990; De-Bresser, 1991).

With new data from the alpine foreland basin, we compare the Jamison and Spang's and Rowe and Rutter's palaeopiezometers. A large number of studies using the same techniques are compared to our results, and all results are compared quantitatively to theoretical strength profiles for the earth and semi-quantitatively to present day stress data. Additionally, the Coulomb failure criterion is considered for the alpine foreland data. At the same time, the questions of sources of differential stresses in the lithosphere are examined. It has been suggested that stresses can be split into plate-wide, regional and local fields, with super imposition of all three (Zoback, 1992; Engelder, 1993). It is already interesting to speculate which type of stress played the most important role in the alpine foreland basin whilst the Jura mountains were being formed.

6.2 Stress Measurement techniques

6.2.1 Present day, in situ techniques

Present day stresses in the crust have been determined with varying degrees of precision over a large depth range (we consider data down to 5km) by a variety of techniques (Engelder, 1993). One class of measurements, stress relief methods, involves freeing a part of a borehole core from lateral constraint and then measuring the associated elastic deformation. Various elastic relationships lead back to the original stress that the rock was subjected to. The Hydrofrac technique provides an alternative means of determining stresses directly in boreholes. Fluid is pumped into a sealed section of borehole until the first instance of fracture in the borehole walls is detected (breakdown) when there will be a pressure drop. If the hydraulic circuit is closed instantly, and the pump shut down, a pressure just sufficient to hold the fractures open is recorded (instantaneous shut in pressure - ISIP). These borehole methods are summarised in McGarr and Gay (1978) and Engelder (1993). Finally, stress determination methods related to stress drops and seismic moments associated with earthquakes can also be used (McGarr and Gay, 1978).

6.2.2 Palaeopiezometric techniques

Palaeopiezometric techniques using twinning, dislocation density, subgrain sizes and recrystallization grain sizes have all been used in the past. The latter three techniques rely on the proportionality between steady state flow stress during hot creep and dislocation density, since nucleation rates increase with higher stresses (Twiss, 1977, 1986). They are reserved for higher temperature regimes. Twinning techniques span quite a range of studies. They are generally focused on two minerals, calcite and dolomite, but clinopyroxene, quartz and feldspars have all been considered candidates for study (Tullis, 1980). Amongst calcite and dolomite twinning techniques, Friedman and Heard (1974) found an increase in the number of twin lamellae in calcite in low porosity limestones due to increased loading and duration of loading. The technique gave an increase in a lamellae index of 10 per 3.5 MPa per up to 40 MPa. Jamison and Spang (1976) proposed a more complete method related to the theoretical magnitude of resolved shear stresses on twin planes in a population of randomly oriented calcite (or dolomite) crystals. The relationship they used is purely theoretical, and was tested by laboratory study and against field examples.

Rowe and Rutter (1990) calibrated several twinning parameters with grain size, and stress levels. They considered twinning incidence (% of grains containing twins in a particular grain size class), twinning index (no.

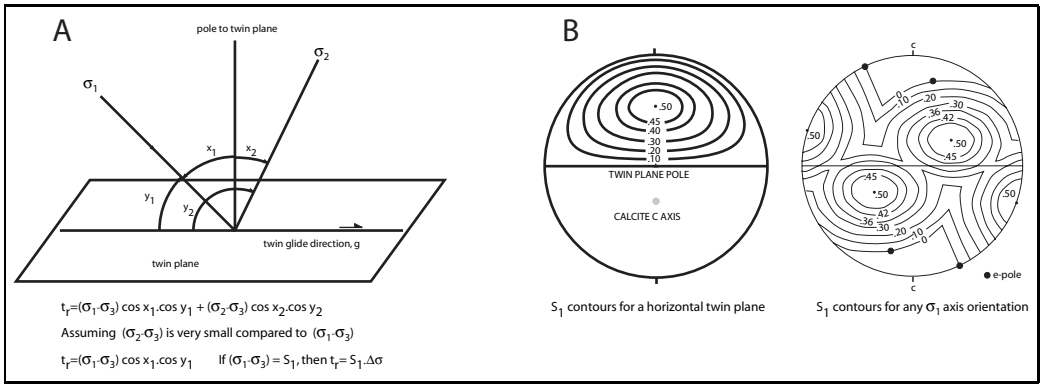

Figure 6.1: a) the resolved shear stress on a twin plane should be at a maximum when the compression axis is at 45° to the plane and in the great circle containing the pole to e, c and g. b) contoured S_1 values for a horizontal twin plane and for randomly oriented σ_1 axes

of twin lamellae per mm. as Friedman and Heard), and volume % twinning. Their empirical relationships between differential stress and grain size were derived for high temperature experiments (=400°C), under steady state flow conditions.

A group of inversion techniques also exist using calcite twin data to reconstruct a reduced stress tensor (e.g.. Tourneret and Laurent (1990); Lacombe and Laurent (1992)).

Regional studies of palaeostress magnitudes using the above techniques are numerous (Friedman and Heard, 1974; Jamison and Spang, 1976; House and Gray, 1982; Lacombe et al., 1990; Rowe and Rutter, 1990; Tourneret and Laurent, 1990; De-Bresser, 1991; Lacombe and Laurent, 1992; Newman, 1994). Their results are interesting in comparison to both present day data and to the results of this study.

6.2.3 Rowe and Rutter's technique

Rowe and Rutters' 1990 method relies on experimental calibration of different calcite twinning parameters associated with a known differential stress. They found that strain rate, temperature and total strain influence the twinning parameters they defined, but that they were affected by grain size and differential stress levels (Schmid et al., 1977; Spiers, 1982; Spiers and Rutter, 1984). We consider only the twinning incidence palaeopiezometer here.

Twinning incidence (I_t) is the measure of the percentage of grains from a particular grain size interval which show evidence of twinning (either single or multiple twinsets). The equation derived from linear regression gives the following relationship:

$$\sigma_D = 523 + 2.13\,\mathrm{I}_t - 204 \log d, \tag{6.1}$$

where d = the representative diameter of each grain measured. Notably, the experiments performed to derive this relationship were all carried out at temperatures =400°C, and involving large strains (7-30%).

6.2.4 Jamison and Spang's technique

The resolved shear stress (t_r) on a twin plane in the glide direction of the twin plane is directly related to the differential stress (σ_D) applied and the orientation of the σ_1 axis relative to the twin plane pole and its glide direction (figure 6.1). Jamison and Spang assumed a uniaxial stress to be applied. Thus, the resolved shear stress for any c-axis orientation relative to the σ_1 axis is

$$t_r = (\sigma_1 - \sigma_3).\cos(x1).\cos(y1) + (\sigma_2 - \sigma_3).\cos(x2).\cos(y2) \tag{6.2}$$

but, because of the uniaxial stress assumption $(\sigma_2 - \sigma_3)$ is considered insignificant compared to $(\sigma_1 - \sigma_3)$, and the equation simplifies to

$$t_r = (\sigma_1 - \sigma_3).\cos(x1).\cos(y1) \tag{6.3}$$

or

$$t_r = S_1.\sigma_D \tag{6.4}$$

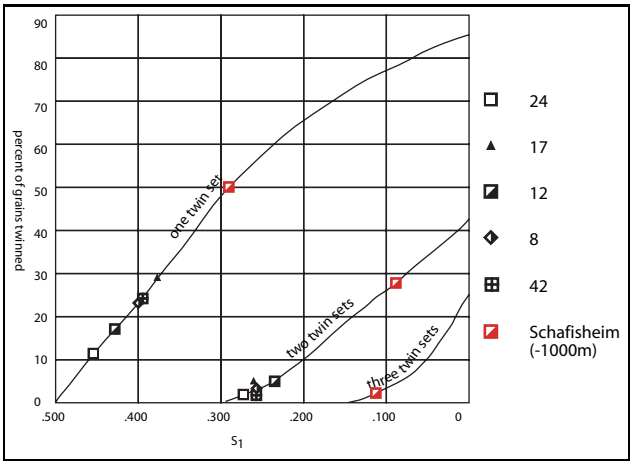

Figure 6.2: The values of S1 according to the percentages of grains showing 1, 2 or 3 twinsets. S1 is calculated for all Molasse samples from this study based on 1, and 2 twinsets per grain, which usually gives different results. This gives a range of possible differential stresses.

where

$$\sigma_D = (\sigma_1 - \sigma_3) \text{ and } S_1 = \cos(x1).\cos(y1) \tag{6.5}$$

This value S_1 is sometimes called the Schmid factor. Assuming a constant σ_1 orientation, and a random orientation of calcite c-axes, the S_1 values will vary for different calcite crystals. We assume that twinning will only occur where the resolved shear stress, t_r = the critical shear stress, t_c for calcite. This is a known constant, usually taken as 10 MPa (Tullis, 1980).

$$t_r = t_c \tag{6.6}$$

For the minimum S_1 value at which twinning is possible,

$$t_c = t_r \tag{6.7}$$

so,

$$\sigma_D = \frac{t_c}{S_1} \tag{6.8}$$

Figure 6.1 shows the S_1 values for a horizontal twin plane and three twin planes (shown as poles. The percentage of the surface of the hemisphere lying within a particular contour is equivalent to the percentage of crystals twinned with S_1 = this value, assuming a continuous and random distribution of c-axis orientations in a sample. There are three twin planes per crystal, and the contours for each twin plane overlap. The percentages of crystals containing 1, 2 or 3 active twinsets in a sample can be found for a particular S_1. The values should be identical for the same sample. Figure 6.2 shows a graph of the values of S_1 associated with a particular percentage of twinned grains in a sample.

This simple theory was also extended to dolomite twinning. For both calcite and dolomite, it is assumed that there is no preferred crystallographic orientation, and that strains are small and coaxial. The technique was tested by laboratory deformation of Indiana limestone at room temperature, 100 MPa confining pressure and 10^{-4}s-1 strain rate with strains up to 8.5%, with a marked deterioration in results as strains increased (Jamison and Spang, 1976).

6.3 Problems associated with palaeopiezometers

6.3.1 Assumptions and Experimental Conditions

Jamison and Spang's technique is underpinned by the assumption of a unique, critical resolved shear stress for twinning and the assumption of no preferred crystallographic orientation of grains. Testing was carried out only at room temperature and at relatively high strain rates. Noticeably, Jamison and Spang's technique fails to account

for grain size, which is known to affect twinning (Spiers and Rutter, 1984; Rowe and Rutter, 1990; Burkhard, 1993; Newman, 1994). Rowe and Rutter's method is based on experimental calibration of one of three twinning parameters described with differential stress and grain size, but only under hot creep regimes (=400°C). Under such high temperature conditions, other deformation mechanisms will compete with twinning, including other slip systems in calcite (r and f glide). It may be true that twinning itself is not a thermally activated process, but nucleation of twins requires a high (unknown) initial shear stress on a twin plane. Once yield by other slip mechanisms can take place, it may be that stresses never reach sufficiently high levels to allow twinning, which appears to be the case from observation of high temperature deformations where twinning is less common (Tullis, 1980). So, once outside such deformation regime, the applicability of piezometric calibrations is questionable. Similarly, Jamison and Spang's technique runs into problems for large deformations when for instance twinning on one set is ubiquitous, and the one twinset values 'fall off' the graph, meaning S_1 has reached 0 and differential stress is 'infinite'.

6.3.2 Grain Size Dependency

Newman's (1994) study of the two piezometers analysed grain size effects. She used samples at varying distances from a fault to try and find systematic variations of stress with distance away from the fault plane. She found that the two techniques yielded exactly opposite results. Jamison and Spang's method gives increasing stress with distance away from the fault, whilst Rowe and Rutter's method showed decreasing stress further away from the fault. The system studied is a natural fault zone. It shows a distinct evolution of grain size across its width. Gouge near the centre of the fault zone is composed of very fine grained material, whilst at 10m away from the centre, tectonic grain size reduction has had little effect. A grain size sensitive technique will automatically be influenced by grain size changes (Rowe and Rutter, 1990). Hence, it is not so surprising to see the difference between the two techniques at this level. Newman continues to state that the effective consequence of the reduction of grain size in the samples on the Jamison and Spang technique is that the CRSS of grains should be higher. The CRSS associated with calcite is a point of some discussion, but we wish to admit that it is a constant, at least in the range of temperatures and pressures undergone within the Molasse. A smaller average grain size will increase the number of grain boundary contacts, and this may impede twinning (Spiers, 1979, 1982).

Newman also pointed out that grain size distribution in a rock may influence twinning incidence given that a larger number of small grains surrounding a larger grain will increase the chances for one of the surrounding grains to provide a stress concentration favourably oriented for twinning to occur. The physics of such problems are very complex, however, Newman was able to state from her work that for the same grain size class intervals from rocks with more or less heterogeneously distributed grain sizes, there were variations in twinning incidence.

Figure 6.3 shows the grain size distributions from the samples used in this study. They are presented as percentages of twinned and untwinned grains from each grain size class. The highest percentages of twinned grains are generally found in slightly coarser grain size classes than the maximum for untwinned grains. Otherwise, there are no strong variations between samples, reflecting the similar grain sizes from each sample studied. Newman, by contrast studied rocks across a fault zone with considerable differences in grain sizes. The grain size distributions form this study probably correspond best to her 'broad and low' distributions - a large range of grain sizes.

6.3.3 CRSS

Clearly, mechanical twinning in crystals occurs only when shear stresses on the twin plane are high enough to allow twinning. The resulting assumption is that a critical shear stress exists for twinning, and for piezometry, this shear stress is assumed to be unique. (Turner et al., 1954) found a range of values for the CRSS for calcite according to both confining pressure and temperature (figure 6.4). He gave a general value of 5.9 $\pm$ 2 MPa, under conditions of some confining pressure (between 500 and 1000 MPa). Klassen-Neklyudova (1964) reviewed work on mechanical twinning in the first half of the twentieth century. Reporting the work of Garber, (pp66-67), the question of different yield points for calcite is addressed. Twinning is considered to involve several different yield points, the first to make an 'elastic twin' and apparently requiring a very high stress probably produced by a stress concentration due to flaws such as dislocations in the crystal. This initial 'elastic twin' can be ejected spontaneously when the driving stress is removed. The next limit is to make the twin permanent (residual or reducing), and is the value quoted in figure 6.4, and appears to be temperature dependent (but more so at very low temperatures).

All of Turner et al. (1954), Klassen-Neklyudova (1964) De-Bresser (1991) find that temperature influences the CRSS of calcite to some degree. Turner et al. (1954) found pressure effects to be minimal, but Klassen-Neklyudova

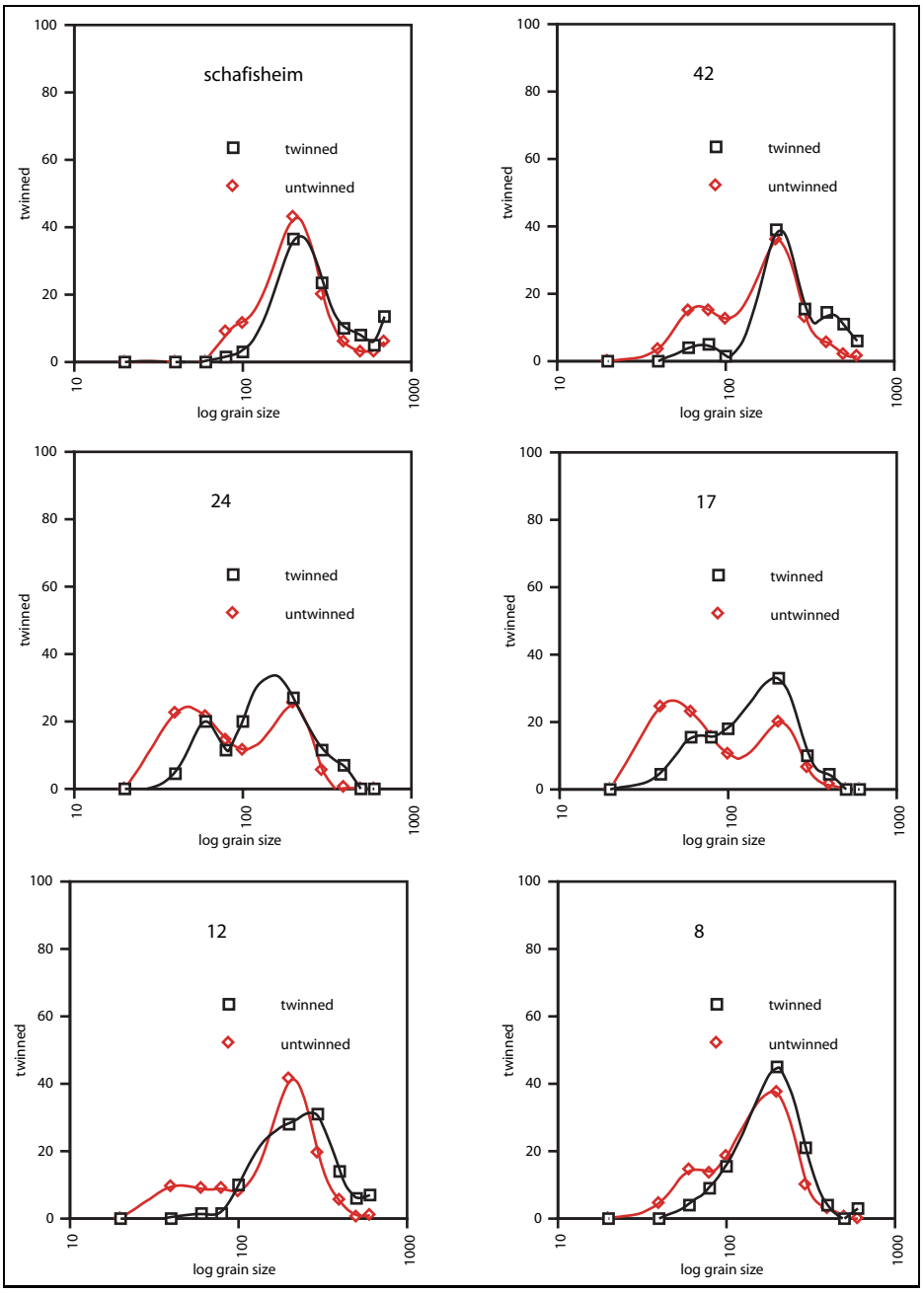

Figure 6.3: Grain size distributions of each sample. Percentages of the populations of twinned and untwinned grains are plotted for each grain size interval considered.

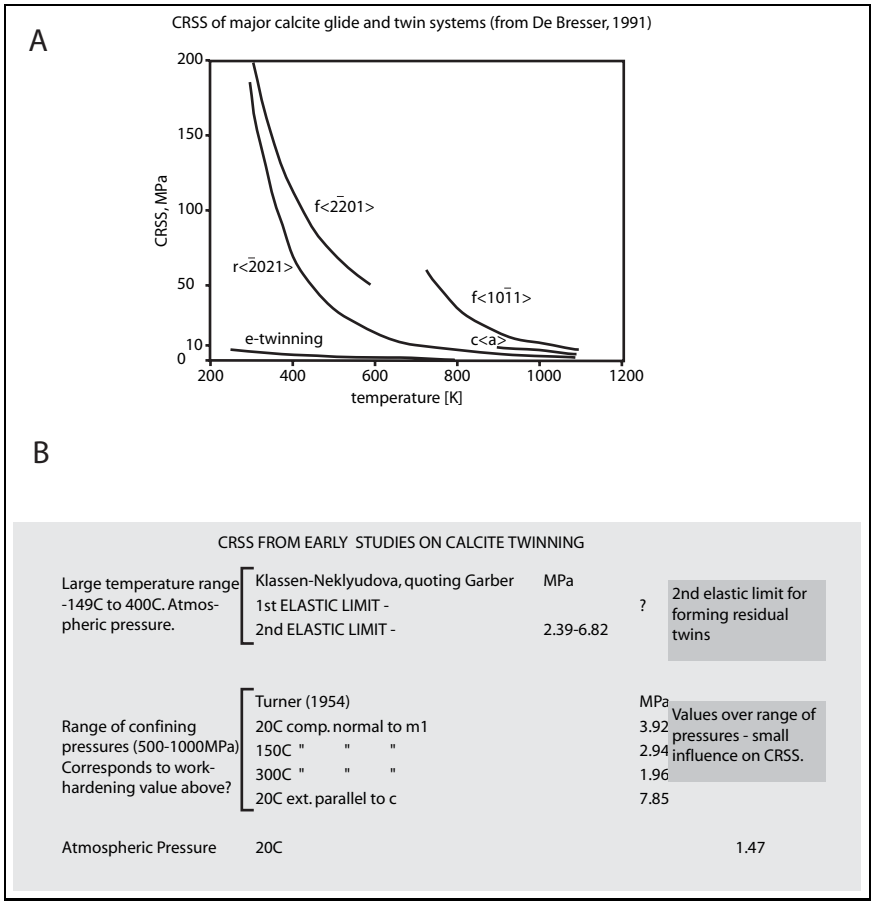

Figure 6.4: Compilation of data on twin and glide shear stresses for calcite crystals. a) form De-Bresser (1991), b) from Garber (quoted in Klassen-Neklyudova (1964) and from Turner et al. (1954).

concludes that high temperatures, high pressures and high deformation rates facilitate twinning.

De-Bresser (1991) studied other slip systems than e-twinning in calcite. However, he gives a value of 9 MPa for the e-twinning CRSS associated with some of his experiments (T=575°C). He also compares this to results of Spiers (T=500°C) of 12 MPa. He concludes that CRSS values may not have too much significance due to the importance of stress concentration effects in nucleating twins (a fact also commented on by Garber - see Klassen-Neklyudova (1964)). He also discusses the important effect of the diminution of the relative magnitude of CRSS for other slip systems in calcite and their consequent predominance at higher temperatures (figure 6.4).

Perhaps the conclusion to draw from this analysis of the sometimes contradictory data on CRSS associated with calcite twinning on e is that an experimental, transferable, constant value can be used. It may not even be a CRSS as such, but rather an arbitrary constant determined as necessary for a stress-twinning relationship. Jamison and Spang's found agreement with experimental stress magnitudes from deformed limestones using a value of CRSS of 10 MPa for their analyses. On this basis, a CRSS for calcite is acceptable. If it is really transferable between different aggregates is a different question. In the present study, the rock is not purely carbonate, and grain size inhomogeneities outside the domain of calcite crystals are very strong. The rock is poorly sorted. It has been assumed that to make such a transfer is acceptable, but no conclusion on the existence or magnitude of a real, unique CRSS for calcite is implied. What has been assumed is a general value suitable for aggregates and appropriate to the Jamison and Spang twinning incidence technique.

6.3.4 Strain

Twinning is a function of strain. Hence, large strains should produce large amounts of twinning. Twinning operating as a low temperature creep mechanism over time will produce more twins for a constant differential stress. The piezometric assumption of differential stress itself governing which twins function may not be completely true at high strains.

Twinning is assumed to have occurred in an irrotational strain field, and strain is homogeneous across a sample. With rotation, twin planes initially unfavourably oriented may twin. This will give an overestimate of the differential stress operative in a sample. In the case of Molasse samples, the small magnitude of the internal deformation measured is reassuring as any rotational component of strain should be tiny and hence so should the associated error.

Homogeneous strain distributions across a sample are also important. Rowe and Rutter (1990) report the work of Spiers who found that grains favourably oriented for twinning accommodate twice as much strain as is theoretically expected, leading to a homogeneous stress distribution between the grains of an aggregate. This is important for any palaeostress estimation technique. Within the OMM sandstone used in this study, we must expect some stress concentrations leading to twinning activity which will be inconsistent with the prevailing, large scale differential stress.

6.4 Differential stresses from the alpine foreland

6.4.1 Study area and sample material

The Molasse Basin in Switzerland is a flexural depression in the earth's crust due to loading by the growing Western Alps from the beginning of the Tertiary period onwards. The depression is filled by Oligocene-Miocene sediments of either fluvio-lacustrine or marine character. The upper most marine series (Obere Meeres Molasse or OMM) yields coarse, sparite cemented lumachellic sandstone. These rocks contain many mechanical, calcite twins. They make a good subject to study palaeostresses, being relatively young (Mid-Late Miocene) and subject to only the latest deformation associated with the formation of the Jura mountains. Maximum shortening is confirmed to be close to the horizontal plane (see chapter 3) and by abstraction, we can assume that principal compressive stresses were also close to the horizontal plane. Finite deformation in the Molasse has been proven to be small, which reduces certain problems associated with twin palaeopiezometers (large strains increasing twinning, non-coaxial flows producing 'extra' twinning).

Using calcite twin palaeopiezometers in such a case allows us to estimate the magnitude of differential stress (peak value) for rocks. As they have a reasonably well constrained burial depth of up to 2km (Schegg, 1993), these values can then be compared to data from the present day and to other studies of palaeostresses and theoretical constraints imposed from rock mechanics. The existence of some faults in the Molasse Basin is documented, but evidence for major fractures crossing the basin is controversial. Some authors postulate strike-slip faults across the Molasse, from the Alps. At one site in this study, clear evidence for fracturing (small tear faults) has been

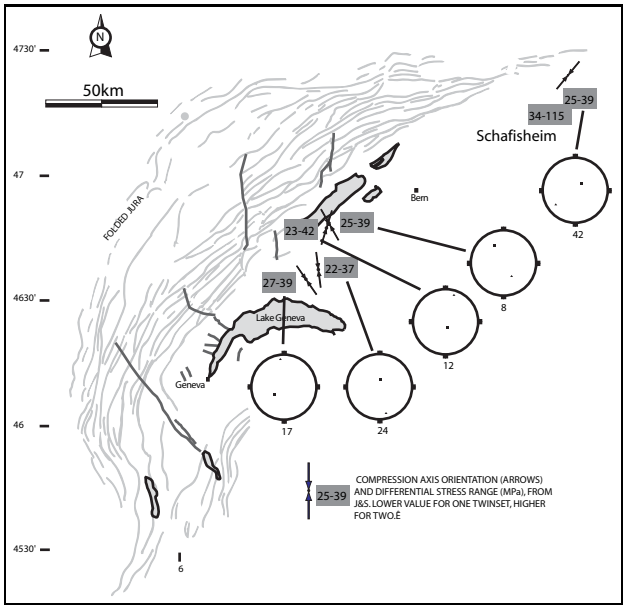

Figure 6.5: Compilation of strain and stress data for the Jura Arc and Molasse Basin. Shows compression axes (this study), and values for differential stresses (MPa) according to Jamison and Spang's method. Stereograms show principal strain axes, taken to be coincident with principal stresses. Numbers below sterograms indicate the study site.

found. Large fractures are never visible, but could very easily be hidden by extensive Quaternary deposits across the Molasse Basin.

6.4.2 Study Results

Samples of OMM sandstone gathered around western Switzerland in the Plateau region and one sample from Mesozoic limestone gathered at depth (-1100m) from a borehole at Schafisheim (figure 6.5) have been analysed using both techniques described above. The lithologies of the Molasse samples are very similar, comprising mostly carbonate material, with bioclasts, and an often well developed sparry calcite cement and also some detritic grains, often quartz and some feldspars and micas. The rocks are often conglomeratic or of coarse sand grade and frequently contain pebble size elements. Measuring twinning incidence requires a large number of grains to be examined. In general, 250-350 grains have been measured across as large a range of grain sizes as possible. The results are presented in several forms. In figure 6.2 data are plotted on curves to give S1 for Jamison and Spang's method. Figure 6.5 shows the location of the sample sites and gives corresponding strain axes determined from calcite twins as well as the numerical values for stresses from the Jamison and Spang technique. Figure 6.6 shows the results for each sample and for each grain size interval for Rowe and Rutter's technique. The percentage of twinned grains per grain size class is shown next to each data point, and the vertical axis gives the differential stress measured. Figure 6.7 gives the values for both techniques, The results for Jamison and Spang's method shown as a bar over the range between σ_D for one and two twinsets. The table below also gives these values and a 'mean stress' over all grain sizes for Rowe and Rutter's technique.

The results from the techniques are strongly contrasting. Values obtained with Rowe and Rutter's equation are more than 5 times higher than those obtained using Jamison and Spang's method (figure 6.7). Values reach as high as 230 MPa for certain grain size classes. For each sample, as can be seen in figure 6.6, the values for different grain sizes do not lie on a horizontal line implying a large range of values for each sample according to the particular grain size class interval analysed. This is in line with the findings of Newman (1994). However, between samples, both the range and magnitude of values determined are broadly similar. The mean value over all grain sizes is also given for each sample. Even here, the values fall consistently above 100 MPa. The I_t values increase fairly consistently as grain size increases, though stress values remain consistently lower for coarser grain sizes.

Jamison and Spang's technique gives a very narrow and much lower range of values (22 to 42 MPa) as can be seen in figure 6.7. The values are very consistent across the range of OMM samples, whilst higher for Schafisheim,

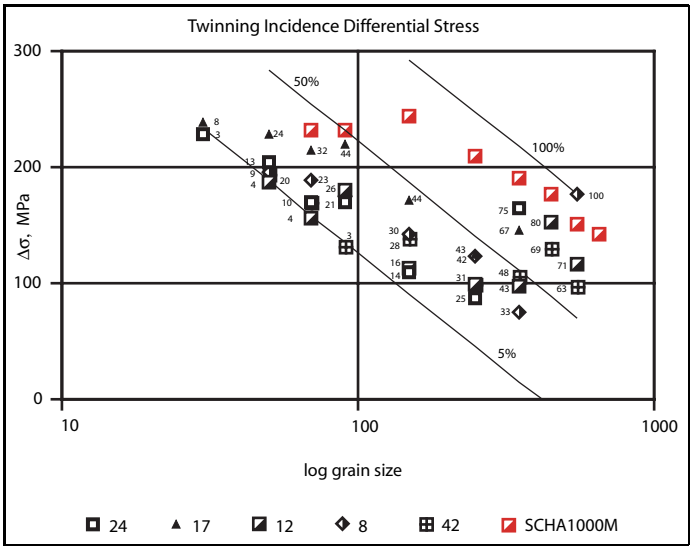

Figure 6.6: Differential stress values as determined for percentage twinning incidence per grain size category from Rowe and Rutter's technique. Numbers next to data points are the twin percent values for each grain size interval..Lines shown for 5, 50 and 100% twinning giving predictedDs.

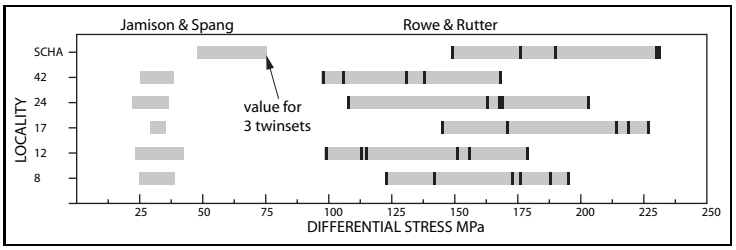

Figure 6.7: Values of differential stress from the study area (see figure 6.5 for locations). Bars indicate ranges obtained according to one or two twinsets from Jamison and Spang's technique and values for differing grain size intervals from Rowe and Rutter's technique (black bands represent the individual values for each grain size interval). Numerical values given in table 6.4.2

Table 6.1: Stress values from different techniques. Jamison and Spang for 1 and 2 twinset percentage twinning, Rowe and Rutter, mean value over all grain size intervals.

Differential Stress values Swiss Molasse Basin			
	J&S σ_D	J&S σ_D	R&R σ_D
sample no.	1 twinset	2 twinset	average
8	25	39	128
12	23	42	137
17	27	39	191
24	22	37	161
42	25	39	132
SCHAF. -1100m	34	115	196

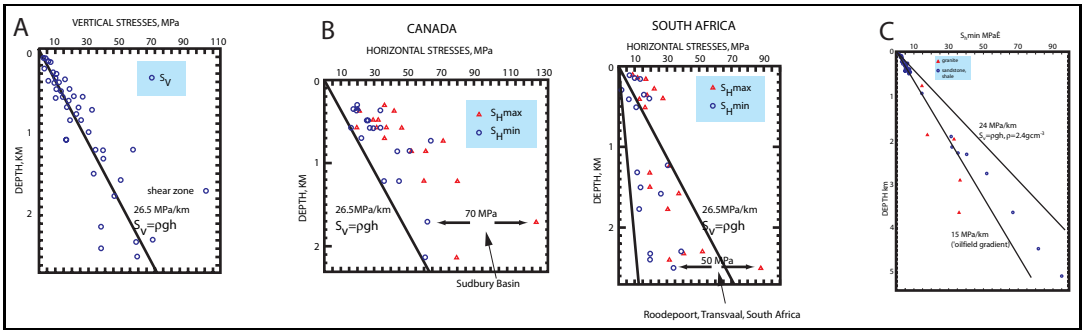

Figure 6.8: The variations in horizontal and vertical stresses from different present day stress determinations. A) Compilation of measured vertical stress magnitudes with depth. The results, though with some scatter, fit well to an assumed lithostatic pressure ($\sigma_v = \rho gh$, shown), ρ=2.7gcm^{-3}. B) Horizontal stresses from the upper crust, I) Canada (left) has always a maximum stress in the horizontal. II) South Africa, shallow measurements have a maximum stress which is horizontal, whilst deeper ones have a vertical. $\sigma_v = \rho gh$, ρ=2.7gcm^{-3} C) Minimum horizontal stresses from U.S. Basins (soft rock data) The soft rock values show; 1) low scatter 2) a deviation from the 'oilfield' stress gradient at depth. 3) minimum horizonzal stress lower than a vertical stress at a gradient of 24MPa/km ($\sigma_v = \rho gh$, ρ=2.4gcm^{-3})

an expected consequence of greater burial depth.

6.5 Present day stress measures from the lithosphere

It has already been suggested that palaeostress estimates might be compared to present day stress measures from around the world as a control on their credibility. The present study is an ideal case as it comes from a depth range for which in situ stress measures have been made and to which stress gradients can be reasonably extrapolated.

Present day stress measures down to 2km in the crust are abundant enough for good data compilations to be made over this range. The data available reveal some trends in the magnitude of stresses over a particular depth range.

6.5.1 Vertical principal stresses

McGarr and Gay (1978) produced a major compilation of stress data from around the world. They dealt with the question of vertical stresses both with respect to a linear, lithostatic gradient and the coincidence of a principal stress axis with the vertical. Figure 6.8a shows the vertical stress results, which appear to follow a constant stress gradient corresponding to a lithostatic load with a density of 2.7gcm^{-3} lending support to such a model.

6.5.2 Horizontal, compressive stresses

(McGarr and Gay (1978) produced a compilation of some of the available world-wide data on horizontal stresses and found the values to vary according to the tectonic situation. Thus, figure 6.8b shows that in South Africa, in a region affected by normal faulting, the horizontal stresses are lower than the vertical after a certain depth (1200m), are higher than vertical above 500m and are transitional between these two states at depths between 500m and 1200m. Data from Canada shows that the horizontal stress magnitudes remain consistently greater

than the vertical. The measures made along the edge of the Canadian shield are from a region which formerly underwent thrust faulting. Molasse data are broadly horizontally compressional (from the five selected Molasse sites and Schafisheim). Again, this should be so as the basin was presumably subject to compressional stresses across its width during the Miocene and Pliocene.

6.5.3 Stress reference states

Several stress reference states have been proposed for the crust, all seeking to define what a 'tectonically unmodified' stress state might be like. The simplest reference state is that of lithostatic stress, $\sigma_v = \rho g h$ and $\sigma_v = \sigma_{hmax} = \sigma_{hmin}$ which would correspond to the stress in molten rock or an igneous body which had just crystallised, or to stresses in newly buried sediments. A uniaxial strain reference state defined on the bases of uniquely vertical loading of the crust with horizontal confinement has also been suggested. The elastic, horizontal response of the rock to the vertical load would give the relationship

$$\sigma_h = \frac{\nu}{1-\nu}\sigma_v \tag{6.9}$$

McGarr (1988) (basing his work on that of Artyushkov) derived a constant horizontal stress model for the lithosphere, which, simply stated, gave an average stress to a reference thickness of lithosphere. Should that thickness be decreased, there will need to be an increase in the average horizontal stress over the thinned crust to maintain force balance. The overall result is to keep horizontal stresses close to vertical stresses over large depth ranges when there is either erosion or sedimentation. This contrasts with lateral constraint models (e.g..Haxby and Turcotte (1976), citethaxby1976b), which often predicted large changes in horizontal to vertical stress ratios.

Palaeostress magnitudes from an active, compressional area such as the Molasse, have to be provoked by something more than a non-tectonic process, which is obvious in the context of an actively shortening wedge of material like the Molasse-Jura system. This tectonic stress can be assumed to be the driving force for the Jura. How much of the differential stress to attribute to this would depend on how much the reference state would deviate from lithostatic stress. Model results for McGarr's reference state suggest not much. Therefore, we may be justified in attributing most of the differential stress to a remote, boundary compression.

6.5.4 Shear stresses determined for the crust

Studies of actual shear stresses have led to the conclusion (McGarr, 1980) that there is a linear increase in shear stress with depth at least in the first 5km of the crust and that this may be extrapolated beyond these depths. McGarr and Gay (1978) concluded that there was a large scatter in available shear stress-depth data, and that the increase in shear stress was sharper in the first kilometre than below. McGarr (1980) fitted regression lines to shear stress data to find a relationship of the form

$$\tau_m = A + Bz \tag{6.10}$$

He found that soft rock values gave a low root mean squared deviation and were fitted to a line A=3.76±1.02, B=3.80±0.6. This gradient was substantially less than for hard rock. The soft rock data from McGarr (1980) and an extrapolation to depth of the shear stress gradients for soft and hard rock are shown together in figure 6.9.

6.5.5 Orientation of principal stresses

Coincident vertical and principal stresses are less certain according to much data, but (McGarr and Gay, 1978) concluded that scatter was sufficiently small for such a situation to be. The data for this study show inclinations between 45° and 78° for least principal stresses, so approximating this situation (figure 6.5).

6.6 Evaluation of palaeostress data

6.6.1 Available palaeostress data

We have proposed a comparison of palaeostress data to theoretical strength limits we can impose on the crust. These take two forms, namely a profile corresponding to strength under frictional sliding, and material brittle failure criteria (e.g.. Coulomb failure of Mohr envelopes). Data from this study and a compilation of available data for other palaeopiezometry studies are presented in figure 6.10. These data combine both twin piezometers

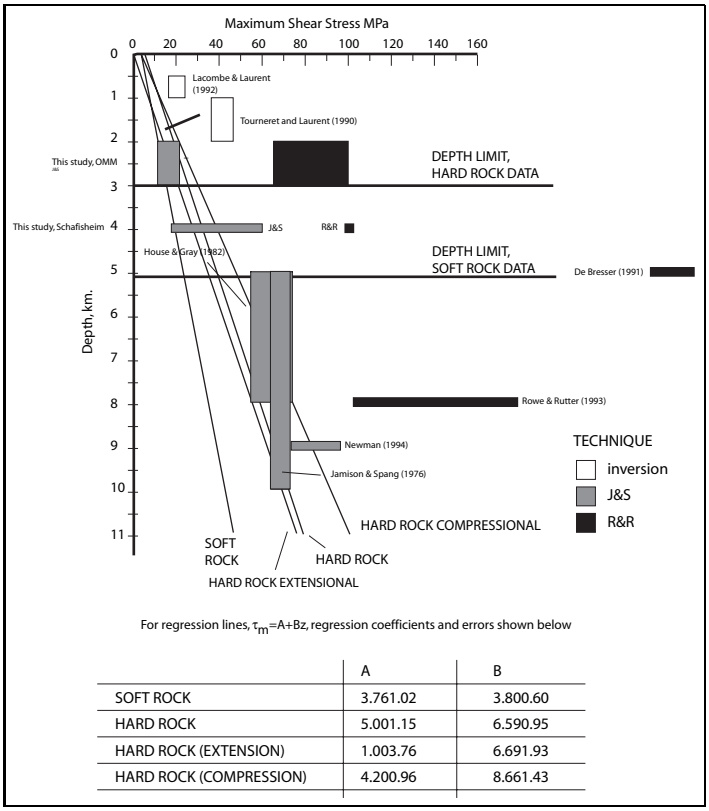

For regression lines, τ_m=A+Bz, regression coefficients and errors shown below

	A	B
SOFT ROCK	3.761.02	3.800.60
HARD ROCK	5.001.15	6.590.95
HARD ROCK (EXTENSION)	1.003.76	6.691.93
HARD ROCK (COMPRESSION)	4.200.96	8.661.43

Figure 6.9: Regression lines calculated from shear stress values for hard rock, and soft rock (McGarr, 1980), compared to palaeostress data.

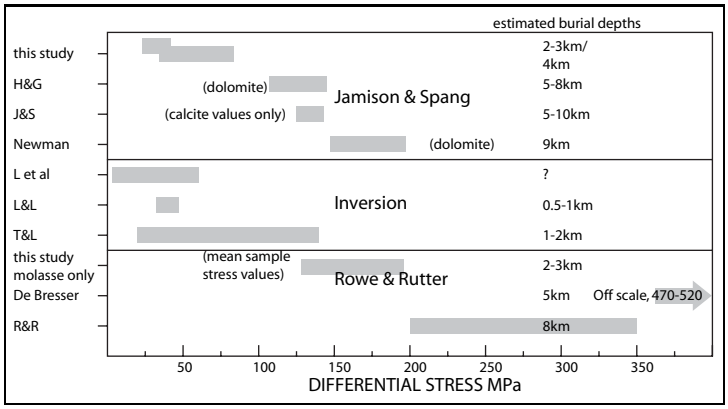

Figure 6.10: Comparative diagram of values of differential stress from other studies. Bars indicate value ranges obtained study areas according to different authors. (House and Gray, 1982; Jamison and Spang, 1976; Newman, 1994; Lacombe et al., 1990; Lacombe and Laurent, 1992; Tourneret and Laurent, 1990; De-Bresser, 1991; Rowe and Rutter, 1990).

used in the alpine foreland and a set of inversion stress magnitudes (Jamison and Spang, 1976; House and Gray, 1982; Lacombe et al., 1990; Rowe and Rutter, 1990; Tourneret and Laurent, 1990; De-Bresser, 1991; Lacombe and Laurent, 1992; Newman, 1994).

6.6.2 Strength under frictional sliding

Brace and Kohlstedt (1980), using Byerlee's law (Byerlee, 1978) defined a theoretical limit to crustal shear strength. Assuming that a body of rock will contain fractures at all orientations, and frictional sliding will take place on them whenever the resolved shear stress on a fracture plane reaches its critical value, we find a bilinear relationship over a range of normal stresses (3MPa-1.7GPa) defining the strength of the crust. In terms of the effective principal stresses, the relationship is (Brace and Kohlstedt, 1980)

$$\sigma_1 - \sigma_3 \approx 4\sigma_3 \ , \ \sigma_3 < 110\text{Mpa}$$
$$\sigma_1 - \sigma_3 \approx 3.1\sigma_3 + 210 \ , \ \sigma_3 > 110\text{Mpa}$$

Differential stress values are plotted over the estimated depth ranges for palaeostress studies mentioned in this chapter (see table 6.6.2), and are compared to the theoretical maximum differential stress according to Byerlee's law (figure 6.11). In fact, most of the studies lie well within the strength limits of dry and wet rock, where wet rock is assumed to have a hydrostatic pore pressure. The gradients shown are calculated based on an assumed vertical stress of ρgh, with a density of 2.45 gcm^{-3}, a reasonable soft rock value. Its extrapolation to depths as great as 10km is uncertain, but use of a 'hard rock' value would only push the limit values of differential stress even higher. So, in theory, any differential stress contained within these gradients would be within the limits of the strength of the earth's crust.

Table 6.2: Compilation and comparison of differential stress data from palaeostress studies.

Differential Stress from paleostress studies				
study	Depth,km	σ_D MPa	Tectonic Situation	Predicted Frictional Sliding
De Bresser	5	470-510	On the Tutt shear zone	yes
Rowe and Rutter	10	200-350	Cantabria shear zone	no
Newman	9	147-∼200	On the Pioneer Landing fault zone	no
Jamison and Spang	5-10	125-143	In McConnell thrust sheet	no
House and Gray	5-8	107-145	On Saltville River thrustplane	no
Tourneret and Laurent	1-2	40-80	Quercy Platform, N. of Pyrenees	yes
Lacombe et al.	0.5-2	3-60	Burgundy Platform, continental transform	
Lacombe and Laurent	0.5-1	32-47	Burgundy Platform, continental transform	yes
This study, J&S	2-3(4)	22-42 (35-115)	Molasse Basin, 50km from alpine front	no
This study R&R	2-3(4)	128-196	Molasse Basin, 50km from alpine front	yes

Laws of frictional sliding remain remarkably constant across all rock types (with the exception of clays). Moreover, the sliding rate and temperature has little effect on rock strength under conditions applicable to the

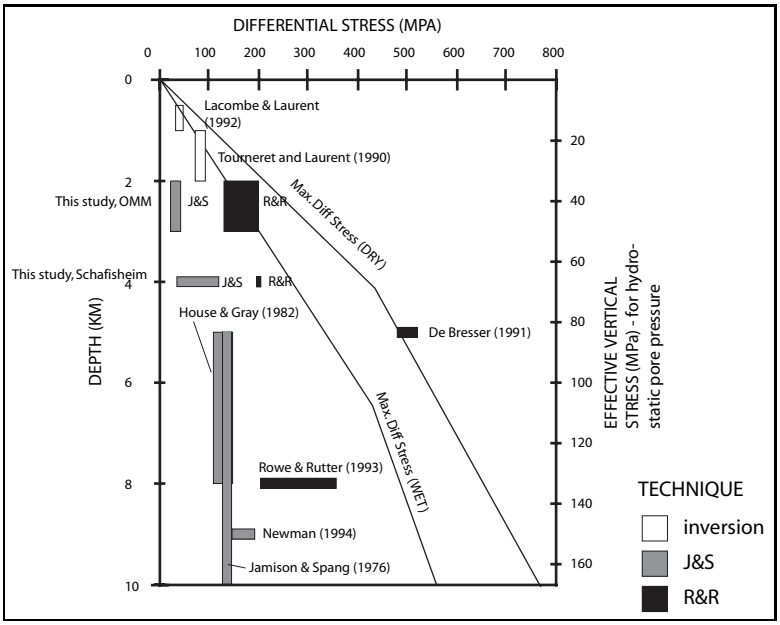

Figure 6.11: Differential stresses from palaeostress studies, and theoretical limits on differential stress levels from Byerlee's law. Extrapolated gradients are shown for hydrostatic pore pressure (WET) and for dry rock (DRY). The study data are plotted as the range of stress values over the entire estimated depth range of each study.

upper 10km of the crust. A frictional sliding law is thus suitable for defining upper limits to crustal strength

Engelder (1993) (p. 118) produced a similar diagram to figure 6.11, adding a brittle failure envelope for crystalline rock, which is much 'stronger' than the frictional sliding envelope. However, if we took certain brittle fracture criteria for limestones, they would lie within the envelope for frictional sliding. Hence, brittle fracture should take place first. The definition of any strength profile in the earth is thus very dependent on the material properties of a particular section of the crust. Application of Byerlee's Law is therefore only a general guide to an absolute limit of a differential stress value at a particular depth.

6.6.3 Use of brittle fracture criteria

In some individual cases, the fracture strength of a material may be lower than the strength during frictional sliding. This can be determined by laboratory analysis on samples of the rock in question at pressures and temperatures approaching those known to have affected the material, defining the failure envelope. Brace and Kohlstedt (1980) pointed out the large variations in fracture criteria under identical conditions, and argued that Byerlee's law provided a better guide to strength of the crust. However, certain brittle fracture criteria have been used in conjunction with palaeostress studies. De-Bresser (1991) compared his results for differential stress determinations in the Tutt shear zone of South Wales to a Mohr failure envelope for the Tutt limestone. By setting σ_3 to the value of effective confining pressure estimated for the shear zone (80 MPa), the Mohr circle's diameter is then increased to become tangent to the failure envelope, at which size, its diameter equals peak, theoretical differential stress. In so doing, he obtained a value of 410MPa, which is in accordance with some of the stress analyses he carried out, but noticeably lower than values from Rowe and Rutter's technique (470-510MPa). A similar process can be attempted for the measures from this study. However, no fracture data are available for the material involved. A comparison with a linear (Coulomb) fracture criterion for the Berea sandstone is shown in figure 6.12. Evidently, the values obtained from Jamison and Spang's method never approach either failure or frictional sliding. Rowe and Rutter's technique would be suggestive of cataclastic flow for the maximum stress values, but minimum stresses also just lie within the stable zones of both envelopes. The comparison to the Berea sandstone (a very weak rock) is rather arbitrary, and it would be interesting to define a Mohr failure envelope for intact samples of Molasse sandstone.

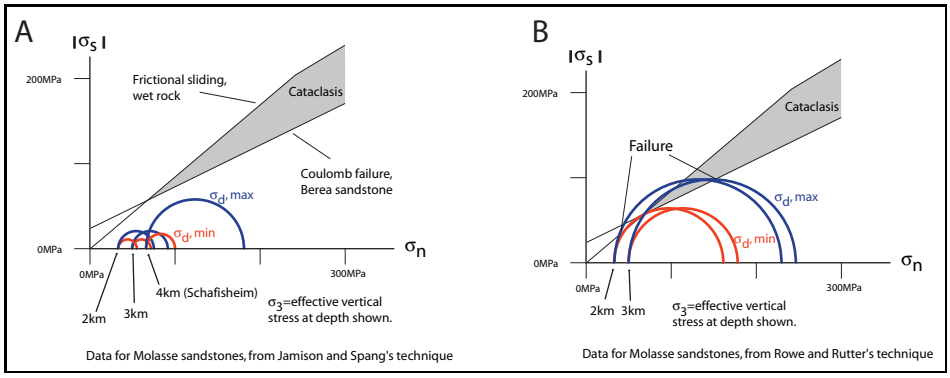

Figure 6.12: The Coulomb failure criterion and frictional sliding strength compared to differential stress estimates from Jamison and Spang's and Rowe and Rutter's techniques. A Mohr circle for minimum (a) and maximum (b) differential stress is shown.

6.6.4 Present day stresses

The comparison to present day stress measurements limits itself to that of stress orientations and shear stress values. Shear stresses for the compilation of palaeostress studies tend to be higher at shallow depths than the regression lines McGarr fitted to present day shear stresses (McGarr, 1980). There is a closer correspondence at greater depths (figure 6.9). There is no discernible linear gradient in shear stress values from palaeostress studies. Orientation data (figure 6.5) for both present day measures and those made in the Molasse Basin confirm a general alignment of principal stresses with the vertical and horizontal directions in the earth.

6.6.5 Discussion

Values of differential stress found for the alpine foreland show a strong contrast between the two palaeopiezometers used. The most likely reason for the discrepancy is the temperature and pressure conditions under which the piezometers were calibrated. Rowe and Rutter's technique was applied to a temperature range where different slip systems in calcite appear to compete strongly with e plane twinning (De-Bresser, 1991; Burkhard, 1993). It is not proven that the calibrations are extendible to lower temperature regimes such as would have existed in the Molasse Basin (Schegg, 1993). This would explain possible overestimates of differential stress in the alpine foreland study. Jamison and Spang's technique was proven for low temperature deformation but loses accuracy under increasing strain. The OMM material examined from the alpine foreland has suffered minute internal strains (horizontal shortenings of probably $<1\%$) and so lies well within the margins of accuracy of the technique. A question remains over the influence of grain size heterogeneity on results. The Molasse lithology is both not pure carbonate and also contains a wide variety of calcite grain sizes. Grain size fractions of $>20\mu$m have been used. As the values yielded by the Jamison and Spang technique fall within the stability envelope of frictional sliding and should be well within the limits of brittle fracture of the material from which they come, they are preferred to those from Rowe and Rutter's technique.

The general success of most of the studies compiled here is measured by the fact that most of them lie within a frictional sliding envelope, which is assumed to be the upper limit of strength of the earth's crust. Lying within this envelope does not preclude new fractures forming at lower stresses. Higher pore fluid pressures would also allow easier sliding on pre-existing fractures as might the presence of gouge material or crushed grains. Hence, the limits of differential stress could be set lower than the frictional sliding envelope shown, in which case, the piezometric estimates are not totally constrained. Comparison to a determined brittle fracture envelope (Mohr envelope) for the material adds an additional check. For all the studies considered, it appears that the choice of piezometer influences the results. Higher stresses seem to be consistently recorded by Rowe and Rutter's technique. In the case of the Tutt shear zone (De-Bresser, 1991), the failure envelope determined precludes the high differential stress suggested by Rowe and Rutter's technique (failure of a Tutt limestone sample was at 410MPa) which provides good evidence of a stress overestimate. The inversion techniques are all from studies at shallow depths, and suggest similar problems of overestimation of stresses (compare figure 6.11). More data from greater burial depths would be helpful to truly evaluate their usefulness.

As table 6.6.2 also shows, certain of the studies have been carried out close to or on faults or shear zones.

These are normally zones of locally very high strain, and as twinning is a function of strain, the accuracy of piezometers suffers. This is known to be the case with Jamison and Spang's technique, though Rowe and Rutter's method was calibrated across a range of strains (7-30%). However, with the exception of De Bresser's results from the Tutt shear zone, none of the other studies have suggested differential stresses which clearly surpass the theoretical strength of the crust at the depth to which they correspond. However, the many problems highlighted by Newman (1994) in using piezometers across fault zones where grain size certainly plays a role, and probably grain rolling, still leads to the conclusion that it may be best to avoid such regions and stick to less deformed areas, in regional studies.

The latter attempts to measure stresses from high deformation zones may explain the general discrepancy between present day and palaeostress data (figure 6.9). Studies concentrated on compression zones, close to collisional plate boundaries (as many of the palaeostress studies are) are inappropriate for comparison to data gathered from stable continental interiors as is the case for McGarr (1980). Two effects may combine, namely naturally high values due to high stresses because of the tectonic setting and artificially high values due to high strain in zones of intense deformation. Thus, it is more appropriate to compare regression data for present day stresses taken from similar tectonic settings to the palaeostress data being evaluated.

Many attempts to estimate the shear stresses operative on faults in the upper crust have been made. Citing just two of these (Scholz, 1980; Sibson, 1980) permits comparison to our palaeostress data. Scholz (1980) took evidence for heat generated by fault movement and considered the various slip rates and shear stresses required to generate the heat. Good evidence exists for metamorphism due to thrusting in the case of the Olympos thrust (Greece). Thrusting was buried under 6km of overburden and occurs in a carbonate series over a zone 1km thick, which is plastically deformed. The results of modelling showed that with high slip rates, an initial shear stress of 100 MPa would be required, but that this would rapidly diminish with increasing temperature as the carbonate rock would weaken. This analogy is drawn as the studies cited are from limestones, and the depth (6km) is comparable to several of the studies considered here. A 100 MPa shear stress means at least a 200 MPa differential stress, which is in fair agreement with palaeostress studies from similar depths.

Sibson (1980) used the presence of pseudotachylites as evidence of power dissipation associated with fault slip in the upper crust. He concluded that events could be associated with shear stresses of =10 MPa or (more rarely) =100 MPa. Again, the constraint on differential stress in the crust is vague, but none of the palaeostress data compiled are incompatible with such results.

In summary, it remains very difficult to place more confidence in any one piezometer, even after applying theoretical constraints. The piezometers should best be used in regions which underwent deformation at similar temperatures and pressures (and strains) to those used for calibrating a particular technique.

6.7 Tectonic setting of the alpine foreland

The question of what exactly has generated the differential stresses in the alpine foreland has not been directly addressed. Figure 6.13 shows the plate wide stress field believed to affect Northwest Europe (Zoback, 1992). Most of the region Northwest of the Alps shows a trend of horizontal compressive stresses directed Northwest or north Northwest. However, some deviations of the stress field around the Alps (particularly the western Alps) are noted, and have been explained as due to the north south trending Alps and their root which provide a strong density contrast to adjacent material. It is possible (Zoback, 1992), knowing the degree of rotation of a plate wide stress field and the strike of the structure producing the deflection, to calculate the relative magnitudes of a regional differential stress and the superimposed local stress. In the case of the Alps, the estimates show a local stress 2.5 times greater than the plate wide one.

However, this explanation may well work for the western Alps, but the situation affecting the Jura region is different. Borehole strain gauge measures made around the eastern Jura and central Jura by Becker (Becker et al., 1987; Becker and Werner, 1995) have yielded stress axes orientations and differential stress magnitudes at shallow depths. The important question of stress at depth and decoupling over a dcollement is also discussed in these papers. Becker et al. (1987) and Becker and Werner (1995) found that the stress field in the detached cover of the Jura mountains is rotated above a stress field in the 'basement' which remains consistent with the plate wide trend. This situation suggests that at least the action of local stresses is on a far smaller volume of material due to the fact that it is detached. Hence, local stresses due to the adjacent, relief of the Alps, with strong density contrasts must completely dominate the stress regime. The horizontal component of stress generated by this surpasses the vertical and will be responsible for the fairly large differential stresses recorded most reliably by Jamison and Spang's technique. The role of the weak detachment in decoupling the uppermost part of the

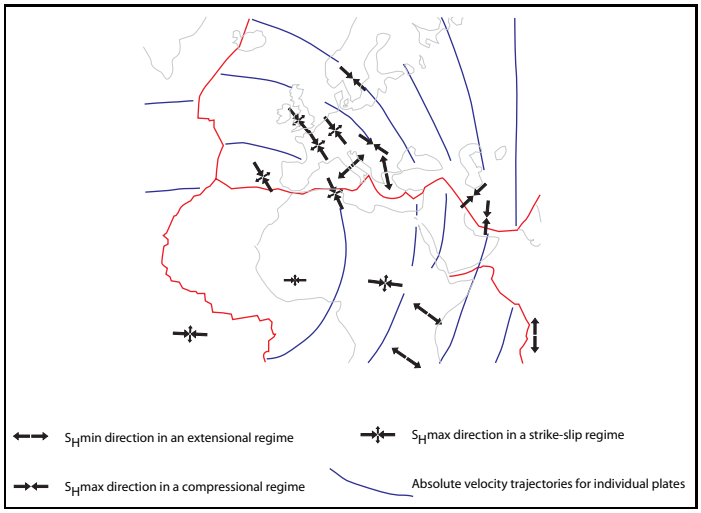

Figure 6.13: World stress map averaged stress orientations for clusters of data from the European/North African region (from Zoback (1992).

crust is essential.

6.8 Stress anisotropy and the magnitude of horizontal stresses

The ratio of horizontal to vertical stresses can be estimated very simply. Schegg (1993); Schegg et al. (1997) have found through thermal modelling that Late Tertiary erosion of 2000-2600 metres has occurred in the Molasse Basin. Presumably, the vertical effective stress acting on the rock would be

$$\sigma_{v-eff} = \sigma_v - 0.4\rho g h \tag{6.11}$$

We have already stated the maximum principal stress lies in the horizontal plane. It must therefore be larger than σ_{v-eff} by a proportion related to the size of the differential stress. We know all the values necessary to derive σ_{h-eff} and we have different possible values of differential stress. We can thus determine the stress ratio

$$A = \frac{\sigma_{h-eff}}{\sigma_{v-eff}} \tag{6.12}$$

A is shown graphically (figure 6.14) for the different possible σ_D values determined in the study. A varies over the depth range plotted (down to 5km). At 2600m overburden, the lowest estimate of A is 1.46 (for 20MPa) - weakly anisotropic, whilst at 2000m, it is 1.6. If we take σ_D = 40MPa, we arrive at 1.92 and 2.20 respectively. The anisotropies suggested by Rowe and Rutter's technique are far stronger (5.4 - 6.7). Values for maximum principal stress can also be inferred. For the same depths, for σ_D = 20MPa, we have 85 - 100 MPa principal stress. For σ_D= 40MPa, we get 116 - 132 MPa and these are the horizontal stresses through the Molasse Basin as it pushed into the Jura.

6.9 General Conclusions

It continues to prove difficult to constrain the magnitude of stresses in the crust. Present day direct measurements go no deeper than 6km, below which depth, we are forced to make inferences from earthquake data.

We can place upper limits on the strength of the upper crust, but they remain subject to large fluctuations according to stress regime, fluid pressures etc. Theoretical considerations of mechanisms of faulting and energy considerations also only allow an approximation to an order of magnitude for the strength of faults. However, it is rare to find shear stresses postulated above 150 MPa.

Within this context of uncertainty, palaeostress estimates remain useful nut cannot be over-interpreted as no definite proof of their accuracy outside laboratory conditions and time scales exists. Moreover, the two techniques used here seem applicable to two very different temperature and pressure regimes, which explains the large

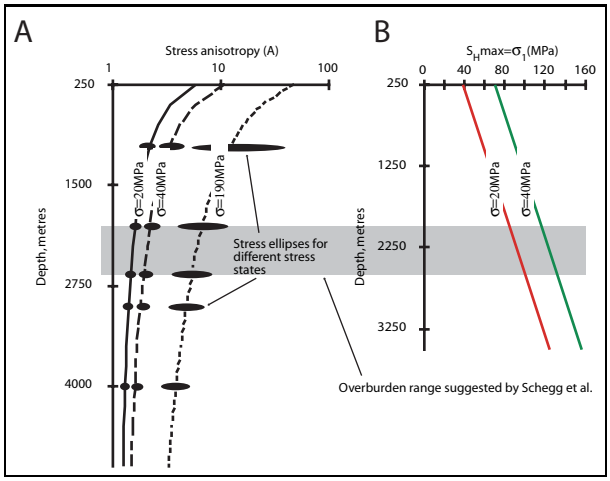

Figure 6.14: a) Graph showing the different stress anisotropies for 3 different values of s over a range of overburden values. Stress ellipses representative of the different stress states at 1000, 2000, 2600, 3000 and 4000metres overburden are shown. b) Horizontal, maximum principal stress values for two σ values are shown as a function of overburden. For both graphs, the overburden range suggested by Schegg et al. (1997) is shown as a grey shaded area.

discrepancy between values from Rowe and Rutter's and Jamison and Spang's techniques in the alpine foreland study.

We accept the Jamison and Spang techniques results for the alpine foreland considering the low strain, low temperature and shallow burial that the material has undergone. Hence, we can conclude that the best estimates of differential stresses in the alpine foreland at the time of the rise of the Jura mountains lie between 20 and 40 MPa, which should neither provoke fracture nor cataclastic flow in the material. This is compatible with the field evidence for very little fracturing. The stresses in the alpine foreland appear to be local ones, related to the relief of the adjacent Alps. Presumably, the differential stresses measured from the foreland basin relate directly to the horizontal push which made the Jura.

Bibliography

Allen, P., Homewood, P., Williams, G., 1986. Foreland Basins: an introduction. In: Allen, P., Homewood, P. (Eds.), Foreland Basins. Special Publications of the International Association of Sedimentologists. Blackwell Scientific, London, pp. 3–12.

Angelier, J., 1994. Fault slip analysis and paleostress reconstruction. In: Hancock, P. (Ed.), Continental Deformation. Pergamon Press, Oxford, pp. 53–100.

Argand, E., 1922. La tectonique de l'Asie. In: Extrait du compte-rendu du XIIIe congrès géologique international. Congrès Géologique Internationale, Brussels, pp. 171–372.

Aubert, D., 1945. Le Jura et la tectonique d'écoulement. Memoire de la Société Vaudoise des Sciences Naturelles. 8, 217–236.

Aubert, D., 1959. Le décrochement de Pontarlier et l'orogenèse du Jura. Memoire de la Société Vaudoise des Sciences Naturelles. 12, 93–152.

Bai, W., Vigny, C., Ricard, Y., Froidevaux, C., 1992. On the origin of deviatoric stresses in the lithosphere. Journal of Geophysical Research 97 (B8), 11729–11737.

Becker, A., Blümling, P., Müller, W., 1987. Recent stress fields and neotectonics in the Eastern Jura mountins, Switzerland. Tectonophysics 135, 277–288.

Becker, A., Werner, D., 1995. Neotectonic state of stress in the Jura mountains. Geodinamica Acta 8 (2), 99–111.

Berger, Z., 1994. Satellite Hydrocarbon Exploration. Springer Verlag.

Bergerat, F., 1987. Paléo-champs de contrainte tertiaires dans la plate-forme européenne au front de l'orogène alpin. Bulletin de la Société géologique de France 8 (3), 611–620.

Besse, J., Courtillot, V., 1991. Revised and synthetic apparent polar wander path of the African, Eurasian, North American and Indian plates, and true polar wander since 200 Ma. Journal of Geophysical Research 96 (B3), 4029–4050.

Bitterli, T., 1988. Die dreidimensionale Massenbilanz - ein wichtiges Hilfsmittel zum Verständnis der regionalen Kinematik (Schuppenzone von Reigoldswil, Faltenjura). Eclogae geologicae Helvetiae 81, 415–431.

Boyer, S., Elliott, D., 1982. The geometry of thrust systems. AAPG Bulletin 66, 1196–1230.

Brace, W., Kohlstedt, D., 1980. Limits on lithospheric stress imposed by laboratory experiments. Journal of Geophysical Research 85 (B11), 6248–6252.

Burbank, D., Engesser, B., Matter, A., Weidmann, M., 1992. Magnetostratigraphic chronology, mammalian faunas and stratigraphic evolution of the Lower Freshwater Molasse, Haute Savoie, France. Eclogae Geologicae Helvetiae 85, 399–431.

Burchfiel, B., 1980. Eastern European alpine system and the Carpathian Orocline as an example of collision tectonics. Tectonophysics 63, 31–61.

Burkhard, M., 1990. Aspects of the large scale Miocene deformation in the most external part of the Swiss Alps. Eclogae Geologicae Helvetiae 83 (3), 559–583.

Burkhard, M., 1993. Calcite twins, their geometry, appearance and significance as stress-strain markers and indicators of tectonic regime: a review. Jounral of Structural Geology 15 (3), 351–368.

Burkhard, M., Sommaruga, A., 1998. Evolution of the Western Swiss Molasse Basin: structural relationships with the Alps and the Jura belt. In: MAscle, A., Puigdefabregas, C., Lüterbacher, H., Fernandez, M. (Eds.), Cenozoic foreland basins of western europe. Vol. 134 of Geological Society Special Publication. London, pp. 279–298.

Buxtorf, A., 1916. Prognosen und Befunde beim Hauensteinbasis und Grenchenberg tunnel und die bedeutung der letztere für die Geologie der Juragebirges. Verh. Naturforsch. Ges. Basel 27, 185–254.

Byerlee, J., 1978. Friction in rocks. Pure and Applied Geophysics 116 (3), 615–626.

Carey, S., 1955. The orocline concept in geotectonics. Proceedings of the Royal Society of Tasmania 89, 255–288.

Chapple, W., 1978. Mechanics of thin-skinned fold-and-thrust belts. Geological Society of America, Bulletin 89, 1189–1198.

Chenevart, C., 1978. Seismic profiles as related to wrench-faulting in the Swiss Molasse Basin. Eclogae Geologicae Helvetiae 71 (1), 53–60.

Chinnery, M., 1961. The deformation of the ground around surface faults. Bulletin of the Seismological Society of America 51 (3), 355–372.

Cobbold, P., 1977. Compatibility equations and the integration of finite strains in two dimensions. Tectonophysics 39, T1–T6.

Cobbold, P., 1979. Removal of finite deformation using strain trajectories. Journal of Structural Geology 5, 299–305.

Conel, J., 1962. Studies of the development of fabrics in some naturally deformed limestones. Ph.D. thesis, California Institute of Tecnology, Pasadena, unpublished.

Cowie, P., Scholz, C., 1992. Displacement-length scaling relationship for faults: data synthesis and discussion. Journal of Structural Geology 14 (10), 1149–1156.

Dahlen, F., 1990. Critical taper model of fold-and-thrust belts and accretionary wedges. Annual Review of Earth and Planetary Sciences 18, 55–99.

Davis, D., Lillie, R., 1993. Changing mechanical response during continental collision: active examples from the foreland thrust belts of pakistan. Journal of Structural Geology 16 (1), 21–34.

De-Bresser, J., 1991. Intracrystalline deformation of calcite. Ph.D. thesis, Utrecht.

Debrand-Passard, S., Courbouleix, S., Leinhardt, M.-J., 1984. Synthèse géologique du Sud-Est de la France. Stratigraphie et Paléogographie. Orléans.

Diebold, P., Naef, H., Amman, M., 1991. Zur Tektonik der Zentralen Nordschweiz. Nagra, Baden.

Eldredge, S., Bachtadse, V., der Voo, R. V., 1985. Paleomagnetism and the orocline hypothesis. Tectonophysics 119, 153–179.

Engelder, T., 1993. Stress regimes in the lithosphere. Princeton University Press.

England, P., Jackson, J., 1989. Active deformation of the continents. Annual Review of Earth and Planetary Science Letters 17, 197–226.

Ferrill, D., 1991. Curvature development and limestone deformation in the northern subalpine chain (Haute Savoie, France). Ph.D. thesis, University of Alabama, unpublished.

Ferrill, D., Groshong, R., 1993. Kinematic model for the curvature of the northern Subalpine Chain, France. Journal of Structural Geology 15, 523–541.

Freund, R., 1970. Rotation of strike-slip faults in Sistan, southeast Iran. Journal of Geology 78, 18–200.

Friedman, M., Heard, H., 1974. Principal stress ratios in Cretaceous limestones from the Texas Gulf Coast. AAPG Bulletin 58 (1), 71–78.

Gehring, A., Keller, P., Heller, F., 1991. Paleomagnetism and tectonics of the Jura arcuate mountain belt in France and Switzerland. Tectonophysics 186, 269–278.

Gorin, G., Signer, C., Amberger, G., 1993. Structural configuration of the western Swiss Molasse Basin as defined by reflection seismic data. Eclogae Geologicae Helvetiae 86, 693–715.

Graham, R., 1978. Wrench faults, arcuate fold patterns and deformation in the southern French Alps. Proceedings of the Geological Association 89 (2), 125–142.

Gratier, J.-P., Guiller, B., 1993. Compatibility constraints on folded strata and calculation of total displacement using computational restoration (UNFOLD program). Journal of Structural Geology 15, 1–14.

Gratier, J.-P., Ménard, G., Arpin, R., 1989. Strain-displacement compatibility and restoration of the Chaînes Subalpines of the western Alps. In: Coward, M., Dietrich, D., Park, R. (Eds.), Alpine Tectonics. Vol. 45 of Geol. Soc. Spec. Pub. London, pp. 65–81.

Groshong, R., 1972. Strain calculated from twinning in calcite. Geological Society of America Bulletin 83, 2025–2038.

Groshong, R., 1974. Experimental test of least-squares strain guage calculation using twinned calcite. Geological Society of America Bulletin 85, 1855–1864.

Guellec, S., Mugnier, J., Tardy, M., Roure, F., 1990. Neogene evolution of the western alpine foreland in the light of ECORS data and balanced cross sections. In: Roure, F., Heitzmann, P., Polino, R. (Eds.), Deep Structure of the Alps. Vol. 1 of Mem. Soc. Geol. Suisse. Zürich, pp. 165–184.

Haxby, W., Turcotte, D., 1976. Stresses induced by the addition or removal of overburden and associated thermal effects. Geology 4, 181–184.

Heim, A., 1921. Geologie der Schweiz. Band I Molasseland und Juragebirge. Tauchniz, Leipzig.

Higgs, D., Handin, J., 1959. Experimental deformation of dolomite single crystals. Bulletin of the Geological Society of America 70, 245–278.

Hindle, D., 1997. Quantifying stresses and strains from the Jura arc and their usefulness in choosing a deformation model for the region. Ph.D. thesis, Université de Neuchâtel.

Hindle, D., Burkhard, M., 1999. Strain, displacement and rotation associated with the formation of curvature in fold belts; the example of the Jura arc. Journal of Structural Geology 21, 1089–1101.

Hobbs, B., 1971. The analysis of strain in folded layers. Tectonophysics 11, 329–375.

Homberg, C., 1996. Analyse des déformations cassantes dans le jura et modélisation numrique des perturbations des contraintes tectoniques autour d'accidents majeurs. Ph.D. thesis, Université Paul et Marie Curie, Paris, unpublished.

Homberg, C., Angelier, J., Bergerat, F., Lacombe, O., 1994. Nouvelles données tectoniques dans le Jura externe: apport des paléocontraintes.

Homberg, C., Hu, J., Angelier, J., Bergerat, F., Lacombe, O., 1997. Characterization of stress perturbations near major fault zones: insights fro 2-D distinct element numerical modelling and field studies (Jura mountains). Journal of Structural Geology 19 (5), 703–718.

Homberg, C., Lacombe, O., Angelier, J., Bergerat, F., 1999. New constraints for indentation mechanisms in arcuate belts from the Jura Mountains, France.

Homewood, P., 1986. Geodynamics and palaeogeography of the Western Molasse Basin: a review. Giornale di Gelogia 48 (1-2), 275–284.

Homewood, P., Allen, P., Williams, G., 1986. Dynamics of the Molasse Basin of western Switzerland. In: Allen, P., Homewood, P. (Eds.), Foreland Basins. Vol. 8 of Special Publications of the International Association of Sedimentologists. Blackwell Scientific, pp. 199–217.

House, W., Gray, D., 1982. Cataclasites along the Saltville thrust, USA and their implications for thrust-sheet emplacement. Journal of Structural Geology 4 (3), 257–269.

Howard, J., 1967. Recent deformation at Buena Vista Hills, California. American Journal of Science 266, 737–757.

Howard, J., 1968. The role of displacements in analytical structural geology. Geological Society of America Bulletin 79, 1846–1852.

Illies, J., 1974. Taphrogenesis and plate tectonics. In: Illies, J., Fuchs, K. (Eds.), Approaches to taphrogenesis. Vol. 8 of Geodyn. Sci. Rep. Schweizerbart'sche. Stuttgart, pp. 433–460.

Isacks, B., 1988. Uplift of the Central Andean plateau and bending of the Bolivian Orocline. Journal of Geophysical Research 93, 3211–3231.

Jamison, W., Spang, J., 1976. Use of calcite twin lamellae to infer differential stress. Geological Society of America Bulletin 87, 868–872.

Jordan, P., 1994. Evaporite als Abscherhorizonte. Eine gefgekundlich-strukturgeologische Untersuchung am Beispiel der Nordschweizer Trias. In: Matériaux Carte Géologique Suisse. Vol. 164. p. 79.

Karner, G., Watts, A., 1983. Gravity anomalies and flexure of the lithosphere at mountains ranges. Journal of Geophysical Research 88, 10449–10447.

Kempf, O., Schlunegger, F., Strunck, P., Matter, A., 1998. Paleomagnetic evidence for late Miocene rotation of the Swiss Alps: results from the north Alpine foreland basin. Terra Nova 10 (1), 6–10.

Kiraly, L., 1969. Brèf commentaire à la carte structurale de la surface Argovien-Sequanien dans le canton de Neuchâtel. Bulletin de la Société Neuchâteloise des Sciences Naturelles 92, 71–73.

Klassen-Neklyudova, M., 1964. Mechanical Twinning of Crystals. Consultants Bureau, New York.

Lacombe, O., Angelier, J., Byrne, D., Dupin, J., 1993. Eocene-oligocene tectonics and kinematisc of the Rhine-Sâone continental transform zone. Tectonics 12 (4), 874–888.

Lacombe, O., Angelier, J., Laurent, P., Bergerat, F., 1990. Joint analyses of calcite twins and fault slips as a key for deciphering polyphase tectonics: Burgundy as a case study. Tectonophysics 182, 279–300.

Lacombe, O., Laurent, P., 1992. Determination of principal stress magnitudes using calcite twins and rock mechanics data. Tectonophysics 202, 83–93.

Laubscher, H., 1961. Die Fernschubhypothese der Jurafaltung. Eclogae Geologicae Helvetiae 54 (1), 221–282.

Laubscher, H., 1965. Ein kinematisches Modell der Jurafaltung. Eclogae Geologicae Helvetiae 58 (1), 232–316.

Laubscher, H., 1972. Some overall aspects of Jura dynamics. American Journal of Science 272, 293–304.

Laubscher, H., 1980. Basement uplift and décollement in the Molasse Basin. Eclogae Geoloigicae Helvetiae 54 (1), 221–282.

Laubscher, H., 1986. The eastern Jura: Relations between thin-skinned and basement tectonics, local and regional. Geologische Rundschau 75 (3), 535–553.

Laubscher, H., 1992. Jura kinematics and the Molasse basin. Eclogae geologicae Helvetiae 85 (3), 653–676.

Lee, J., Angelier, A., 1994. Paleostress trajectories maps based on the results of local determinations: the “lissage” program. Computer and Geosciences 20 (2), 161–191.

Léger, M., Thibaut, M., Gratier, J.-P., Morvin, J.-M., 1997. A least squares method for multisurface unfolding. Journal of Structual Geology 19 (5), 735–743.

Lemoine, M., Bas, T., Arnaud-Vanneau, A., Arnaud, H., Dumont, T., Gidon, M., Bourbon, M., de Graciansky, P.-C., Rudkiewicz, J.-L., Mgard-Galli, J., Tricart, P., 1986. The continental margin of the Mesozoic Tethys in the western Alps. Marine and Pertroleum Geology 3, 178–199.

Lisle, R., 1992. Constant bed length folding: three-dimensional implications. Journal of Structural Geology 14 (2), 245–252.

Lowrie, W., Hirt, A., 1986. Paleomagnetism in arcuate mountain belts. Vol. 21 of Developments in Geotectonics. Elsevier, pp. 141–158.

Malvern, L., 1969. Introduction to the mechanics of a continuous medium. Prentice-Hall, New York.

Marshak, S., 1988. Kinematics of orocline and arc formation in thin-skinned orogens. Tectonics 7 (1), 73–86.

Marshak, S., Wilkerson, M., Hsui, A., 1992. Generation of curved fold-thrust belts: Insight from simple physical and analytical models. In: McClay, K. (Ed.), Thrust Tectonics. Chapman and Hall, pp. 83–92.

McCoss, A., 1988. Restoration of transpression/transtension by generating the three-dimensional, segmented helial loci of deformed lines across structure contour maps. Journal of Structural Geology 10, 109–120.

McGarr, A., 1980. Some constraints on levels of shear stress in the crust from observations and theory. Journal of Geophysical Research 85 (B11), 6231–6238.

McGarr, A., 1988. On the state of lithospheric stress in the absence of applied tectonic forces. Journal of Geophysical Research 93 (B11), 13609–13617.

McGarr, A., Gay, N., 1978. State of stress in the earth's crust. Annual Review of Earth and Planetary Science 6, 405–436.

Means, W., 1976. Stress and Strain; Basic Concepts of Continuum Mechanics for Geologists. Springer-Verlag.

Merle, O., 1989. Strain models within spreading nappes. Tectonophysics 165, 57–71.

Molnar, P., 1983. Average regional strain due to slip on numerous faults of different orientations. Journal of Geophysical Research 88 (B88), 6430–6432.

Mugnier, J., Guellec, S., Ménard, G., Roure, F., Tardy, M., Vialon, P., 1990. A crustal scale balanced cross-section through the external Alps deduced from the ECORS profile. In: Roure, F., Heitzmann, P., Polino, R. (Eds.), Deep structure of the Alps. Vol. 1 of Mémoire de la société géologique suisse. Zürich.

Newman, J., 1994. The influence of grain size and grain size distribution on methods for estimating palaeostresses from twinning in carbonates. Journal of Structural Geology 16 (12), 1589–1601.

Pavoni, N., 1961. Faltung durch Horizontalvershiebung. Eclogae Geologicae Helvetiae 54 (2), 515–534.

Philippe, Y., 1994. Transfer zone in the southern Jura thrust belt (eastern France): Geometry, development and comparison with analogue modelling experiments. In: Mascle, A. (Ed.), Hydrocarbon and Petroleum Geology of France. European Association of Petroleum Geology, 327-346.

Philippe, Y., 1995. Rampes latérales et zones de transfer dans les chaines plissées: géométrie, conditions de formation et pièges structuraux associés. Ph.D. thesis, Université de Savoie Chambery.

Philippe, Y., Coletta, B., Deville, E., Mascle, A., 1996. The jura fold-and-thrust belt: a kinematic model based on map-balancing. In: Ziegler, P., Horvath, F. (Eds.), Peri-Tethys Memoir 2: Structure and Prospects of Alpine Basins and Forelands. Vol. 170 of Mémoire du Musée national d'histoire naturel. pp. 235–261.

Plancherel, R., 1979. Aspects de la déformation en grand dans les Préalpes médianes plastiques entre Rhône et Aar. Eclogae Geologicae Helvetiae 72 (1), 145–214.

Platt, J., Behrmann, J., Cunningham, P., Dewey, J., Helman, M., Parisch, M., Shepley, M., amd P. Weston, S. W., 1989a. Kinematics of the Alpine arc and the motion history of Adria. Nature 337, 158–161.

Platt, J., Lister, G., Cunningham, P., Weston, P., Peel, F., Baudin, T., Dondey, H., 1989b. Thrusting and backthrusting in the Briançonnais domain of the western Alps. In: Coward, M., Dietrich, D., Park, R. (Eds.), Alpine Tectonics. Vol. 45 of Special Publications of the Geological Society. Geol. Soc., London, pp. 135–152.

Plessmann, W., 1972. Horizontal stylolithen im französisch-schweizerischen Tafel-und faltenjura und ihre einpassung in den regionalen Rahmen. Geologische Rundschau 61, 332–347.

Ramsay, J., 1976. Displacement and Strain. In: A discussion on natural strain and geological structure. Vol. 283 of Philosophical Transactions of the Royal Society. Royal Society of London, pp. 3–25.

Ramsay, J., Graham, R., 1970. Strain variation in shear belts. Canadian Journal of Earth Sciences 7, 786–813.

Reches, Z., 1978. Analysis of faulting in a three-dimensional strain field. Tectonophysics 47, 109–129.

Ries, A., Shackleton, R., 1976. Patterns of strain variations in arcuate fold belts. Philosophical Transactions of the Royal Society of London A283, 281–288.

Rowe, K., Rutter, E., 1990. Palaeostress estimation using calcite twinning: experimental calibration and application to nature. Journal of Structural Geology 12 (1), 1–17.

Sanderson, D., Marchini, W., 1984. Transpression. Journal of Structural Geology 6 (5), 449–458.

Schardt, H., 1906. Deux coupes générales à travers la chaîne du Jura. Archives des Sciences Physiques et Naturelles, Genève XXIII.

Schardt, H., 1908. Les causes du plissement et des chevauchements dans le Jura. Eclogae Geologicae Helvetiae X, 484–488.

Schegg, R., 1993. Thermal maturity and history of sediments in the north Alpine foreland basin (Switzerland, France). Ph.D. thesis, Université de Genève, unpublished.

Schegg, R., Leu, W., Cornford, C., Allen, P., 1997. New coalification profiles in the Molasse Basin of western Switzerland: Implications for the thermal and geodynamic evolution of the alpine foreland. Eclogae Geologicae Helvetiae 90 (1), 79–96.

Schlunegger, F., Burbank, D., Matter, A., Engesser, B., Mödden, C., 1996. Magnetostratigraphic calibration of the Oligocene to Middle Miocene (30-15Ma) mammal biozones and depositional sequences of the Swiss Molasse Basin. Eclogae Geologicae Helvetiae 89, 753–788.

Schmid, S., Boland, J., Paterson, M., 1977. Superplastic flow in fine grained limestone. Tectonophysics 43, 357–391.

Scholz, C., 1980. Shear heating and the state of stress on faults. Journal of Geophysical Research 85 (B11), 6174–6184.

Scholz, C., Cowie, P., 1990. Determination of total geologic strain from faulting. Nature 346, 837–839.

Schrader, F., 1988. Das regionale Gefüge der Drucklösungsdeformation an Geröllen im Westlichen Molassebecken. Geologische Rundschau 77 (2), 347–369.

Schreurs, G., 1994. Experiments on strike-slip faulting and block rotation. Geology 22 (6), 567–570.

Schultz-Ela, D., 1988. Application of a three-dimensional, finite element method of strain analyses. Journal of Structural Geology 10, 263–272.

Schüppli, H., 1950. Erdölgeologische Untersuchungen in der Schweiz, III Teil. In: Beiträge zur Geologie der Schweiz. Vol. 26(3) of Geotechnische Serie. p. 41.

Sheffels, B., 1995. Is the bend in the Bolivian Andes and orocline? In: Tankard, A., Suárez-Soruco, R., Welsink, H. (Eds.), Petroleum basins of South America. Vol. 62 of AAPG Memoir. pp. 511–522.

Sibson, R., 1980. Power dissipation and stress levels on faults in the upper crust. Journal of Geophysical Research 85 (B11), 6239–6247.

Siddans, A., 1979. Arcuate fold and thrust patterns in the Subalpine Chains of southeast France. Journal of Structural Geology 1 (2), 117–126.

Sommaruga, A., 1995. Tectonics of the Central Jura, and the Molasse Basin. New insights from the interpretation of seismic reflection data. Bulletin de la SociétŃeuchâteloise des Sciences Naturelles 118, 95–108.

Sommaruga, A., 1996. Geology of the central Jura and the Molasse Basin: new insight into an evaporite-based foreland fold and thrust belt. Ph.D. thesis, Université de Neuchâtel, unpublished.

Sommaruga, A., 1999. Décollement tectonics in the Jura foreland fold-and-thrust belt. Marine and Petroleum Geology 16, 111–134.

Spang, J., 1972. Numerical mehtod for dynamic analysis of calcite twin lamellae. Geological Society of America Bulletin 83, 467–472.

Spiers, C., 1979. Fabric development in polcrystals deformed at 400_{circ}c. Bulletin de Minéralogie 102, 282–289.

Spiers, C., 1982. The development of deformation textures in calcite rocks. Ph.D. thesis, University of London, unpublished.

Spiers, C., Rutter, E., 1984. A calcite twinning palaeopiezometer. In: Henderson, C. (Ed.), Progress in Experimental Petrology. Vol. D25 of NERC Publication Series. NERC, pp. 241–245.

Sylvester, A., 1988. Strike-slip faults. Geological Society of America, Bulletin 100, 1666–1703.

Tait, J., Bachtadse, V., Soffel, H., 1996. Eastern variscan fold belt: Paleomagnetic evidence for oroclinal bending. Geology 24 (10), 871–874.

Tourneret, C., Laurent, P., 1990. Paleostress orientations from calcite twins in the North Pyrenean foreland, determined by the Etchecopar inverse method. Tectonophysics 180, 287–302.

Tricart, P., 1984. From passive margin to continental collision: a tectonic scenario for the western Alps. American Journal of Science 284, 97–120.

Tschanz, X., 1990. Analyse de la déformation du Jura central entre Neuchâtel (Suisse) et Besancon (France). Eclogae Geologicae Helvetiae 88, 543–558.

Tschanz, X., Sommaruga, A., 1993. Deformation associated with folding above frontal and oblique ramps around the rhomb shaped Val-de-Ruz basin (Jura Mountains). Annales Tectonicae 7 (1), 53–70.

Tullis, T., 1980. The use of mechanical twinning in minerals as a measure of shear stress magnitudes. Journal of Geophysical Research 85 (B11), 6263–6268.

Turner, F., 1953. Nature and dynamic interpretation of deformation lamellae in calcite of three marbles. American Journal of Science 251, 276–298.

Turner, F., Griggs, D., Heard, H., 1954. Experimental deformation of calcite crystals. Geological Society of America Bulletin 65, 883–934.

Twiss, R., 1977. Theory and applicability of a recrystallized grain size piezometer. Pure and Applied Geophysics 115, 227–244.

Twiss, R., 1986. Variable sensitivity piezometric equations for dislocation denstiy and subgrain diameter and their relevance to olivine and quartz. In: Friedman, H., Heard, H. (Eds.), Mineral and Rock Deformation: Laboratory studies. Vol. 36 of Geophysical Monograph. American Geophysical Union, Washington D.C., pp. 247–262.

Wilkerson, M., Marshak, S., Bosworth, W., 1992. Computerized tomographic analysis of displacement trajectories and three-dimensional fold geometry above oblique thrust ramps. Geology 20, 439–442.

Wilkerson, M., Medwedeff, D., S.Marshak, 1991. Geometrical modeling of fault-related folds: a pseudo-three-dimensional approach. Journal of Structural Geology 13, 801–812.

Ziegler, P., 1982. Geological atlas of western and central Europe. Shell International Petroleum Maatshappij B.V.

Zoback, M., 1992. First- and second-order patterns of stress in the lithosphere: the world stress map project. Journal of Geophysical Research 97 (B8), 11703–11728.

Zoback, M., Tsukahara, H., Hickman, S., 1980. Stress measurements at depth in the vicinity of the San Andreas fault: Implications for the magnitude of shear stress at depth. Journal of Geophysical Research 85 (B11), 6157–6173.